GLOBAL MARINE CARBON EXPORT PRODUCTION DURING EOCENE HYPERTHERMAL EVENTS

ANGELA RUTH LEWIS

Presented to the Faculty of the Graduate School of

The University of Texas at Arlington in Partial Fulfillment

of the Requirements

for the Degree of

MASTER OF SCIENCE IN ENVIRONMENTAL AND EARTH SCIENCE

THE UNIVERSITY OF TEXAS AT ARLINGTON

December 2017

Acknowledgements

I would like to thank my advisor and mentor, Dr. Elizabeth Griffith, for believing in me and working with me over the last several years both as an undergraduate and as a graduate student. Dr. Griffith's guidance as a professor, researcher and a woman in the sciences has greatly expanded my understanding of the academic and scientific communities. I would also like to thank Dr. Arne Winguth for his continuous support throughout my graduate degree through continuous moral support and allowing me the privilege of being his graduate teaching assistant for some of his classes. This thesis was supported by the National Science Foundation Grant NSF-OCE 153660 and I am very grateful to the collaborators on the NSF grant, especially Dr. Ellen Thomas, whose vital contributions have made this project possible.

I am eternally grateful to my friends, family, and former coworkers who have been there for me through the good times and the bad, helping me formulate and realize my goals. Their support, wisdom and patience have helped me become who I am today.

November 17, 2017

Abstract

GLOBAL MARINE CARBON EXPORT PRODUCTION DURING EOCENE HYPERTHERMAL EVENTS

Angela R. Lewis, MS

The University of Texas at Arlington, 2017

Supervising Professor: Elizabeth M. Griffith

Early Eocene hyperthermal events can be an analog for global warming. Pelagic marine barite in deep sea sediment is a proxy for marine export production of organic matter into the deep ocean. Pelagic marine barite accumulation rates (BAR) were reconstructed over the Paleocene – Eocene Thermal Maximum (PETM; ~55.5 million years ago), Eocene Thermal Maximum 2 (ETM2; ~53.7 Ma) and ETM3 (~52.4 Ma) from ODP Sites 1209, 1215 and 1263. Northern Atlantic samples (with high detrital content) were acid digested and analyzed to reconstruct biogenic Ba (Ba/Al, Ba/Ti) and compare with elemental data from high resolution X-ray fluorescence. This data was used to test the following hypotheses: 1. Export production increases globally after the minimum carbon isotope excursion (CIE) defining the hyperthermal events due to increased surface production; 2. If driving mechanism(s) for ETM2 and ETM3 are similar to the PETM, then all three events should have similar trends in export production inferred from marine barite accumulation with lower magnitudes for ETM2 and ETM3; and 3. Enhanced remineralization in the thermocline will reduce the amount of exported organic matter that reaches the seafloor, potentially due to increased microbial metabolisms from temperature increases that consume organic material at faster rates resulting in less organic material sinking to the seafloor.

Despite reduced or unchanged surface productivity, export production (inferred from BAR) increased during the PETM, ETM2 and ETM3. Generally, maximum export production

occurred during the CIE minimums from increased organic carbon export efficiency from increased surface temperatures and/or increased aggregation from microbial transparent exopolymer particles. Export production was proportional to the CIE magnitude: highest after onset of the PETM and smallest after the onset of ETM3. Remineralization rates can be inferred from the difference between benthic foraminiferal data and export production. Low benthic foraminiferal accumulation (or high oligotrophic taxa) appear to be caused by low oxygen and nutrients in the deep ocean due to high remineralization rates from warm intermediate depths and less ballasting. Low oxygen levels in intermediate water depths suggest high oxygen utilization rates from remineralization supporting this interpretation.

Table of Contents

List of Illustrations

List of Tables

Chapter 1

Introduction: Purpose of Research

Hyperthermals are periods of extremely elevated temperatures with a very low equator-to-pole sea surface temperature gradient, reduced Ekman-induced upwelling and less vigorous deep ocean circulation, limiting upwelling (Lourens et al., 2005; Thomas et al., 2000). Understanding how hyperthermal events changed the Earth in the past will help us to better predict the potential changes that global warming can cause in the near future (Zachos et al., 2008). In the lower Eocene, there were three significant hyperthermal events: Paleocene – Eocene Thermal Maximum (PETM), Eocene Thermal Maximum 2 (ETM2) and ETM3 (also known as the Elmo and K/X event respectively; Lourens et al., 2005; Nicolo et al., 2007).

The PETM is the event with the largest negative carbon isotope excursion (CIE) with a magnitude that ranged between -2.5‰ to -5 ‰ in bulk carbonate and total organic carbon, which resulted in global warming of 5°C to 8°C (Dunkley-Jones et al., 2013; Sluijs and Dickens, 2012). The PETM occurred about 55.53 million years ago (Ma) with a duration of approximately 170 thousand years (Röhl et al., 2007; Westerhold et al., 2012). During the PETM there was ocean acidification, which resulted in Calcite Compensation Depth (CCD) shoaling and diminished carbonate preservation (McInerney and Wing, 2011; Zachos et al., 2005). There are numerous proposed carbon sources that caused the CIE at the PETM that include release of methane gas hydrates, volcanic CO_2, methane from melting of Antarctic permafrost and carbon by submarine magmatic activity (e.g., DeConto et al., 2012; Dickens, 2011; Eldholm and Thomas, 1993; Svensen et al., 2004). There are also several potential mechanisms for the removal and sequestration of the excess carbon after the PETM such as enhanced silicate weathering, organic carbon burial, and changes in marine export production and remineralization (e.g., Bowen and Zachos, 2010; Ma et al., 2014; Zachos et al., 2005).

ETM2 and ETM3 occurred 2 Ma after the PETM (approximately 1.5 Ma apart), with ~40 thousand years (ky) duration (Röhl et al., 2007; Stap et al., 2009; 2010). The benthic foraminiferal CIE of ETM2 was about -1.4‰ and generating 3°C of global warming while ETM3 had a -0.8‰ benthic foraminiferal CIE with 2°C warming (Stap et al., 2010). Proposed mechanisms for these hyperthermal events are similar to some of those proposed for the PETM, which are either the release of carbon from sedimentary reservoirs such as melted permafrost on Antarctica, peat bogs or decay or increased dissolved organic carbon or DOC (e.g., Littler et al., 2014; Sexton et al., 2011). Recovery from the marine carbonate dissolution of the smaller Eocene hyperthermals could potentially be from enhanced weathering of terrestrial carbonates, elevating $CaCO_3$ saturation in the ocean and carbon sequestration (Stap et al., 2009). Weathering of silicate minerals also draws down atmospheric CO_2 over long 100 kyr intervals, however ETM2 recovers over only 30 kyr (Ridgewell and Zeebe, 2005; Stap et al. 2009).

1.1 Global warming

Recent global warming due to anthropogenic induced carbon emissions in to the atmosphere is similar to early Eocene hyperthermals because both warming events include large quantities of carbon introduced into the environment in a geologically short period of time. Exploring the effect that changes in ocean biogeochemical cycles during Eocene hyperthermal events had on the ocean in the past can lead to understanding potential impacts of carbon uptake into the ocean. Prior to the Industrial Revolution (1750 A.D.) the atmosphere contained approximately 280 ppm CO_2 (Keeling et al., 2005) and as of July 2016, the National Oceanic and Atmospheric Association's (NOAA) Global Monitoring Division reported that the global monthly atmospheric CO_2 levels are approximately 402 ppm (NOAA, 2016). Observed monthly atmospheric $\delta^{13}C$ values at Mauna Loa, Hawaii were approximately -8.2‰ PDB in 2008 and cumulative anthropogenic CO_2 emissions were approximately 2,000 gigatonnes (Gt) from 1750 to 2011 (IPCC,

2014; Keeling et al., 2010). Anthropogenic CO_2 emissions since the Industrial Revolution are rapidly approaching the 2,300 and 6,300 Gt of carbon (depending on the carbon source; e.g., CO_2, methane) thought to have triggered the PETM CIE (Dickens et al., 1995; Pagani et al., 2006; Panchuk et al., 2008; Zeebe et al., 2009).

The latest Intergovernmental Panel on Climate Change (IPCC, 2014) reported observed warming over 0.5°C from 1951 to 2010 and globally averaged land and sea surface temperature (SST) anomalies of approximately 0.75°C from 1880 to 2005. An increase of at least 0.5°C over the last 125 years is a shorter timeframe than the geologically rapid onset of approximately 20 kyr for the early Eocene hyperthermals (Stap et al., 2010; Zachos et al., 2005). Globally averaged SSTs are projected to be between 1.5°C and 4°C by 2100 (IPCC, 2014). Global temperature projections for the future are almost as high as the PETM (+5 to 8°C) and even conservative projections approach the +2°C of ETM3 (Dunkley-Jones et al., 2013; Sluijs and Dickens, 2012; Stap et al., 2010).

This increase in global surface temperatures has resulted in substantial the reduction of glacial mass as well as thermal expansion of the ocean. Together glacial melt and thermal expansion have raised the average global sea level by 0.05 m since the early 1900s (IPCC, 2014; Vermeer and Rahmstorf, 2009). Warmer surface temperatures also lead to enhanced stratification of the ocean by increasing the temperature gradient (thermocline) between the surface layer and the rest of the ocean. This stratification prevents mixing between water layers reducing oxygen diffusion and the transport of nutrients.

Increase in the atmosphere to the ocean pCO_2 gradient also increase CO_2 flux into the ocean, increasing oceanic dissolved CO_2 concentration levels leading to lowered pH and ocean acidification (Doney et al., 2009). Global seawater pH is at least 0.1 units lower than the preindustrial ocean pH ranges and future projections estimate a reduction of up 0.3 or 0.4 pH units (Orr et al., 2005). Calcareous marine organisms precipitate calcium carbonate ($CaCO_3$) from the seawater during shell formation, but $CaCO_3$ is more soluble in acidic conditions which can reduce

the rate of precipitation or even leach $CaCO_3$ out of shells (e.g., Hendriks et al., 2010). Evidence of ocean acidification during the hyperthermals can be seen through carbonate dissolution of marine sediment and boron isotope ratios ($\delta^{11}B$) which are thought to reflect changes in the pH of seawater (e.g., Gutjahr et al., 2017; Kelly et al., 2010; Zachos et al., 2005). However, some calcareous primary producers have demonstrated elevated metabolisms from the abundance of dissolved CO_2 and pH in seawater has not been low enough to damage their shells (Holcomb et al., 2014; Iglesias-Rodriguez et al., 2008). The continual exponential rise in atmospheric pCO_2 indicates that it is likely only a matter of time before ocean acidification becomes a serious problem for all marine organisms (Hoegh-Guldberg et al., 2007).

1.2 Global carbon cycle

Carbon is one of the critical elements required for life and it is recycled throughout the natural environment (Figure 1.1). Carbon reservoir residence timescales, depicted in Figure 1.2 and range from 0.1 to 100 million years. The ocean is the largest reservoir of C in the short-term carbon cycle (Figure 1.1B) and air-sea gas exchange draws CO_2 into the surface layers (euphotic zone) where photosynthesis, respiration and decomposition occur. Over long time scales carbon can be released to the atmosphere from volcanic activity, hydrothermal vents, photosynthetic respiration from plants and phytoplankton in marine and aquatic environments, biomass burning, permafrost and marine sediments (gas hydrates). Carbon can be sequestered through decomposition and burial of organic carbon occurs in sediments. Acid hydrolysis dissolves limestone and consumes CO_2 from the atmosphere and releases calcium and carbonate ions (CO_3^{-2}) that can be transported by river runoff to the ocean. Carbonate minerals precipitate in the oceans and can accumulate in marine sediments to either ultimately be subducted into the mantle or released due to diagenesis (Berner, 2003).

Carbon is also exchange between the atmosphere and the biosphere (Figure 1.1B). In terrestrial environments, CO_2 assimilated used by plants and a due to anthropogenic induced carbon emissions in to the atmosphere. The ocean is the largest reservoir of C in the short-term carbon cycle (Figure 1.1B) and air-sea gas exchange draws CO_2 into the surface layers (euphotic zone) where photosynthesis, respiration and decomposition occur.

1.3 Marine environment

1.3.1 Marine carbon transport

Marine organisms in the ocean surface transform carbon (e.g., CO_2, dust, riverine sources) into organic matter which is transported through the water column by other organisms, sinking, ocean circulation and subsequent burial in deep sea sediments. There are two major carbon pumps in the ocean: the solubility pump and the biological pump which can be separated by the more prominent soft tissue pump and the $CaCO_3$ counterpump (Volk and Hoffert, 1985). The soft-tissue pump (Figure 1.3) describes the mechanism for uptake of dissolved inorganic carbon (DIC) through photosynthesis by primary producers in the euphotic zone (Figure 1.4), which can be limited by the availability of nutrients and sunlight (Berger et al., 1989; Falkowski et al., 1998). Detrital organic matter is exported from the euphotic zone as particulate organic carbon (POC) and the more easily accessible or labile material is readily remineralized through heterotrophic respiration primarily in the thermocline, whereas a small portion (~1%) is deposited at the sea floor. Apparent oxygen utilization (AOU) in the ocean can be used as an indicator of aerobic remineralization due to the consumption of dissolved oxygen (DO) by heterotrophic organisms during the breakdown of labile POC (Pytkowicx, 1975). Changes in AOU over time can be expressed as true oxygenation utilization or oxygen utilization rate (OUR) which is highest in the thermocline (Broecker and Peng, 1982; Sarmiento et al., 1990).

The remaining, more refractory material (~1% of the total particulate organic carbon (POC) flux) descends through the seawater column until it is incorporated into the marine sediment (Broecker and Peng, 1982; Rivkin and Legendre, 2001). The POC flux is ballasted by mineral components (Amstrong et al., 2002; Klaas and Archer, 2002) and characterized by substantial regional variations (Buesseler, 1991). Dissolved inorganic carbon (DIC) accumulates in the deep ocean and can be upwelled back to the surface through ocean circulation patterns, where it can be consumed by primary producers in the euphotic zone (Daneri et al., 2000).

1.3.2 Ocean circulation

The transport (advection and eddy-induced mixing) of water masses in the ocean has a significant impact on the distribution of nutrients in the water column that support marine productivity (Ganachaud and Wunsch, 2000). The ocean surface circulation is driven by heat, freshwater, and momentum between the atmosphere and the ocean (Bryan and Cox, 1967; Defant, 1961; Ekman, 1905; Maier-Reimer et al., 1993; Stommel, 1979). Upwelling of cold, nutrient rich deep water occurs on the eastern side of ocean basins, and in the Equatorial region around the intertropical convergence zone or ITCZ (Reid, 1948; Stommel, 1948).

Intense warming during the early Eocene could have reduced deep water mass formation in the ocean due to lower meridional temperature gradients and freshening of seawater at the poles from enhanced precipitation (e.g., Bice et al., 1997; Brinkhuis et al., 2006). Reduced deep ocean circulation and possible reduced trade winds and a switch form the thermal mode to a haline mode (Jin et al., 1999) during the PETM could have limited surface marine primary productivity through reduced upwelling of nutrients (Winguth et al., 2012). Pelagic surface primary productivity of POC also depends on the availability of adequate sunlight, temperature, macro- and micro-nutrients (e.g., N, P, Si, Fe, Zn) and mixing but ocean acidification during the PETM would limit productivity of calcareous organisms is due to calcite dissolution (Zachos et al., 2005).

1.3.3 Marginal marine boundaries

In general, marine carbon transport processes along continental margins are similar to processes in the open ocean. However, fluvial sediment influx along the continental margin increases the amounts of nutrients, clay and suspended particles (turbidity) in the seawater column. Turbid water lowers the light penetration depth, which can reduce the availability of sunlight for photosynthesis (Cloern, 1987). Overall, the continental margin exports carbon more efficiently than the open ocean even though the open ocean produces larger quantities of carbon over a larger area (Sarmiento and Gruber, 2006). In Figure 1.5 Sarmiento and Gruber (2006) demonstrated that approximately 48% of surface POC the along continental margins were exported while 18% of pelagic POC was exported to the deep ocean.

The Eocene hyperthermals are thought to have had increased precipitation along the equator and in the high latitudes, resulting in larger fluvial freshwater runoff and sediment deposition (e.g., Pagani et al., 2006; Bornemann et al., 2014). Therefore, local hydrologic changes at sites in the marginal marine environment could have had a significant impact on primary production and export production that would not be present at more distal sites.

1.4 Relevant paleoenvironmental proxies

Isotopes are atoms of an element with different numbers of neutrons which results in differing atomic masses. Heavier isotopes form stable low energy bonds while lighter isotopes are less stable and are more involved in chemical reactions (Bigeleisen, 1965). Stable isotope fractionation occurs as a result of differences in bond stability, resulting in the preferential incorporation of lighter isotopes in organic material for example. The relationship between the abundance of heavy to light isotopes relative to a standard is expressed using δ notation (McKinney et al., 1950). The isotopic ratio for C is calculated in per mil (‰) with Vienna Pee Dee Belemnite (VPDB) standard:

$$\delta^{13}C = \left(\frac{\left(\frac{^{13}C}{^{12}C}\right)_{sample} - \left(\frac{^{13}C}{^{12}C}\right)_{standard}}{\left(\frac{^{13}C}{^{12}C}\right)_{standard}} \right) X\ 1000\ ‰$$

Isotopic data (like $\delta^{13}C$) and selected chemical compounds are used as proxies for the reconstruction of paleoenvironments (Urey, 1948). For example, low $\delta^{13}C$ values recorded in benthic foraminiferal tests are indicative of large amounts of light carbon input into the marine environment, either in the form of CO_2 or methane (Zachos et al., 2008).

Multiple potential sources of light carbon have been proposed for the PETM. Methane $\delta^{13}C$ values are ~-60‰ (Kvenvolden, 1993) which could be released through destabilization of methane clathrates due to continental slope failure (Katz et al., 1999) and/or increased temperatures (Dickens et al., 1995; 1997). Another methane source is thermogenic methane ($\delta^{13}C$ ~ -30‰) released from organic-rich sediments injected with magma in the North Atlantic (Svensen et al., 2004; 2010; Westerhold et al., 2009). Other potential sources of carbon for the PETM are large scale wildfires from burning peat and coal ($\delta^{13}C$ ~ -22‰), rapid drying and oxidation of organic matter in isolated epicontinental seas in Asia ($\delta^{13}C$ ~ -22‰; Gavrilov et al., 2003; Higgins and Schrag 2006), and melting of Antarctic permafrost and peat ($\delta^{13}C$ ~ -30‰; DeConto et al., 2010).

Isotopic fractionation of oxygen in carbonate minerals and water is temperature dependent and the difference in $\delta^{18}O$ between water and precipitated calcite is used to reconstruct water temperatures (Urey, 1947). Living organisms use $CaCO_3$ from the seawater to form their shells and some organisms preserve the isotopic values of the water while others alter the isotopic values through metabolic fractionation through vital or kinetic effects (McCrea, 1950; Urey et al., 1951). The ratio of stable heavy to light oxygen (O) is $^{18}O/^{16}O$, which is fractionated in the hydrologic cycle by the preferential evaporation of ^{16}O and the precipitation of ^{18}O in water vapor and water, respectively. High $\delta^{18}O$ values of benthic foraminifera tests reflect cooler global temperatures because a higher amount of ^{16}O is sequestered in continental ice sheets, leaving the ocean concentrated in the heavier ^{18}O during times of cooler global temperatures (Gat, 1996).

Paleotemperatures for the Cenozoic were reconstructed with $\delta^{18}O$ values from benthic foraminiferal tests and indicate large temperature fluctuations from high temperatures during the PETM and early Eocene to glaciation events such as the expansion of the Antarctic ice-sheets and Northern hemispheric glaciation (Zachos et al., 2001).

Proxy data can be derived from the geochemical analysis of materials preserved in marine sediment, such as aeolian dust, clays, organic and inorganic material, such as the carbonate foraminiferal tests that are widely utilized in geochemical analysis. Foraminifera are single-celled, heterotrophic protists that precipitate calcium carbonate from seawater forming shells that form in a characteristic manner that is dependent on the sea (Rosenthal et al., 1997). Foraminifera occur in all water depth ranging from planktonic (euphotic) or benthic (seafloor) and their accumulation rate in marine sediment reflects marine productivity in those regions as long as the underlying sediment is above the CCD (Thomas, 2007).

Pelagic marine barite ($BaSO_4$) accumulation in marine sediments is used as a proxy for marine export production, organic matter that is not recycled in the euphotic zone but is exported out of this zone into the deep ocean (Paytan and Griffith, 2007). Barium is released from organic matter during its decomposition, saturating a small space (microenvironment) within the decaying organic matter and allowing for the precipitation of marine barite (Paytan and Griffith, 2007). Barite precipitation is otherwise limited when seawater is undersaturated with respect to barite, which is the case in most areas of the ocean (Monnin and Cividini, 2006). The ratio of Sr/Ba has been used as a proxy for barite saturation of seawater (Van Beek et al., 2003). Pelagic marine barite (Figure 1.6) is typically morphologically distinguished from other forms of barite (i.e., hydrothermal barite), being euhedral to sub-spherical grains that are usually less than 5 μm (Dehairs et al., 1980; Bishop, 1988; Bertram and Cowen, 1997).

1.5 Review of productivity changes during hyperthermal events

Barite accumulation rates (BAR) have been reconstructed from numerous areas during the PETM by Ma et al. (2014) and interpreted to be generally increasing in most areas of the ocean (Figure 1.7). Paytan et al. (2007) previously found no change in the barite saturation levels during the PETM. This suggests that the increase in BAR is due to increased marine export production in the overlaying water column. Export productivity was used as a reflection of the strength of the biological pump in sequestering carbon by enhanced transport and regeneration of organic material from the euphotic zone. Ma et al. (2014) reported generally global increased marine export production with the largest elevations in the Equatorial region, especially in the Pacific and along South America. There were also significant elevations in export production along the continental margins in the Northern Hemisphere.

Throughout the PETM there is evidence of deoxygenation in the thermocline, potentially the result of enhanced remineralization due to increased microbial metabolism from the warm hyperthermal environments (Ma et al., 2014). Ocean acidification causes calcium carbonate dissolution, reducing ballast material to form aggregates so organic material does not readily sink and instead spends a longer time in the thermocline. Elevated microbial activity and decreased sinking rates of organic matter could lead to the remineralization of larger quantities of organic material and less exported to the benthics (de Jesus Mendes and Thomsen, 2012; Gibbs et al., 2010). Enhanced remineralization would recycle larger quantities of organic matter in the thermocline, reducing the amount of organic matter available to sustain benthic foraminifera (Ma et al., 2014). A reduction in organic matter would subsequently reduce the benthic foraminiferal population.

Benthic faunal turnover occurred in the western Pacific during the PETM resulting in smaller test size (“dwarfism”) and an abundance of opportunistic species, likely due to lower dissolved oxygen levels and reduced surface productivity after the onset of the PETM CIE (Takeda and Kaiho, 2007). In contrast, planktonic foraminiferal tests increased in size and there was a shift

to predominately oligotrophic taxa attributed to thermal stratification and reduced nutrient levels (Kaiho et al., 2006; Petrizzo, 2007). The PETM also led to extinctions and reduced diversity of benthic foraminiferal populations in the eastern Equatorial Pacific (Nomura et al., 2005).

Analysis of benthic foraminiferal species in the Southeastern Atlantic suggest increased calcification and extinction during the PETM, but only smaller scale biodiversity shifts during ETM2 (Foster et al., 2013). Changes in ocean circulation created warmer seawater that elevated benthic foraminiferal metabolisms during ETM2 evidenced by low benthic foraminifera accumulation rates (BFAR) despite the presence of low oxygen tolerant taxa (Jennions et al., 2015).

Along the continental margin in the Northeastern Atlantic there was potentially weakened deep water currents during ETM2 and ETM3, interpreted from initially small grain sizes at the onset of the hyperthermal, but gradually increasing sizes during the recovery of the CIEs (D'haenens et al., 2014). A decline in benthic foraminiferal populations is thought to be the result of reduced seasonal blooms of primary production, evidenced by a reduction in opportunistic species that usually are present in nutrient poor environments (D'haenens et al., 2012). Planktonic foraminiferal population shifts at this same site were likely the result of warming, ocean stratification and reduced oxygen over all three hyperthermal (Pardo et al., 1997). Bornemann et al. (2014) found evidence that there were changes in the hydrologic regime of along the continental marine in the Northern Atlantic, namely increased freshwater input and weathered terrigenous material that could have prolonged the environmental impact of the PETM, obscuring the distinction between the PETM and ETM2.

1.6 Hypotheses

Barite accumulation rates (BAR) were reconstructed from International Ocean Discovery Program (IODP) sites in the western Pacific, Equatorial Pacific, northern Atlantic and southern Atlantic over the PETM, ETM2 and ETM3. BAR was used to determine changes in export

production in the regions following previous work by Paytan et al. (1996) and Ma et al. (2014). Export production at the study sites were compared to benthic foraminiferal accumulation rates (BFAR) to infer potential changes to remineralization and to answer the following questions.

1. What is the relationship between export production and the CIE minimums at the Eocene hyperthermal events?

I hypothesize that export production increases globally after the minimum CIE peak due to an increase in surface production caused by the warming events. Generally, export production increased globally following the PETM CIE minimum (Figure 1.7; Ma et al., 2014). If the increased export production was caused by increased surface production due to the warming event, then ETM2 and 3 should also have increased export production following the peak of their CIE events as these are also warming events. All the sites should have elevations during the CIE events, similar to the nearly global increases in export production during the PETM (Ma et al., 2014), although variations in the amount of export production is expected between sites. The amount of export production should vary with each site location depending on many factors including the rate of primary production, efficiency of remineralization, and nutrient availability from ocean circulation.

2. Is there a difference in export production between the PETM and ETM2 and 3?

There is an ongoing debate about the driving mechanism(s) of the PETM, ETM2 and ETM3 and what role orbital cyclicity had in the three Eocene hyperthermal events (Littler et al., 2014; Lourens et al., 2005; Westerhold et al., 2011; Zachos et al., 2010). However, I hypothesize that if the driving mechanism(s) for ETM2 and ETM3 are the same as the PETM, then all three events should have the same trends with lower magnitudes for the smaller CIEs (ETM2 and ETM3).

3. Is there a relationship between export production and benthic foraminifera?

I hypothesize that enhanced remineralization in the thermocline, potentially due to increased microbial metabolisms will consume exported organic material at faster rates resulting in less organic material sinking to the benthics. This could result in the reduction of organic material

available to sustain the benthic foraminiferal populations at depth. There is already evidence that hyperthermal events adversely impacted benthic foraminiferal populations such as the benthic extinction event during the PETM and the reduction of benthic foraminifera during ETM2 in the Southeast Atlantic at Sites 1262 and 1263 (Jennions et al., 2015; Thomas, 2007).

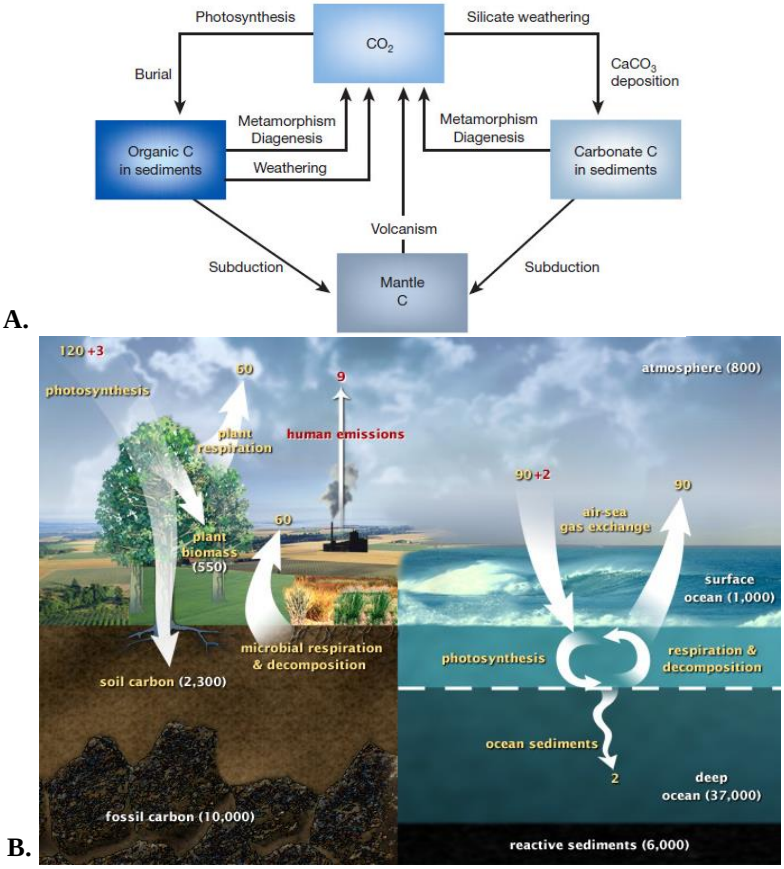

Figure 1.1: Long- and short-term carbon cycles. A. Long-term carbon cycle transport (arrows) through the atmosphere, biosphere and geosphere (reservoir boxes; Berner, 2003). B. Cartoon of the short-term carbon cycle in terrestrial and marine environments. Arrows represent the movement carbon between the labeled reservoirs in Pg of C yr^{-1}, yellow indicates natural fluxes, red are anthropogenic fluxes and white is carbon sequestration (Riebeek, 2011; modified from U.S. DOE, Biological and Environmental Research Information System).

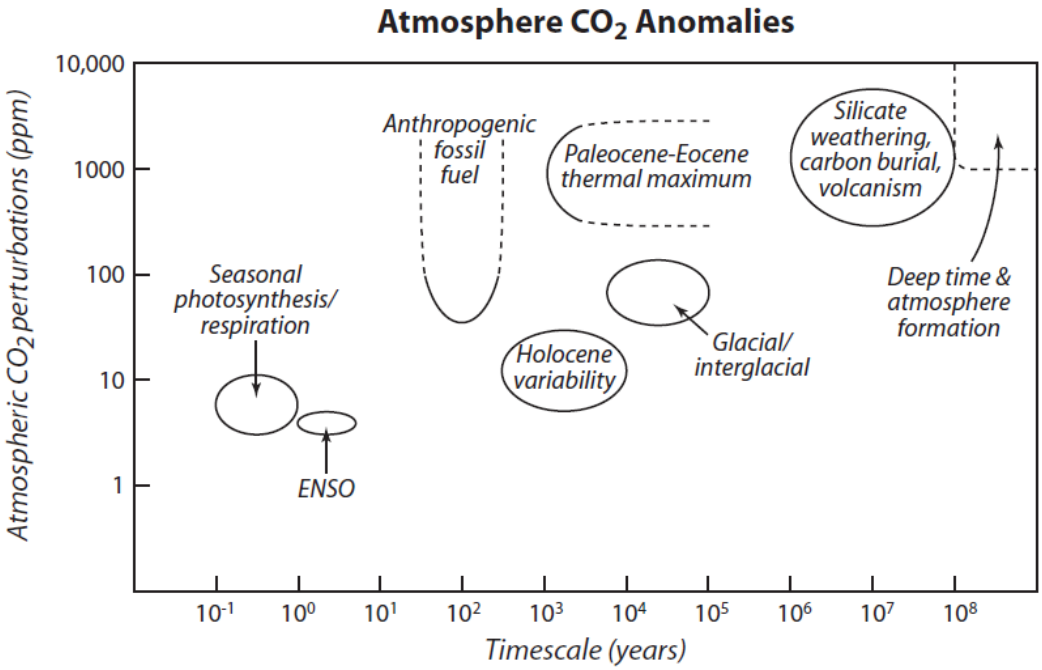

Figure 1.2: Timescale comparison for atmospheric CO_2 (Doney and Schimel, 2007)

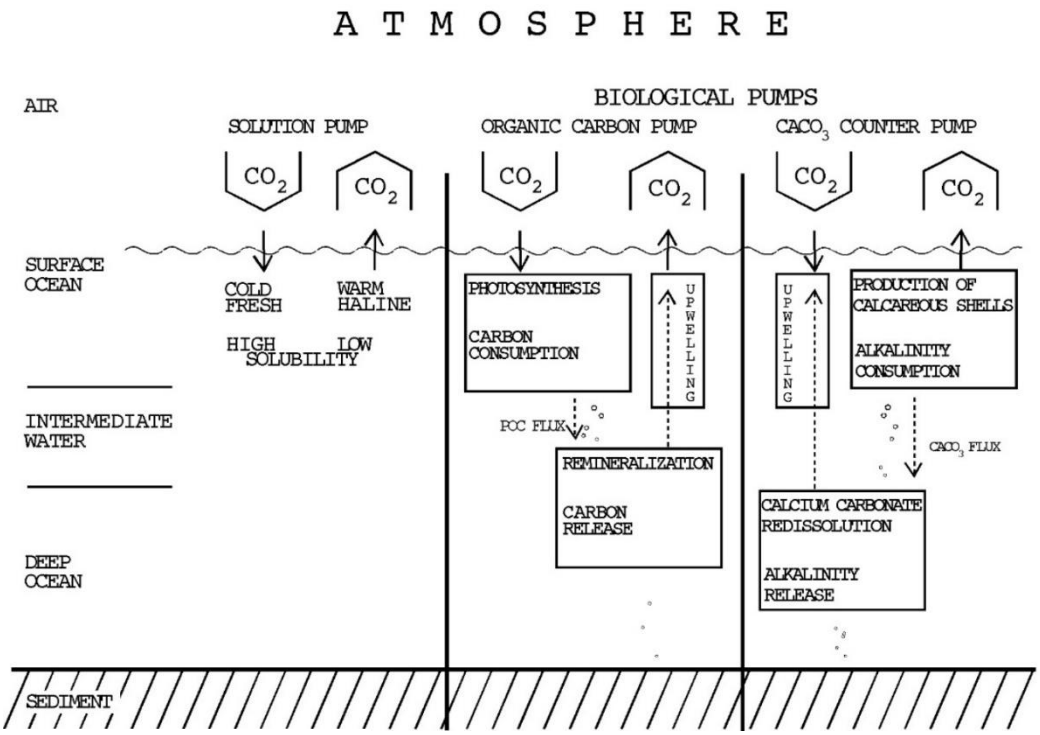

Figure 1.3: Marine carbon pumps represent the vertical transport mechanisms of dissolved inorganic carbon (DIC) through the seawater column. This transport is driven by the solubility of CO_2 due to surface thermohaline conditions, the biological incorporation of carbon in organic soft-tissue and the precipitation of inorganic calcium carbonate ($CaCO_3$) shells (Heinze et al., 1991). Recently, the solubility pump has been expanded into the air-sea gas exchange pump which also includes DIC and alkalinity (Sarmiento and Gruber, 2006).

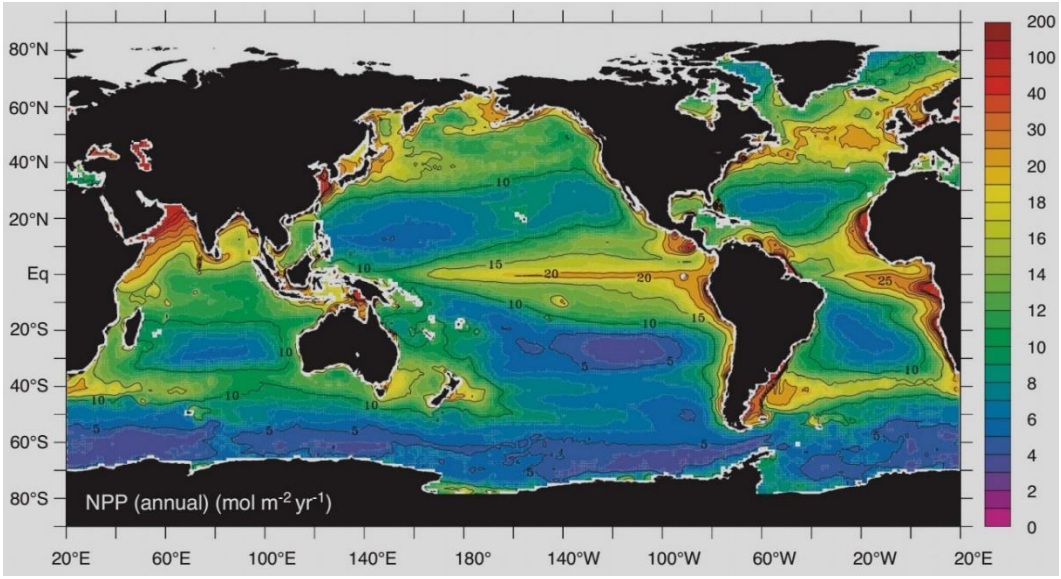

Figure 1.4: Modern marine annual net primary productivity or NPP in mol m^{-2} yr^{-1} (Sarmiento and Gruber, 2006).

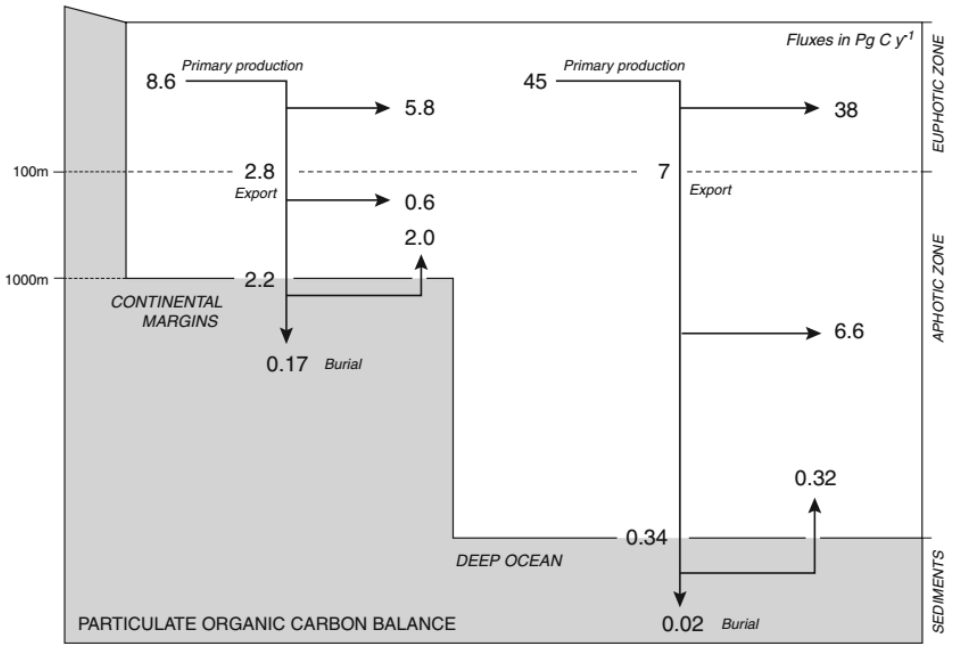

Figure 1.5: Carbon flux differences (in Pg C y^{-1}) between the continental margin and the deep ocean. Overall, the continental margin exports carbon more efficiently than the open ocean even though the open ocean produces larger quantities of carbon over a larger area (Sarmiento and Gruber, 2006).

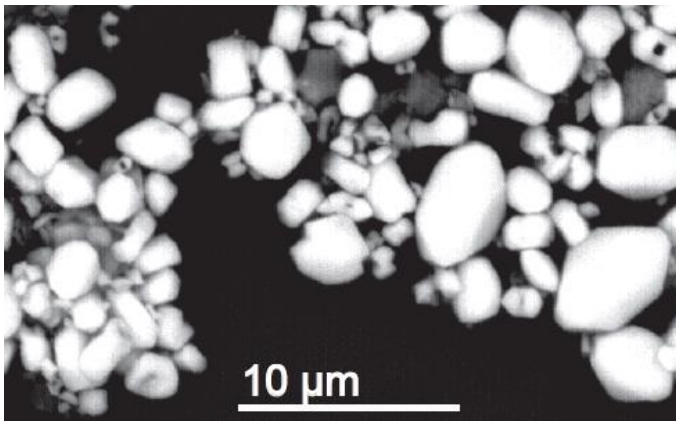

Figure 1.6: Scanning electron microscope (SEM) image of marine pelagic barite. Backscattered (BSE) image was captured using a Hitachi S-3000N SEM. Marine pelagic barite (white grains) and refractory material (gray grains) such as rutile, anatase and residual silicate minerals obtained from sample Site 1263C 10 H 6 58-60 cm from approximately 80 kyr after the onset of ETM2.

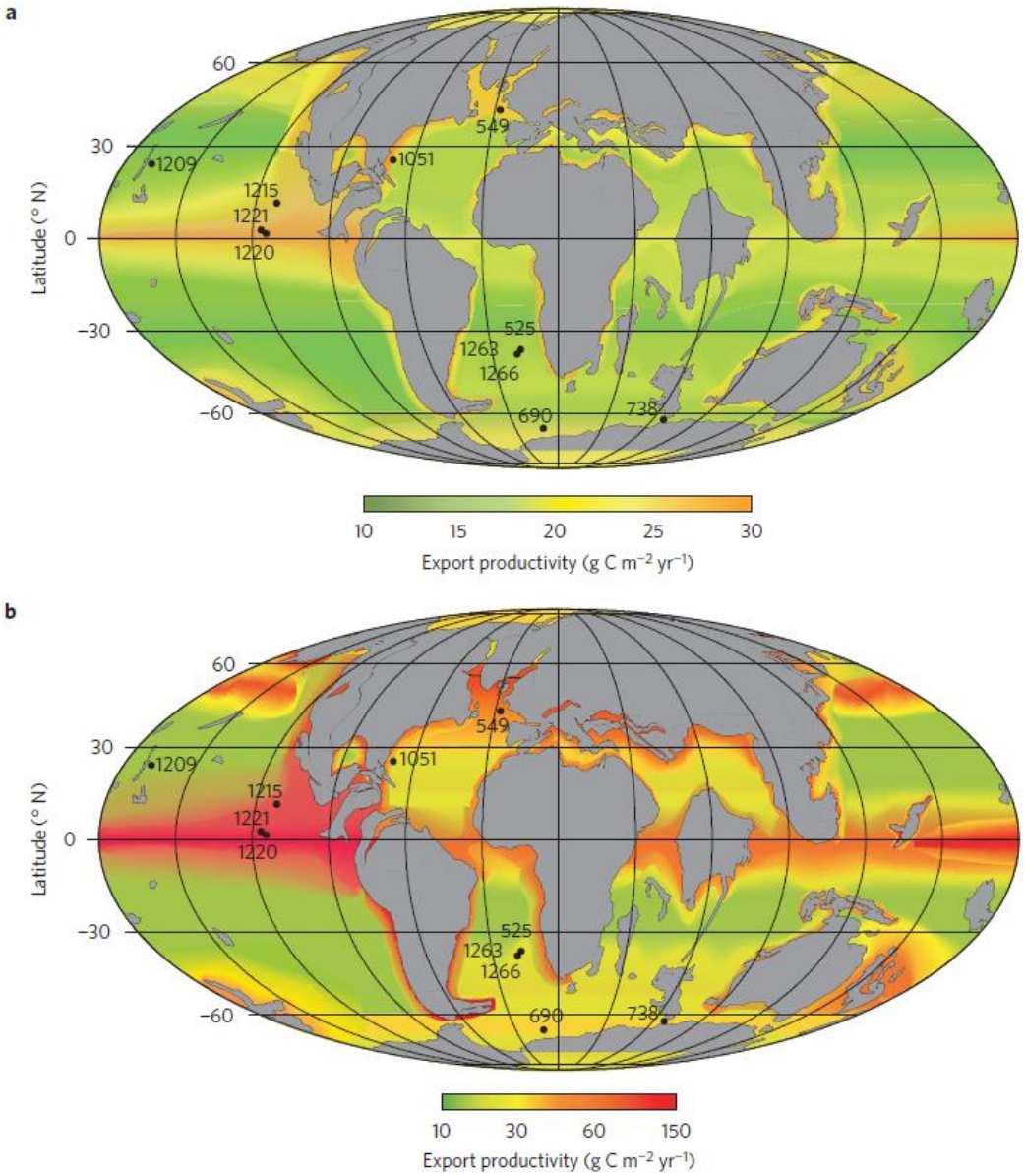

Figure 1.7: Export productivity before and during the PETM. Export productivity calculated from BAR a. prior to the PETM and b. during the PETM from Ma et al. (2014). The is a general global increase in export production during the PETM, with the largest increase in the Equatorial regions, the Southern Ocean and in the Northern Atlantic Ocean (Ma et al., 2014).

Chapter 2

Methods

2.1 Study Sites

The study site locations are listed in Table 2.1. The Ocean Drilling Program (ODP) Expedition 198 Site 1209 is located in the Western Pacific Ocean (32°30.1081′N, 158°30.3564′E) southeast of Japan on the central portion of the Southern High of Shatsky Rise (Figure 2.1). The modern water depth is 2.387 km and a paleodepth of approximately 2.4 km (Bralower et al., 2002). The ODP Expedition 199 Site 1215 is located at in the equatorial Pacific Ocean northeast of Honolulu (26°01.77´N, 147°55.99´W) at a modern water depth of 5.396 km and paleodepth approximately 3.3 km (Shipboard Scientific Party, 2002a). The CCD paleodepth at Site 1215 was about 3.03 km during the PETM, 3.20 km during ETM2 and 3.25 km during ETM3, potentially placing the site was very close to the CCD during the PETM and ETM3 (Leon-Rodriguez and Dickens, 2010). The ODP Expedition 208 Site 1263 is located in the Southeast Atlantic Ocean along the Walvis Ridge (28°31.98′S, 02°46.77′E) at a modern depth of 2.717 km and paleodepth of about 1.5 km (Zachos, et al., 2004). The Deep Sea Drilling Project (DSDP) Expedition 48 Site 401 is located in the Northeast Atlantic Ocean on the north Biscay margin off the west coast of France (47°25.65'N, 08°48.62'W) and a paleolocation of ~43°N (McInerney and Wing, 2011). Site 401 is at a modern water depth of 2.495 km (Montadert et al., 1979) and a paleodepth of 1.8 to 2.0 km during the early Eocene (D'haenens et al., 2014).

2.2 Barite and heavy liquid separations

Marine barite was extracted from approximately 200 marine sediment core samples in the wet chemistry lab (PI Griffith) following a procedure outlined by Paytan et al. (1996) and summarized in Table 2.2. The procedure historically yields a retention of approximately 95% of the original barite in a sample with less than 5% lost during the rinsing steps (Eagle et al., 2003). The

initial bulk sediment was portioned into 20 to 40 g per sample that were dried in an oven to remove any moisture from the samples and weighed after cooling in a dessicator. Samples were then processed through a series of acid and bleach dissolution steps to remove any carbonates, organics, Fe-Mn oxyhydroxides and silicates that may have been present (Table 2.2). A final dissolution step was performed with saturated aluminum chloride to remove any potential fluoride byproducts.

Samples were rinsed and vacuum filtered through a preweighed 0.4 μm EMD Millipore Isopore Polycarbonate Membrane Filters filter and stored in labeled, preweighed petri dishes. Samples were dried for two days in an oven and dessicated for one hour prior to weighing. Sample purity was accessed, prior to sample ashing, in the UTA Characterization Center for Materials and Biology with a Hitachi S-3000N scanning electron microscope (SEM) and Energy-dispersive X-ray spectroscopy (EDS) with EDAX and Thermo NSS Spectral Analysis software. For each sample, 5 backscatter images were obtained, contrast corrected with GIMP 2 (GNU image manipulation program) and modified by test_red_fill_script2.m (Appendix C.1) with MATLAB Software version R2016a, to color most of the impurities red. Each SEM image was inspected and corrected as needed then analyzed with MATLAB by SEMImageAnalysis.m and PercentBaSO4new.m concurrently (Appendix C.2 and C.3). Percentage of barite grains in the residual samples were accessed by calculating the average area of the barite grains divided by the total area of grains.

Samples from Site 1215 that contained chert fragments and grains were separated from the residual barite by sodium polytungstate (SPT) heavy liquid separation. After the barite separation procedure (Table 2.2), the individual samples were combined with 20 mL of 2.95 g/cm^3 SPT solution, sonicated for 5 minutes and centrifuged for 5 minutes at the settings “9” acceleration/“5” deceleration and 3000 rotations per minute. Then the samples gravity settled for 20 minutes and separated by freezing the settled, dense residue with liquid nitrogen, followed by rinsing of the heavy fraction (with barite) in the SPT using vacuum filtration and a preweighed 0.4 μm filter. Samples were then stored in labeled, preweighed petri dishes, oven dried for two days and dessicated for one

hour prior to weighing. Sample residues collected were then analyzed with SEM imaging and MATLAB codes for purity verification.

2.3 Bulk digestion

Bulk digestion was performed on the barite separation residues of about 31 samples from Site 401, due to an abundance of clays in the samples that could not be separated by heavy liquid separation with SPT or lithium heteropolytungstates (LST), which was heated and sonicated in a warm water bath to 35°C to achieve 3.05 g/ml. Sample residues were processed using sealed vial acid hotplate digestion (Table 2.3) following the procedure outlined in Scudder et al. (2014). Samples were placed in acid cleaned Teflon vials with concentrated trace metal grade hydrofluoric acid and once distilled trace metal grade nitric and hydrochloric acids then heated at 98°C on a hotplate. Hydrogen peroxide (2 mL) was added on the second day and the samples were resealed and placed back on the 98°C hotplate for a total of 5 days. All 9 of the bulk sediment samples from Site 401 were fully digested by hotplate method.

However, the majority of Site 401 barite separation residues were not completely digested after 5 days (or even 2 weeks) so they were digested by the sealed vial acid microwave digestion procedure (Table 2.4), modified from Murray and Leinen (1996). Microwave digestion with concentrated nitric and hydrofluoric acid was performed in buttress threaded Savillex digestion vials with 3 layers of polytetrafluoroethylene (PTFE) thread seal tape (plumber's tape) around the threading, and the lids tightened as much as possible with Savillex wrenches. Samples were placed in a thick Tupperware container, plastic wrap placed taught over the opening and the Tupperware lid sealed. The samples were microwaved for a total of 2 hours then a series of acid washes and dry downs on a 98°C hotplate. After complete digestion through either the hotplate or a combination of hotplate and microwave procedures, samples were dried down on a 98°C hotplate and then brought up in 2% trace metal grade nitric acid.

2.4 ICP-AES and XRF elemental ratios

Digested samples were diluted in 2% once distilled trace metal grade nitric acid and analyzed in the UTA Shimadzu Center for Environmental, Forensics, and Material Science on a Shimadzu plasma atomic emission spectrometer ICPE-9000 (ICP-AES). Additional analyses were performed at The Ohio State University (OSU) in the Trace Element Research Laboratory on a PerkinElmer optical emission spectrometer Optima 8300 DV. Digested residual samples were analyzed for barium (Ba) and aluminum (Al) to reconstruct Ba/Al ratios. Digested bulk samples were also analyzed for titanium (Ti) to reconstruct Ba/Ti ratios. In bulk sediment Ba/Al and Ba/Ti are thought to represent the biogenic barium component of the sediment following previous work by Reitz et al. (2004), however this relationship has not been applied to processed sediment residues like those residues from Site 401.

Standard Al solutions for the ICP-AES were 1 ppm, 10 ppm and 100 ppm for barite residues and 10 ppm, 50 ppm and 100 ppm for bulk samples. Standard Ba solutions for the barite residues and the bulk samples were 10 ppb, 1 ppm and 10 ppm. Standard Ti solutions contained trace hydrofluoric acid and were 0.05 ppm, 0.1 ppm, 0.2 ppm and 0.5 ppm. Calibration curves for the analyzed wavelengths best fit to at least $R^2 = 0.999$ and standards had less than 10% error during the analyses for the bulk samples. Drift correction was calculated from the quality control (QC) standards with known concentrations ("Expected") for some the residual samples processed on the PerkinElmer ICP-AES (Appendix B.3; Eq. 2.1).

$$\textit{Equation 2.1: Drift correction} = \text{QC error} + \frac{\text{the next QC error} - \text{QC error}}{\text{Expected} * (\text{Expected} - (\text{Expected} - \text{sample number}))}$$

Elemental wavelengths were chosen by the lowest percentage error from the quality control standards analyzed every 10 samples within the run. Residue elemental data for Al used the wavelength 394.401 nm and Ba used wavelength 455.403 nm from the PerkinElmer ICP-AES. Bulk sample analysis used the PerkinElmer ICP-AES Al 394.401 nm, Ba 230.424 nm, Ti 368.519 nm

and the Shimadzu Ca wavelength 616.217. Bulk sample concentrations were normalized to incorporate the weight of the initial bulk sediment digested (Eq. 2.2) and barite residue samples were normalized to the weight of of the remaining barite residue that was digested (~20 mg of digested residue) (Eq. 2.3).

$$\text{Equation 2.2: Normalized bulk element} = \frac{\text{ICP} - \text{AES concentration } \left(\frac{\text{mg}}{\text{L}}\right)}{\text{Total digested sample } \left(\frac{\text{mg}}{\text{L}}\right)}$$

$$\text{Equation 2.3: Normalized barite residue element} = \frac{\text{ICP} - \text{AES concentration } \left(\frac{\text{mg}}{\text{L}}\right)}{\text{Digested residue } \left(\frac{\text{mg}}{\text{L}}\right)}$$

XRF Ba, Al, Ti and Ca scans were calibrated from the normalized bulk sample digestions from Site 401 during ETM2 with elemental centered log-ratios (CLR) following Aitchison (1986) and Equation 2.4:

$$\text{CLR element} = \frac{\text{Element raw XRF count}}{(\text{Geometric mean count of all elements analyzed for that sample})^{\left(\frac{1}{\text{number of elements}}\right)}}$$

Comparison of elemental CLR and normalized elements are used to construct linear regression curves (Figure 2.2). Linear regression equations are applied to the CLR transformed XRF scans to calculate weight percentages.

2.5 Age model and accumulation Rates

Age models for the hyperthermal events at the sample site locations were chosen based on their reliability and recommendations from other collaborators on the project (Hull, personal communication; Thomas, personal communication). Accurate age models were required for hyperthermal event placement as well as for calculating barite accumulation rates (BAR) to remove the dilution effect of barite compared to other sedimentary components such as $CaCO_3$. The age models used for Site 1263 were Röhl et al. (2007) for the PETM and ETM3, and Jennions et al. (2015) for ETM2. Röhl et al. (2007) orbitally tuned nondestructive X-ray fluorescence (XRF) core

scans of ODP Sites 1262 - 1267 to precession cycles to update the existing extraterrestrial helium age model by Farley and Eltgroth (2003). Jennions et al. (2015) calculated the relative sediment age from the terrigenous mass accumulation rate, calculated from the dry bulk density (DBD) and $CaCO_3$ weight percent, obtained prior to the onset of ETM2 between Westerhold et al. (2007) precession cycle tie points at 298.52 and 301.52 mcd. The zero-relative age point for ETM2 was set according to Stap et al. (2009).

The age models used for Site 1209 were Penman et al. (2014) for the PETM and Gibbs et al. (2012) for ETM2 through the I event. Penman et al. (2014) correlated the fine fraction $\delta^{13}C$ from Site 1209 with the age models in Röhl et al. (2007) for Sites 1263 and 690. Gibbs et al. (2012) correlated bulk sediment $\delta^{13}C$ tie points for Site 1209 over ETM2 to Site 1262, which was orbitally tuned by Zachos et al. (2010).

Site 1215 relative ages for the PETM were obtained from Leon-Rodriguez and Dickens (2010) who compared calcareous nannofossil assemblages to calcareous nannoplankton bioevents outlined by Agnini et al. (2007). The bioevent ages were orbitally tuned according to Westerhold et al. (2007; 2008). Ages for ETM2 and ETM3 were obtained by E. Thomas (personal communication) through correlation of the CIE from Leon-Rodriguez and Dickens (2010) $\delta^{13}C$ and Lauretano et al. (2015).

The relative position of ETM2 was made through correlation with Site 550 by D'haenens et al. (2014) although ETM3 was most likely not recovered when the core was initially drilled. D'haenens et al. (2014) made the correlation through calcareous nannofossil biozone NP11, benthic foraminiferal assemblage changes and bulk $\delta^{13}C$ and $\delta^{18}O$. Recovery gaps from the initial sediment core drilling and the lack of reliable magnetostratigraphic correlation prevented the definitive assignment of the age model, so data from Site 401 will be presented relative to depth and not ages (D'haenens et al., 2014).

Accumulation rates can be calculated for sites with reliable age models. Linear sedimentation rates (LSR, Eq. 2.5) are calculated for adjacent samples by dividing the difference in sample depths by the difference in sample ages, and multiplying by 100.

$$\text{Equation 2.5 LSR} = \frac{\left((\text{bottom sample depth} - \text{top sample depth}) * 100\right)}{(\text{bottom sample age} - \text{top sample age})}$$

Sample mass accumulation rates (MAR, Eq. 2.6) equal the LSR multiplied by DBD. BAR calculations (Eq. 2.7) equal the MAR multiplied by the barite sample weight divided by the initial, dry sample weight.

$$\text{Equation 2.6: MAR} = \text{LSR} * \text{DBD}$$

$$\text{Equation 2.7: BAR} = \left(\frac{\text{barite weight}}{\text{dry sample weight}}\right) * \text{MAR}$$

Dry bulk density was calculated following the method used by Ma et al. (2014) for the PETM, ETM2 and ETM3 at Site 1215 and for the PETM at Site 1263. Dry bulk density was calculated from the slope of the trend line between the gamma ray density (GR) and the dry density measured on discrete (Moisture And Density or MAD) samples measured on the JOIDES Resolution and both archived in the IODP Janus database (Figure 2.3). The resulting equations were then applied to the GR values to calculate the dry bulk density for each sample. Linear interpolation was used for sample depths that were not listed in Janus.

Calibration of GR values from shipboard MAD data for Site 1209 resulted in no correlation for the PETM and ETM2 through the "I event" ($R^2 = 0.0109$; Figure 2.4). Dry bulk density for all hyperthermal events at Site 1209 were therefore calculated from a calibration of $CaCO_3$ weight percent (Hancock and Dickens, 2005) following Snoeckx and Rea (1994) with Eq. 2.8 for sediment with greater relative abundance of biogenic $CaCO_3$ relative to lithic material.

$$\text{Equation. 2.8: Dry bulk density} = (3.60 - 0.0279 \text{ x } CaCO_3 \text{ weight\%})^{-1}$$

Linear interpolation was used for sample depths that were not listed in Hancock et al. (2005). Dry bulk density for Site 1263 over ETM2 and ETM3 were obtained from linear interpolation from

MAD data in the ODP Initial Reports (Zachos et al., 2004) to match the benthic foraminifera accumulation rates (BFAR) calculated by Jennions et al. (2015).

Benthic and planktonic foraminiferal accumulation rates (BFAR and PFAR) were calculated using the same MAR calculated as described above in Eq. 2.6, with the foraminiferal count divided by the sample weight. Foraminiferal accumulation rates were calculated for the benthic foraminiferal data provided by E. Thomas (personal communication) for ETM2 at Site 1209 and the benthic and planktonic foraminiferal data from Leon-Rodriguez (2012) for the PETM, ETM2 and ETM3 at Site 1215.

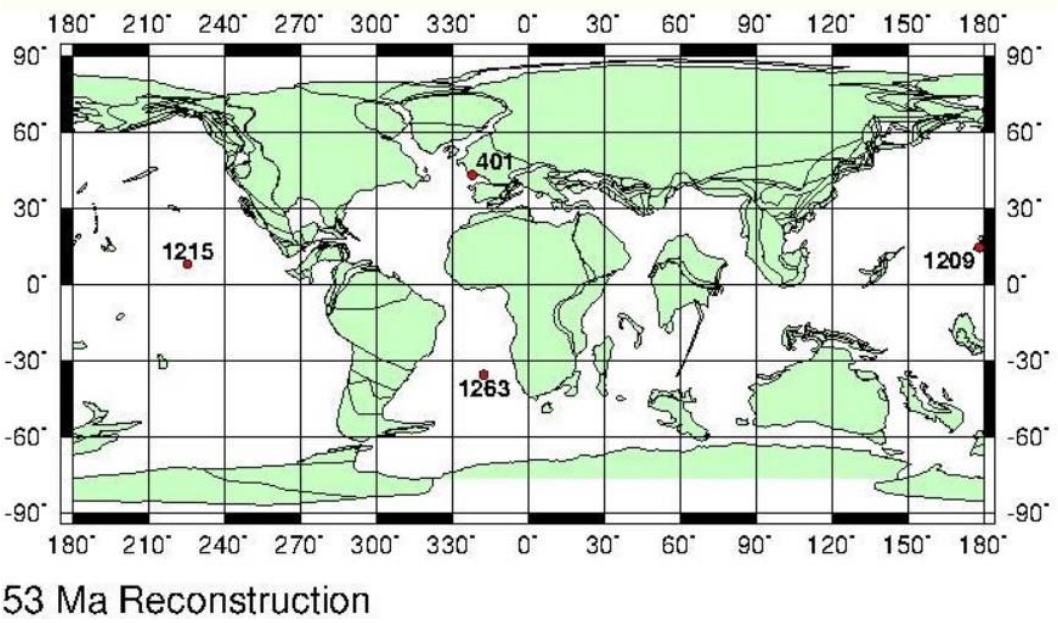

Figure 2.1: Study sample site locations at 53 million years ago (Ma) for ODP Sites 1209, 1215, 1263 and DSDP Site 401. The modern locations for the sites are as follows: ODP Site 1209 is in the western Pacific Ocean southeast of Japan, ODP Site 1215 is in the equatorial Pacific Ocean near Honolulu, ODP Site 1263 is in the southeast Atlantic Ocean along Walvis Ridge, and DSDP Site 401 is off the west coast of France on the North Biscay Margin. Plate reconstructions adapted from Ocean Drilling Stratigraphic Network (ODSN) Paleomap project (http://www.odsn.de/odsn/services/paleomap/paleomap.html).

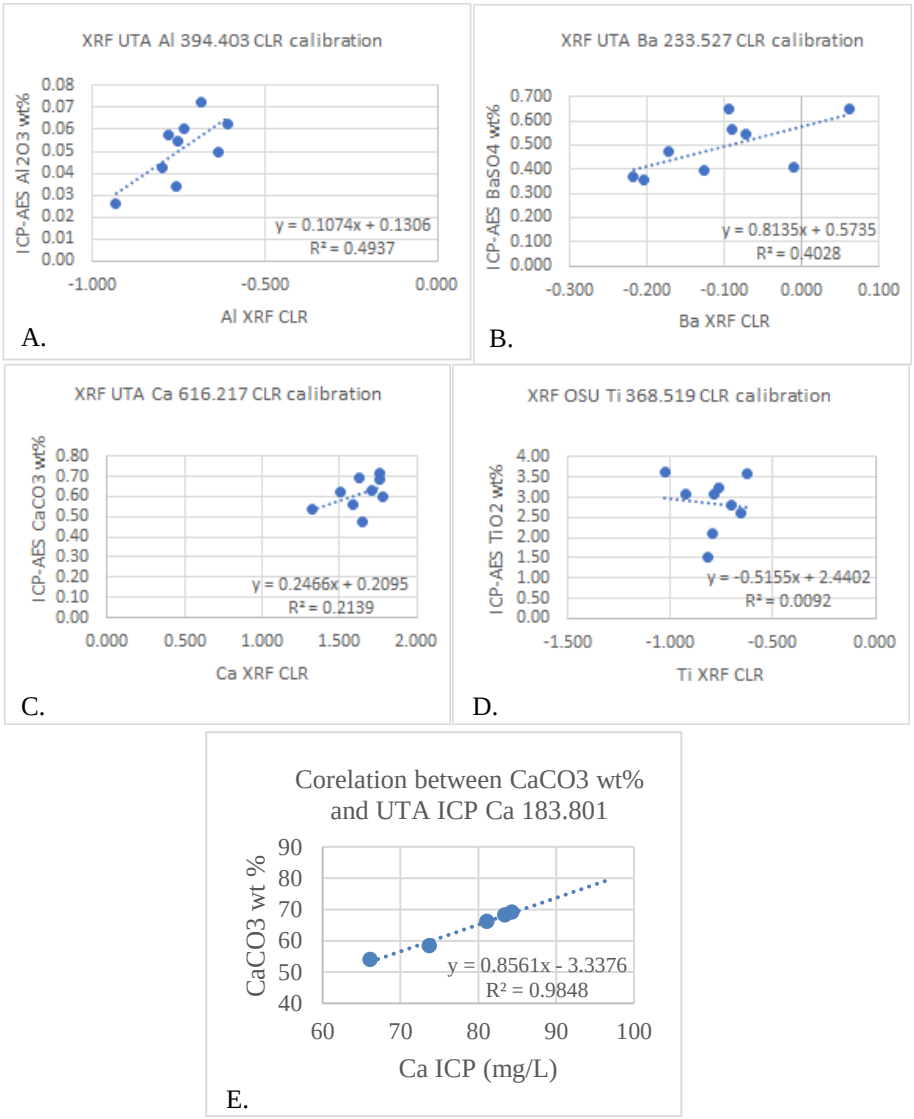

Figure 2.2: XRF Calibration curves for bulk samples from Site 401 ETM2. D'haenens et al. (2014) XRF scans were plotted vs. ICP-AES derived element weight percentages for A. aluminum, B. barium, C. calcium and D. titanium. E. suggests a positive relationship between measured weight percentage and ICP-AES derived weight percentages.

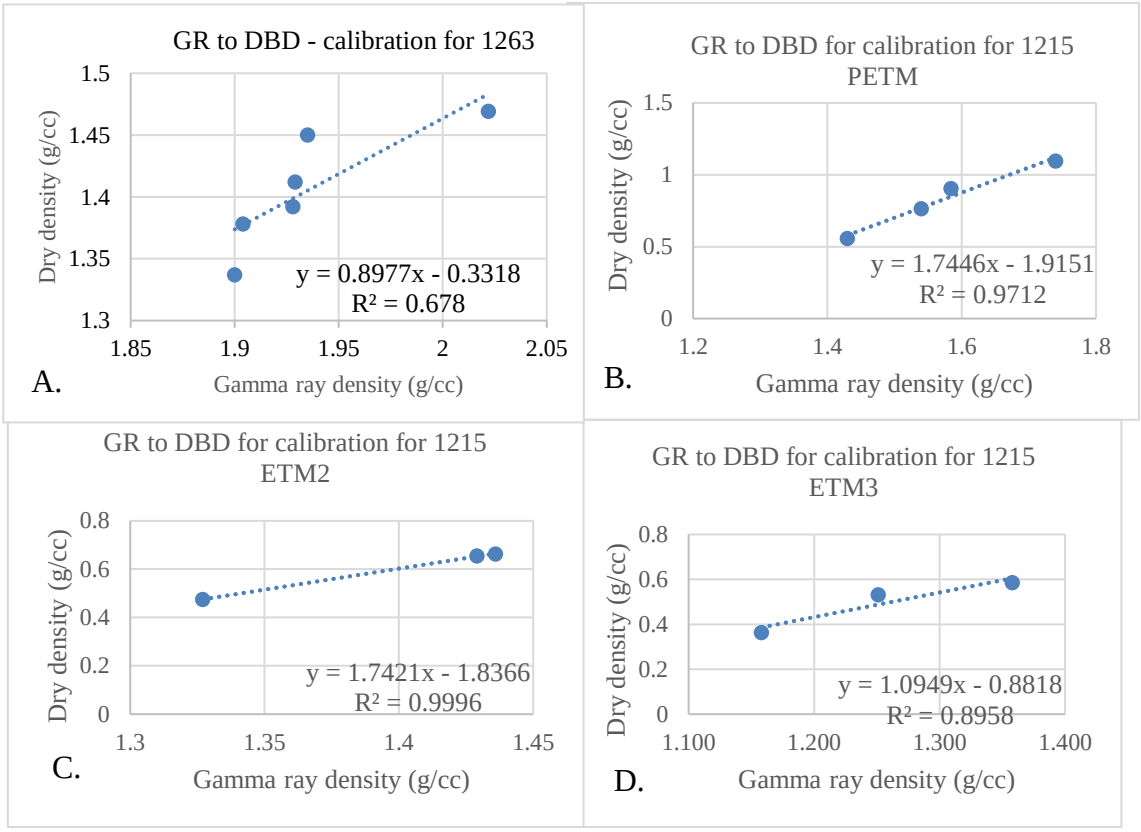

Figure 2.3: Gamma ray density (GR) plotted vs. dry density (DD) calibration curves. DD values were obtained from discrete (Moisture And Density or MAD) samples measured on the JOIDES Resolution and along with GR measurements, DD values are archived in the IODP Janus database. The resulting trend line slopes were applied to the measured GR values to calculate dry bulk density (DBD) for A. ODP Site 1263 for the PETM, and B. ODP Site 1215 for the PETM, C. ODP Site 1215 for ETM2 and D. ODP Site 1215 for ETM3.

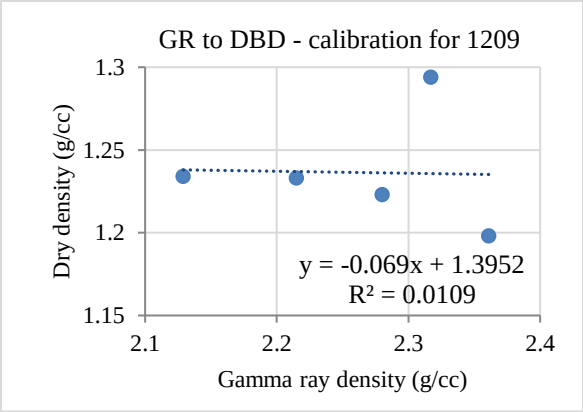

Figure 2.4 Site 1209 Gamma ray density (GR) plotted vs. dry density (DD) calibration. DD values were obtained from discrete (Moisture And Density or MAD) samples measured on the JOIDES Resolution and along with GR measurements, DD values are archived in the IODP Janus database. There appears to be no statistical relationship between the GR and DD measurements ($R^2 = 0.01$) from ODP Site 1209 during the PETM, and ETM2 through the "I2 event", so this method was not used to calculate the dry bulk density (DBD) at this site.

Table 2.1: Sample site location descriptions

	Modern location	Present water depth [m]	Paleodepth [m]
A. DSDP Site 401	47°25.65’N 08°48.62’W	2495	1800 to 2000
B. ODP Site 1209	32°30.1081′N 158°30.3564′E	2387	2400
C. ODP Site 1215	26°01.77´N 147°55.99´W	5396	3300
D. ODP Site 1263	28°31.98′S 02°46.77′E	2717	1500

A. DSDP Site 401 (D’haenens et al., 2014; Montadert et al., 1979), B. ODP Site 1209 (Bralower et al., 2002), C. ODP Site 1215 (Shipboard Scientific party, 2002a), and D. ODP Site 1263 (Zachos et al., 2004).

Table 2.2: Barite separation method modified from Paytan et al. (1996)

1.	Weigh 20-40g of sample into a 250 mL Nalgene container
2.	Dissolve carbonates in 6N hydrochloric acid overnight at room temperature
3.	Perform three DI water rinses after each step
4.	Dissolve organics in hypochlorite overnight at 50°C
5.	Dissolve Fe-Mn oxyhydroxides in 0.02N hydroxylamine in acetic acid overnight at 80°C
6.	Dissolve silicates in 1:2 HF:HNO_3 (1N) overnight at room temperature
7.	Dissolve in 1:1 HF:HNO_3 (1N) overnight at room temperature
8.	If necessary, Dissolve in 2:1 HF:HNO_3 (1N) overnight at room temperature
9.	Dissolve fluorides with saturated aluminum chloride (in 1N nitric acid) for 1 hour at 80°C
10.	Filter and dry overnight, examine under SEM for purity after weighing
11.	Weigh then ash samples in 700°C furnace, weigh again

Table 2.3: Sealed vial acid digestion procedure modified from Scudder et al. (2014)

1.	Label a 25 mL acid cleaned Savillex Teflon digestion vessel using a Staedtler Lumocolor pen
2.	Add 1 mL of concentrated Nitric Acid to each Teflon vessel
3.	For each sample weigh out 0.0198-0.0202 g of powder, record the weight and pour into the Teflon vessel
4.	Add an additional 2 mL of concentrated Nitric Acid
5.	Add 1 mL concentrated Hydrochloric Acid to each vessel, seal tightly and let sit ~1hr
6.	Add 1 mL concentrated Hydrofluoric Acid to each vessel. Seal very tightly and cook on hotplate, sub-boiling ~24hrs.
7.	Place in ultrasonicator filled with water up to the level of the samples inside the Teflon vessels. Sonicate for ~60 mins.
8.	Slowly (drop-by-drop) add 1 mL of Hydrogen Peroxide to each vessel, leave uncapped until samples stop reacting. Reseal vessels and place back on hotplate for ~4-6 hrs.
9.	Add another 1 mL of Hydrogen Peroxide to each vessel, reseal vessels and place back on hotplate for up to 5 days or until total sample dissolution
10.	Uncap vessels, using squeeze bottle with MQ, clean cap dumping MQ back into the vessel. Place caps face down on clean TechCloth.
11.	Put open vessels on hotplate taking note of where each one is located. Cook until samples are fully dried (~8 hrs).
12.	Add 1 mL of concentrated Nitric Acid to re-dissolve dried sample. Let sit for ~5 hrs.
13.	Sonicate (~30 mins) and add 0.5 mL of Hydrogen Peroxide if needed
14.	Dilute to 60 g (3000x dilution) following dilution protocol

Table 2.4: Sealed vial acid microwave digestion procedure modified from

Murray and Leinen (1996)

1.	Label a 60 mL acid cleaned Savillex buttress threaded top Teflon digestion vessel using a Staedtler Lumocolor pen
2.	Add sample, 2.0 mL concentrated Nitric Acid and 5.0 mL concentrated Hydrofluoric Acid
3.	Wrap 3 times around the Teflon vessel threads with Teflon tape or PTFE thread seal tape (plumber's tape) then seal the vials tightly by hand with the rubber gripper and the wrench to at least a quarter turn. Place the vessels into a round Tupperware container together, cover the top with Saran wrap and seal the cover. Place an uncovered, wide mouth, 250 ml HDPE bottle of DI water in the back of the microwave behind the Lazy Susan.
4.	Microwave in the fume hood with the sash all the way down for 1 min at Power 10, and 4 more times at 15 min intervals on Power 2
5.	Microwave in the fume hood for 30 mins on Power 2 and 30 mins on Power 2. Carefully remove the samples and dry down overnight on a hot plate
6.	Add 4.0 mL of concentrated Nitric Acid and dry down
7.	Add 3.0 mL of concentrated Hydrochloric Acid and 1.0 mL concentrated Nitric Acid and dry down
8.	Add 2.0 mL of concentrated Nitric Acid and dry down
9.	Add 2.5 mL concentrated Nitric Acid and dry down
10.	Add 1 mL of concentrated Nitric Acid to re-dissolve dried sample. Let sit for ~5 hrs.
11.	Sonicate for 1 hour or until total sample dissolution
12.	Dilute to 60 g (3000x dilution) following dilution protocol

Chapter 3

Results

3.1 ODP Site 1263

Site 1263 has the highest BAR values up to 6 mg/cm^2*kyr during the PETM beginning at the onset of the CIE recorded in bulk carbonate (Zachos et al., 2005) to approximately 88 thousand years (ky) after the initiation of the PETM (Figure 3.1A; Table A.3; Ma et al., 2014; this study). Prior to the PETM, BAR ranged between 0 (or undetectable) and 0.2 mg/cm^2*kyr with a single high value of about 3 mg/cm^2*kyr at 17 kyr before the onset of the CIE (Ma et al., 2014; this study). An extended BAR period of high values occurs from about 28.5 to 64 kyr occurs during the CIE, and another BAR increase occurs at 87.6 kyr, during the δ^{13}C rebound. After 87.6 kyr, BAR is generally lower and more variable.

There are two BAR peaks during ETM2 (Figure 3.1B; Table A.2). A single BAR point of about 2.2 mg/cm^2*kyr occurs 15.5 kyr after the onset of ETM2 as defined by benthic foraminiferal δ^{13}C (Stap et al., 2010) and a more defined BAR increase ranging from 1.5 to 2.3 mg/cm^2*kyr exists during the δ^{13}C recovery between 66 and 83 kyr after the onset of the CIE. IODP was not able to provide samples for barite processing from the CIE minimum between 35.5 and 66.3 kyr after the CIE onset, but BAR clearly increases while δ^{13}C rebounds.

There are also two BAR increases around ETM3 (Figure 3.1C; Table A.1) as defined by benthic foraminiferal δ^{13}C (Röhl et al., 2005), with the largest increase in BAR of approximately 1.4 mg/cm^2*kyr just after the CIE minimum from 11.7 kyr to about 24 kyr after the onset of the CIE. Prior to ETM3 a BAR peak of approximately 1.1 mg/cm^2*kyr occurs at 25.4 kyr before the onset of the CIE. The highest BAR values from ETM3 are about 1 mg/cm^2*kyr lower than ETM2. The highest PETM BAR values are about 3 times larger than the other two, smaller hyperthermals.

3.2 ODP Site 1209

BAR at Site 1209 reaches its highest level of ~0.12 mg/cm^2*kyr 13 kyr before the onset of the PETM (Figure 3.2A; Table A.6; Ma et al., 2014; this study). BAR levels throughout the PETM are much higher than the baseline values prior to the event of nearly zero. There is a general increase in BAR (Ma et al., 2014; this study) while the bulk carbonate $\delta^{13}C$ decreases to the CIE minimum at 23 kyr after the onset of the PETM at Site 1209 (Gibbs et al., 2012). The highest BAR levels during the PETM of about 0.1 mg/cm^2*kyr decrease during the $\delta^{13}C$ recovery from about 23 to 47.5 kyr after the onset of the PETM.

During ETM2, H2 and the following I2 event, BAR peak values between 0.2 and 0.7 mg/cm^2*kyr are higher than the PETM (Figure 3.2B; Tables A.4 and A.5). After the onset of ETM2, BAR increase when bulk carbonate $\delta^{13}C$ values decreased, but BAR values are low to undetectable after the onset of the I1 event approximately 400 kyr after the onset of ETM2 (Figure 3.2B). The highest BAR values near ETM2 occur at 31 to 15.7 kyr prior to the onset of ETM2 (0.22 and 0.25 mg/cm^2*kyr). High BAR values also occur after H2 from ~ 150 to 230 kyr after the onset of ETM2 (0.29 to 0.58 mg/cm^2*kyr). After the onset of the I2 event BAR fluctuates between 0 (or undetectable) and then jumps up to 0.9 mg/cm^2*kyr at the end of the record.

3.3 ODP Site 1215

Site 1215 BAR levels are generally low before and after the PETM CIE (Figure 3.3A; Table A.9: Ma et al., 2014; this study), except at 150 kyr before the onset of the PETM. After the onset of the PETM, barite values generally increase up to around 8 mg/cm^2*kyr while bulk carbonate $\delta^{13}C$ decreases (Leon-Rodriguez, 2012). Maximum BAR (8.2 mg/cm^2*kyr) occurs 31 kyr after the onset of the PETM, approximately coinciding with the CIE minimum. Approximately 80 kyr after the onset of the PETM, BAR return to the pre-PETM values that range from undetectable to 0.04 mg/cm^2*kyr.

Barite was only recovered from two sample depths around ETM2 (Figure 3.3B; Table A.8), one before and one after the onset of ETM2. Three samples around ETM3 recovered barite (Figure 3.3C; Table A.7), one before and two after the onset of ETM3 as defined by the bulk carbonate $\delta^{13}C$ (E. Thomas, personal communication; Figure 3.3C). The largest BAR of 0.02 mg/cm^2*kyr from samples covering ETM2 occurs before the CIE when $\delta^{13}C$ is high. The second barite peak occurs during the CIE recovery. The largest BAR detected in samples covering ETM3 occur after the CIE. BAR peaks are 0.05 and 0.02 mg/cm^2*kyr, when bulk carbonate $\delta^{13}C$ is high. Barite recovery during the PETM was significantly larger than the smaller hyperthermal events, which had only a few grains per sample or undetectable quantities using the current method.

Site 1215 had 11 samples with a large proportion of chert that was not dissolved by the barite separation method (starred samples in Figure 3.3). Two chert samples were observed after the PETM (Figure 3.3A), three were found in the barite peak during the recovery of ETM2 (Figure 3.3B), and four throughout ETM3 (Figure 3.3C). Potential siliceous microfossils were found in the barite residue of some of the cherty samples including what appears to be coccolithophores genus *Discoaster* that were observed under the SEM to be replaced by silica (Figure 3.4).

3.4 DSDP Site 401

Bulk digestion sediment Al, Ba, Ca, and Ti concentrations from Site 401 over ETM2 generally match the raw XRF scans (Figure 3.5A; Table B.1). Barium concent is generally low when $\delta^{13}C$ values are high with two peaks of ~0.9 μg Ba/mg sample, one prior to the onset of ETM2 and one near the CIE minimum. After the onset of ETM2, Ca initially decreases to 0.2 mg Ca/mg sample before the onset of ETM2, then has a relatively small peak (0.2 mg Ca/mg sample) when Ba, Al and Ti are at the lowest values during ETM2. Gradual recovery of Ca content to pre-ETM2 levels coincide with increasing $\delta^{13}C$ values. Similar to the Ba content curve, Al and Ti content have a peak prior to the onset of ETM2 and another peak near the CIE minimum. Peak Al content before the onset of ETM2 is 0.03 mg Al/mg sample, but the highest Al content is near the CIE minimum (0.04

mg Al/mg sample). Prior to the onset of ETM2, Ti content has a 1.6 μg Ti/mg sample peak but the largest Ti content (1.7 μg Ti/mg sample) occurs near the CIE minimum.

Bulk elemental ratios of Ba/Al and Ba/Ti (Figure 3.5B; Table B.1) generally decrease to their lowest values (0.02 and 0.4 respectively) at 190.1 mbsf near the ETM2 CIE minimum, where Ba, Al and Ti content are the lowest. Peak Ba content at ~190.0 mbsf is only reflected in Ba/Ti ratios as a 0.1 increase. Barium elemental ratios generally increase while $\delta^{13}C$ values increase but to nearly half the pre-ETM2 levels.

Digested barite residues were separated from 20 to 38 g of dry bulk sediment (Table B.3), but interestingly barite residue concentrations have lower normalized Ba concentrations than the bulk sediment samples even though they dissolved the same amount of sample, i.e., 20 mg (Figure 3.6A). The largest Ba peak in the barite residues (~16 μg Ba/mg residue, two orders of magnitude higher than the other residue concentrations) was after the onset of ETM2, near a low in the bulk sediment Ba concentration but also close to a Ba XRF peak. It should be noted that the high barite residue sample interval was not chosen for the bulk digests, but should be looked at further in future work. Therefore, it is possible that the highest Ba content from the barite residue reflects a valid maximum barite concentration. Al content in the barite residue samples during ETM2 generally agree with Al XRF scans. However, peak Ba/Al values in the barite residue occurs when bulk Ba/Al and Ba/Al XRF are low after the onset of ETM2 (Figure 3.6B).

Barite residue digestions were performed on samples before and after the PETM that can be found in Table B.4, but these samples are outside the hyperthermal event and therefore are not discussed. Barite residues were not analyzed for Ti due to the accumulation of refractory rutile and anatase grains in residues which resulted in Ti concentrations that oversaturated the ICP-AES wavelengths for Ti.

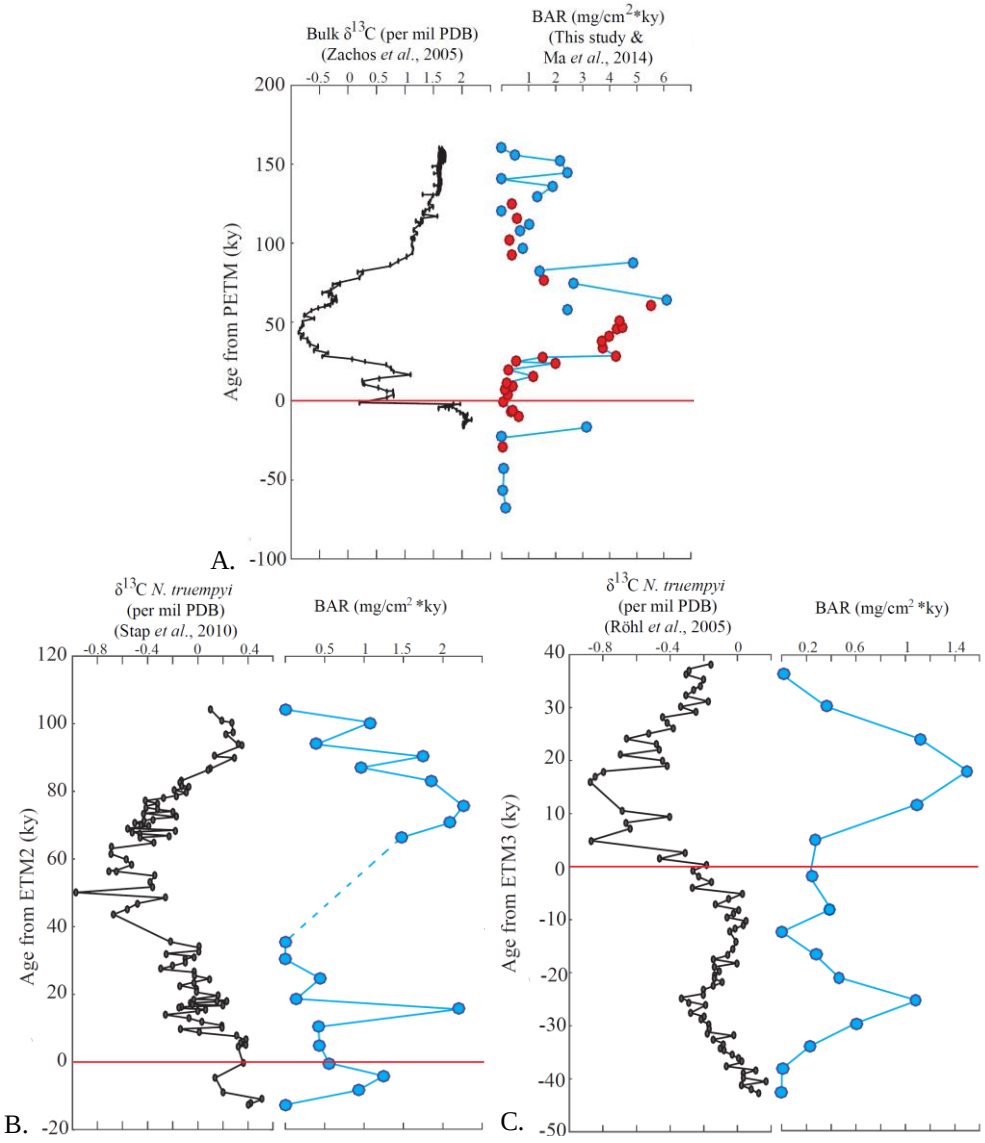

Figure 3.1: Site 1263 barite accumulation rate (BAR) and $\delta^{13}C$. BAR (blue line) from A. the PETM (red circles from Ma et al. (2014); blue circles from this study), B. ETM2 (dashed blue line represents a gap in the processed samples obtained from the Bremen Sample Repository) and C. ETM3. The red line indicates the onset of the hyperthermal events according to A. and C. Röhl et al. (2007), and B. Jennions et al. (2015).

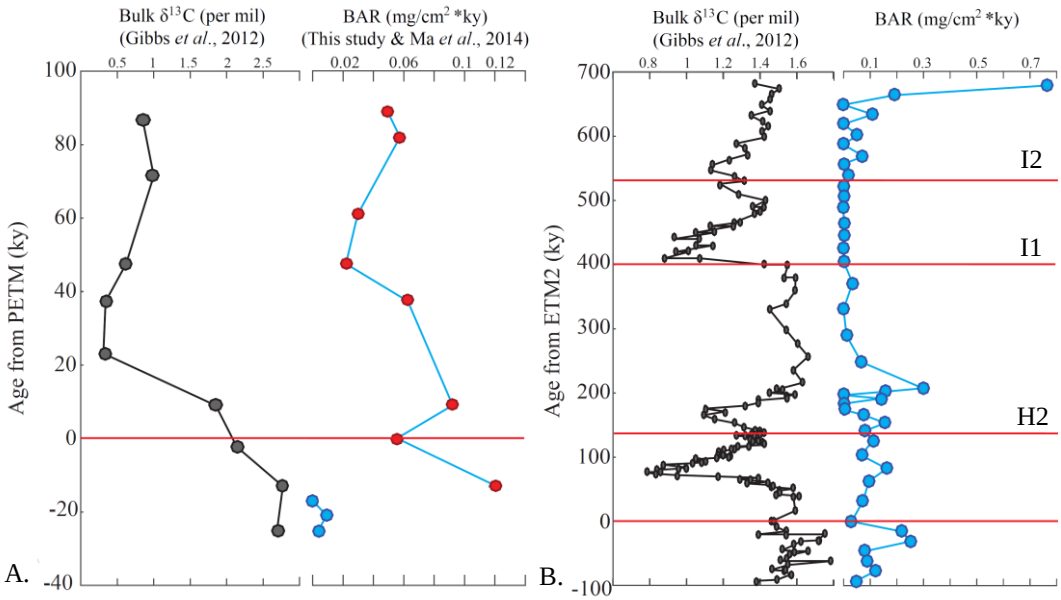

Figure 3.2: Site 1209 barite accumulation rate (BAR) and bulk carbonate $\delta^{13}C$. Barite accumulation rates (BAR, blue line) from A. the PETM (red circles from Ma et al. (2014); blue circles from this study), and B. ETM2. The red line indicates the onset of the hyperthermal events according to A. Penman et al. (2014) and B. Gibbs et al. (2012) with absolute ages from the onset of ETM for H2 (100 kyr), I1 (400 kyr), and I2 (530 kyr) from Zachos et al. (2010).

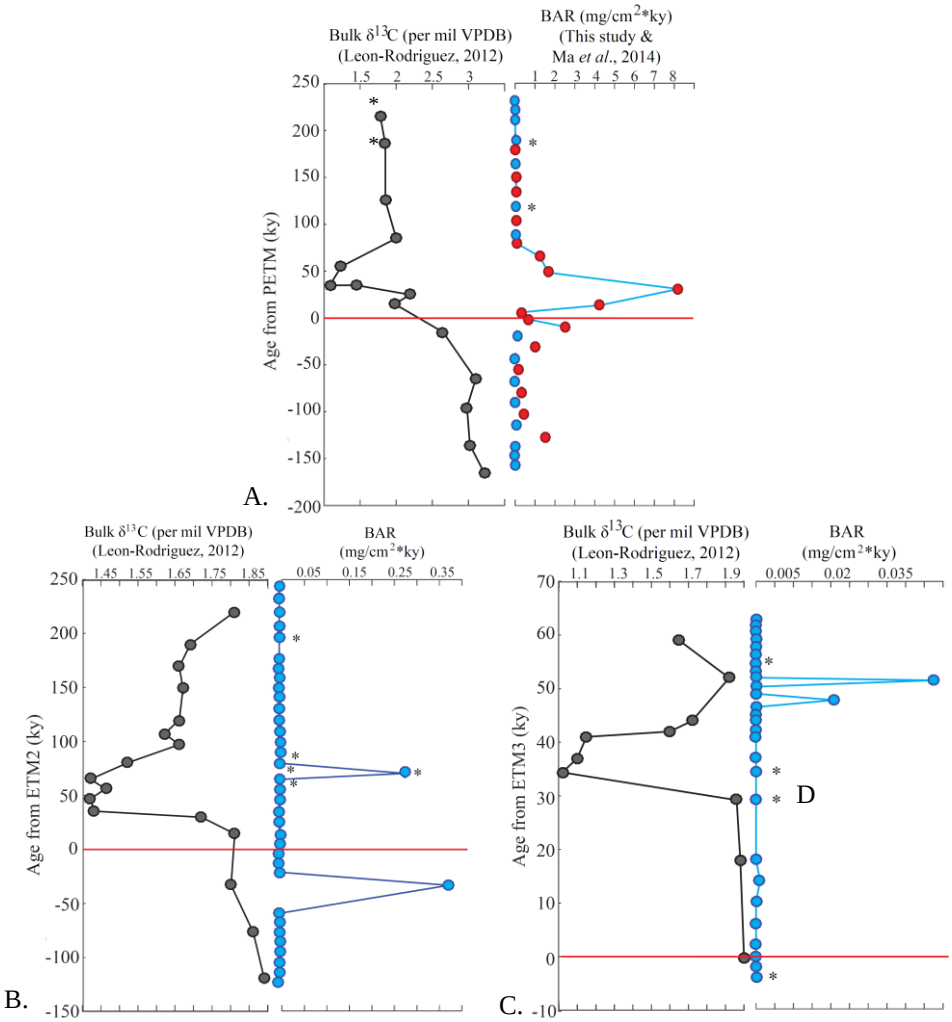

Figure 3.3: Site 1215 barite accumulation rate and bulk carbonate $\delta^{13}C$. Barite accumulation rates (BAR, blue line) from A. the PETM (red circles from Ma et al. (2014); blue circles from this study), B. ETM2, and C. ETM3. The red line indicates the onset of all three hyperthermal events according to E. Thomas (personal communication). Additional study sample labels include a large proportion of chert (*) and potential Discoaster coccolithophores (D) in residues after barite separation.

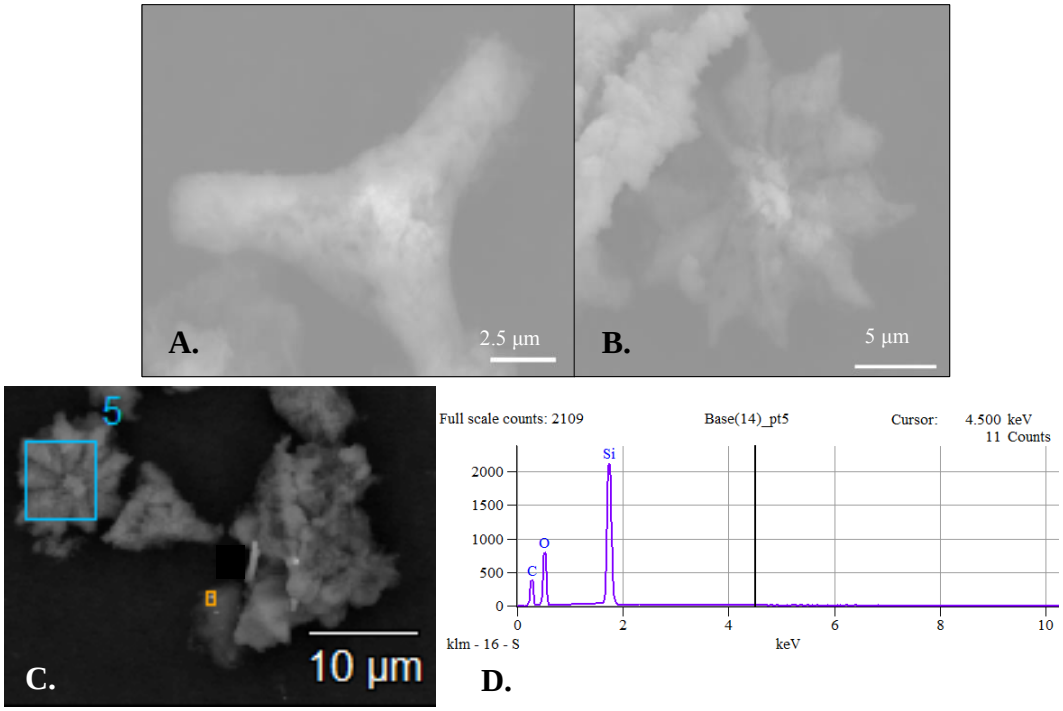

Figure 3.4: Potential nannoplankton tests observed in residue after barite separation at Site 1215. Images from sample Site 1215 4H6 94.5 – 96.5 cm (28.645 mbsf, ~29 kyr after the onset of ETM3 according to E. Thomas (personal communication)) from ETM3 (A and B) obtained with a Hitachi S-3000N scanning electron microscope (SEM) in scanning electron (SE) mode. SEM image of a different grain from the same sample with C. Backscatter electron (BSE) mode and D. energy-dispersive X-ray spectroscopy (EDS) of the blue square in C. collected using Thermo NSS Spectral Analysis software. Images B and C resemble the calcareous ($CaCO_3$) coccolithophore genus Discoaster if it had undergone diagenetic siliceous (SiO_2) recrystallization.

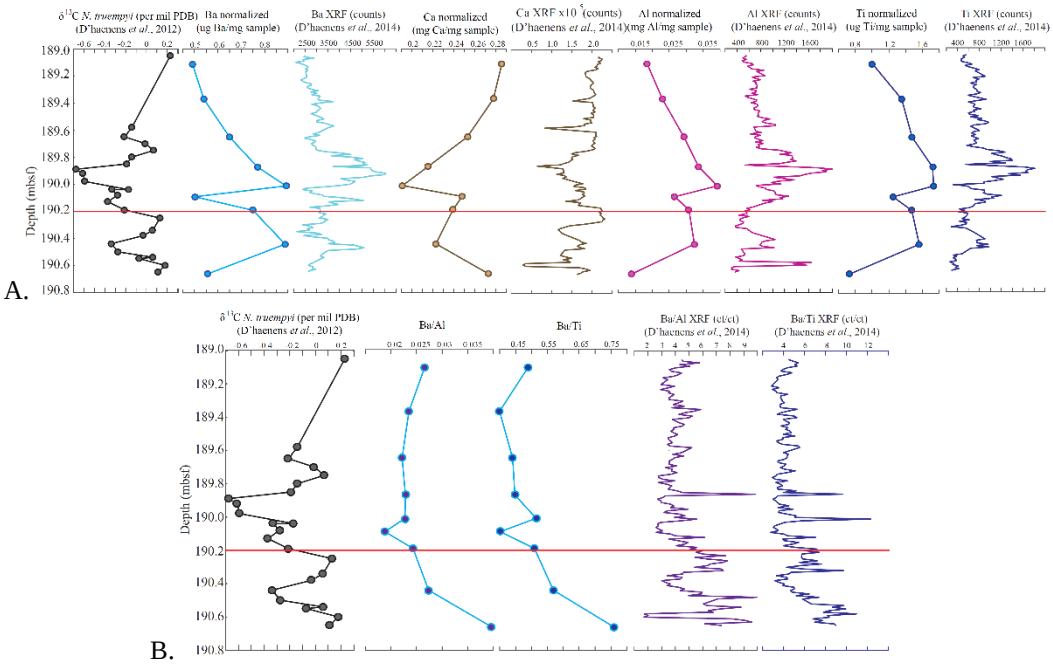

Figure 3.5: Site 401 ETM2 bulk sample ICP-AES and XRF data. A. Alignment of concentrations for Ba, Al and Ti obtained on the PerkinElmer optical emission spectrometer Optima 8300 DV and Ca was obtained from a Shimadzu plasma atomic emission spectrometer ICPE-9000. Relative onset of ETM2 (red line) from D'haenens et al. (2014). B. comparison of elemental ratios Ba/Al or Ba/Ti concentrations and XRF scans.

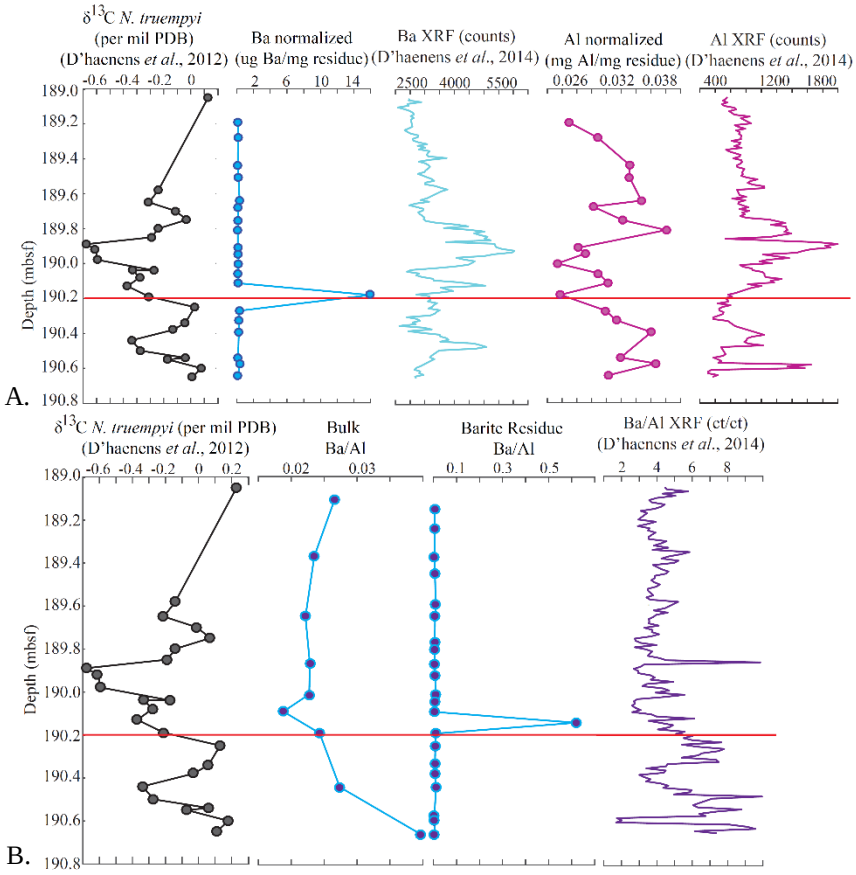

Figure 3.6: Site 401 ETM2 barite residue samples and XRF data. A. Normalized barite residue concentrations for Ba and Al obtained on the PerkinElmer optical emission spectrometer Optima 8300 DV. B. Comparison of bulk sediment, barite residue and XRF Ba/Al ratios. Relative onset of ETM2 (red line) from D'haenens et al. (2014). Elemental ratios of Ba/Al and Ba/Ti in bulk sediment could be related to the biogenic barium component of the sediment similar to previous work by Reitz et al. (2004), but this relationship has not been applied to residual barite sediment.

Chapter 4

Discussion

Marine pelagic barite precipitates during the decomposition of detrital organic matter (Bernstein et al., 1992; Bishop, 1988; Goldberg and Arrhenius, 1958) and has been used as a proxy for export production due to the positive, proportional correlation between pelagic barite accumulation and POC flux (Paytan and Griffith, 2007). Most of the POC is remineralized in the euphotic zone, the remaining POC sinks from the euphotic zone to the deep sea, and ~1% of the POC is deposited in sediments. Highest barite concentrations in the water column barite concentrations occur in oxygen minimum zones, indicating a relationship between barite formation and decomposition of organic matter (Dehairs et al., 1980, 1991, 1992) and not from terrestrial or crustal material (Dymond et al., 1992). In this discussion, export production variations for Sites 690, 1209, 1220, 1221 and 1263 are inferred from BAR changes unless otherwise stated.

4.1 Export production during early Eocene hyperthermal events

Generally, CIE magnitude for each Eocene hyperthermal event and export production are proportional to each other. The PETM has the largest CIE and highest BAR, interpreted to be export production, compared to ETM2 and ETM3 (Figure 4.1; Table 4.1). During the PETM maximum export production occurs when the $\delta^{13}C$ values are at a minimum in all of the studied sites (except in the Western Pacific at Site 1209). This observation is in agreement with the hypothesis that export production increases globally after or close to the minimum CIE peak, as was demonstrated in previous work over the PETM at sites in the Southern Ocean (ODP Site 690; Ma et al., 2014) and the Equatorial Pacific (ODP Sites 1220 and 1221; Ma et al., 2014) shown in Figure 4.2. Export production increased the most during the PETM in the Equatorial Pacific at Sites 1215, 1220, and 1221 (Figure 4.2C-E). Southeastern Atlantic Site 1263 had the next highest regional increase in

export production (Figure 4.2A) followed by the Western Pacific Site 1209 which was almost two orders of magnitude lower than the Equatorial Pacific (Figure 4.2B).

Exported POC from the euphotic zone in the ocean (export production) depends on the surface primary production and the availability of ballasting material for detrital organic matter aggregation (Armstrong et al., 2002). Surface primary production requires micro- and macronutrients and sunlight for photosynthesis (Berger et al., 1989; Falkowski et al., 1998).

While there is not an agreement on which mechanism(s) caused the onset of the PETM, there is a general consensus that it required large amount of isotopically light carbon such as CO_2 and/or methane, which oxidizes to CO_2. Large amounts of dissolved CO_2 increase photosynthetic rates and nutrient consumption in some phytoplanktonic genera (e.g., Fu et al., 2007; Wolf-Gladrow et al., 1999). Increased photosynthetic rates and nutrient consumption results in increased phytoplankton productivity and biomass.

Increase in CO_2 radiative forcing led to a global surface temperature rise of ~5°C to 8°C during the PETM (Dunkley-Jones et al., 2013; Sluijs and Dickens, 2012). Eppley (1972) laboratory studies showed that marine phytoplankton growth rates doubled for every 10°C temperature increase up to 40°C. Positive correlations have also been determined between increasing temperature and increased heterotrophic metabolisms in the ocean (e.g., López-Urrutia et al., 2006; Matsumoto, 2007). Simulated surface air temperatures (Figure 4.6A and B) indicate temperature increases of +1.5°C in the Western Pacific (Site 1209), approximately +2.5°C in the Northern and Southeastern Atlantic (Site 401 and 1263) and approximately +3°C in the Equatorial Pacific (Sites 1215, 1220 and 1221) and Southern Ocean (Site 690). Warmer surface temperatures could enhance metabolic activity in the ocean surface resulting in increased primary productivity biomass, but increased stratification would reduce the nutrient supply to the surface.

Elevated levels of atmospheric CO_2 not only raise temperatures but also leads to ocean acidification and $CaCO_3$ dissolution in the ocean during the PETM (McInerney and Wing, 2011;

Zachos et al., 2005). Calcareous surface organisms precipitate $CaCO_3$ in the water column to form their tests so surface ocean acidification can inhibit calcification and reduce the growth of new test chambers (Kelly et al., 2010). Although some coccolithophore genera increased calcification in high CO_2 environments during laboratory studies (Holcomb et al., 2014; Iglesias-Rodriguez et al., 2008).

Planktonic productivity also requires a sufficient supply of nutrients to the surface ocean, but reduced ocean circulation during the PETM (Sexton et al., 2011) likely decreased upwelling of nutrients. Low nutrient levels would limit the extent of high productivity areas from present day (Figure 1.4) to the narrower regional extent during the PETM (Figure 4.6C; Winguth et al., 2012). Changes in surface conditions that promote surface productivity, such as elevated microbial metabolisms and photosynthetic rates, will not change surface productivity if insufficient nutrient levels are limiting new biomass production (Stoll et al., 2007).

Over the PETM coccolithophore primary productivity was relatively unchanged in the Western Pacific at Site 1209 (Stoll et al., 2007) and there were increased oligotrophic planktonic foraminifera (Petrizzo, 2007). Coccolithophore production increased in the Southern Ocean at Site 690 (Stoll et al., 2007) and there were also were major planktonic foraminiferal population shifts to oligotrophic, warm seawater taxa (Bralower, 2002). Planktonic foraminiferal accumulation rates (PFAR) remained low after the onset of the PETM at Equatorial Pacific Site 1215 until after the PETM CIE minimum (Figure 4.2C; Leon-Rodriguez, 2012). Deformed calcareous nannoplankton tests were recovered from the sediment deposited during the PETM in the Southeastern Atlantic Site 1263 but also $CaCO_3$ dissolution reduced nannoplankton preservation at the site (Raffi and Bernardi, 2008). Surface primary productivity responses to the PETM appear to be variable and regionally specific but increased warm water, oligotrophic planktonic foraminifera at some of the sites indicate surface conditions that were not conducive to high primary productivity and thus surface production and therefore the amount of POC was likely low in the surface ocean during the PETM.

Particulate organic carbon sinks from the euphotic zone to the thermocline where most of the POC is remineralized and the remaining ~1% refractory material is exported to the deep ocean as export production. Export production efficiency can be changed by alteration of the availability of ballasting material. Primary ballasting material in the deep sea in the modern ocean is $CaCO_3$ (Klaas and Archer, 2002). Extensive dissolution of $CaCO_3$ during the PETM (Figure 4.2A, C and F; Zachos et al., 2005) would therefore greatly reduce overall ballasting of material in the thermocline, resulting in longer residence times in the thermocline and possibly increased barite formation as hypothesized by Ma et al. (2014) and reduced carbon export to the seafloor.

Sediment $CaCO_3$ weight percentages during the PETM were reduced to less than 10% at most of the sites in Figure 4.2 where $CaCO_3$ weight percentage data was available. Site 690 in the Southern Ocean (Figure 4.2F) had $CaCO_3$ weight percentage reduced from about 90% before the PETM to approximately 55% during the CIE minimum. The Southern Ocean experienced the greatest temperature increase during the PETM (Figure 4.6F) but less intense $CaCO_3$ dissolution than the other sites in Figure 4.2. Strong $CaCO_3$ dissolution from ocean acidification could have potentially limited the growth and production of calcareous phytoplankton (Kelly et al., 2010).

During the PETM high $CaCO_3$ dissolution from ocean acidification combined with reduced upwelling of surface nutrients (Sexton et al., 2011) resulted in the harsh surface conditions that increased oligotrophic planktonic foraminifera at some of the sites such as Site 690 in the Southern Ocean (Bralower, 2002). Unchanged or low primary production but still high export production could therefore be the result of increased primary production from soft bodied, microscopic organisms such as cyanobacteria. Some cyanobacteria genera have increased photosynthetic rates and metabolisms from high levels of CO_2 and warm SSTs (Fu et al., 2007). High levels of microbial phytoplankton, such as cyanobacteria, are associated with abundant, sticky transparent exopolymer particles (TEP) that readily form aggregates (Alldredge et al., 1993; Engel, 2000; Passow, 2002a, 2002b). Increased photosynthetic microbial activity during high CO_2 concentrations and high SSTs

can increase TEP amounts (Engel et al., 2004) and therefore increase aggregation and POC formation (Riebesell et al., 2007), even if other shelled phytoplankton productivity low. High aggregation and high POC results in high export production.

Export production during ETM2 was highest in the study samples from the southeastern Atlantic, which was an order of magnitude higher than both the Western and Equatorial Pacific (Figure 4.1B). Southeastern Atlantic export production during ETM3 was approximately half the amount of ETM2 and a quarter that of the PETM, while in the Equatorial Pacific export production was an order of magnitude smaller then ETM2 (Figure 4.1C). Site 1209 in the Western Pacific has higher export production during the CIE minimum during ETM2 than during the PETM, however the highest export production value for this site was before the onset of ETM2, which did not generally coincide with low $\delta^{13}C$ values. Elevated export production also occurs prior to the onset of the Eocene hyperthermal events, some of which coincide with periods of low $\delta^{13}C$ clearly seen 25 kyr prior to initiation of ETM3 in the Southeastern Atlantic Site 1263 (Figure 4.1G).

Similar to the PETM, at ETM2 and ETM3 maximum export production occurs when the $\delta^{13}C$ values are at a minimum in the studied sites (Figure 4.1 D, E, G and I) except for Equatorial Pacific Site 1215 (Figure 4.2). At Site 1215, export production is elevated when $\delta^{13}C$ is at its lowest value during ETM2, although it is not the maximum value.

Diagenetic alteration at Site 1215 in the equatorial Pacific could potentially have impacted barite preservation during ETM2 and ETM3 suggesting that an accurate barite signal was not preserved in sediment deposited during these events. Several chert horizons were encountered during the drilling of Site 1215 which disrupted the drilling process and sediment cores that include ETM3, ETM2, and possibly a portion during the recovery of the PETM (Shipboard Scientific Party, 2002a). Radiolarian ooze and thin chert layers were reported during the early Eocene at nearby Site 1220, which was part of the same ODP Leg 199 in the Equatorial region (Figure 4.4; Shipboard Scientific Party, 2002b).

Chert horizons in this region during the early Eocene are likely the result of diagenesis of siliceous radiolarians. Furthermore, significant amounts of chert fragments present in some of the samples collected in this project could be the result displaced chert fragments that were pushed up the core (Hull, personal communication). Potentially replaced coccolithophores present in barite residue from Site 1215 from ETM3 (Figure 3.4) indicates post-depositional diagenic alteration of the sediment. Numerous chert fragments were present in many of the Site 1215 samples from ETM2 and ETM3, several of which required an additional separation step for removal (Figure 4.1, indicated by *). Compelling evidence of post-depositional alteration coinciding with poor barite recovery from ETM2 and ETM3 at Site 1215 (Figure 4.1) suggest that an accurate barite signal was not preserved in sediment deposited during these events.

Similar to the PETM CIE ($\delta^{13}C$ -2.5‰ to -5‰ and +5°C to 8°C; Dunkley-Jones et al., 2013; Sluijs and Dickens, 2012) atmospheric pCO_2 increased during ETM2 as evident from the CIE ($\delta^{13}C$ -1.4‰) and ETM3 ($\delta^{13}C$ -0.8‰) contributing to a surface temperature increase of 3°C during ETM2 and ETM3 +2°C (Stap et al., 2010). Temperature increases are not as high as the PETM but they would have increased enough to cause ocean acidification and reduced deep ocean circulation (Jennions et al., 2015; Zhang et al., 1999).

Coccolithophore productivity during ETM2 was reduced in the Western Pacific at Site 1209 (Dedert et al., 2012) event though coccolithophore productivity were relatively unchanged during the PETM (Stoll et al., 2007). Equatorial Pacific Site 1215 PFAR remained low until after the CIE minimum during ETM2 (Figure 4.7C) and ETM3 (Figure 4.7E), which matches the PFAR trend in the PETM (Figure 4.2C; Leon-Rodriguez, 2012). PFAR decreased in the Southeastern Atlantic at Site 1263 (Figure 4.7B) after the onset of ETM2 (Jennions et al., 2015) which had better preservation of $CaCO_3$ microfossils in the sediment than during the PETM (Raffi and Bernardi, 2008). Planktonic foraminiferal counts per gram of sediment in the Northeastern Atlantic (Site 401)

are variable after the onset of ETM2 but are at relatively higher levels than before the CIE (D'haenens et al., 2012).

Dissolution of $CaCO_3$ occurred during ETM2 and ETM3at most of the sites (Figures 4.2 and 4.7) though it was not as severe as during the PETM. The relatively fast spreading of the East Pacific Rise progressively moved Site 1215 northwest away from the Equator (Ziegler and Murray, 2007), resulting in crustal subsidence of the site during ETM3 to near the CCD (Leon-Rodriguez and Dickens, 2010). Preservation of $CaCO_3$ in the sediment is greatly reduced near the CCD, which could have resulted in the difference of $CaCO_3$ weight percent at Site 1215 during ETM3 compared to the other study sites. Ocean acidification, a rise in sea surface temperature (SST) and reduced ocean circulation were all present during ETM2 and ETM3 but at a lesser degree than during the PETM. Similar to the PETM, coccolithophore and planktonic foraminiferal levels were low during ETM2 and ETM3, therefore high export production during ETM2 and ETM3 was also likely to be the result of increased soft bodied photosynthetic organisms such as cyanobacteria that excrete TEP and enhance aggregation (Alldredge et al., 1993; Engel, 2000; Passow, 2002a, 2002b). Increased photosynthetic microbial activity during high CO_2 concentrations and high SSTs can increase TEP amounts (Engel et al., 2004) and therefore increase aggregation and POC formation (Riebesell et al., 2007) even if other shelled phytoplankton productivity is not high. High aggregation and high POC results in high export production.

4.2 Remineralization rates inferred from export production and benthic foraminiferal data

Reconstructing remineralization rates for the early Eocene hyperthermals are important because increased export production (interpreted from increases in barite accumulation rates) during the CIEs are expected to result in high benthic foraminiferal production. Instead, global benthic foraminiferal extinctions and shifts in dominant genera occurred during the PETM (e.g., Thomas, 2007) and low benthic foraminiferal accumulation rates (BFAR) have been documented during

ETM2 and ETM3 around the globe (e.g., Jennions et al., 2015). Enhanced export production reconstructed from marine barite accumulation rates suggest a greater amount of POC settling from the euphotic zone. In order for low benthic foraminiferal populations to coincide with high export production from the surface, remineralization of POC would have to be at a greater rate than the rate of C export from the surface. Therefore, differences between export production and benthic foraminiferal data can be used to infer remineralization (Jennions et al., 2015).

Benthic foraminiferal data for the PETM in the Southeastern Atlantic at Site 1263 (Site 4.2A), Western Pacific at Site 1209 (Figure 4.2B) and Equatorial Pacific (Figure 4.2C) were represented by the oligotrophic benthic counts due to the low recovery of benthic foraminifera due to the high degree of $CaCO_3$ dissolution at the seafloor during the PETM. Oligotrophic benthic foraminiferal counts increase after the onset of the PETM at all three sites but only at Site 1215 do oligotrophic taxa counts remain high after the CIE minimum. The presence of oligotrophic taxa and reduced overall benthic foraminiferal populations (Figure 4.2E) indicate stressful conditions at the seafloor because these genera are the only ones that can withstand stressful conditions with low nutrients.

Warming events such as the PETM are thought to have reduced deep ocean circulation (Zhang et al., 1999) and lower oxygen solubility (Weiss, 1970) which reduces the dissolved oxygen (DO) to the intermediate and deep ocean. Evidence of low DO concentration was determined through the presence of reduced manganese ($MnCO_3$) and uranium (UO_2) species in the sediment from the Atlantic at shallow (Site 1263), intermediate (Site 1266) and deep (Site 1262) ocean depths during the PETM (Chun et al., 2010). Reduced Mn and U species were also present in sediment from the Northern Atlantic (Site 401) and the Southern Ocean (Site 690) but the Pacific Sites 1209 and 1221 bottom waters remained oxygenated throughout the PETM (Pälike et al., 2014). Evidence for low DO in the Atlantic and Southern Ocean could negatively impact benthic foraminiferal

populations but the well oxygenated Pacific bottom waters would not necessarily affect benthic populations.

Changes in remineralization rates can be inferred from differences in export production and benthic foraminiferal populations as stated previously. High remineralization rates increase the degradation of labile POC and reduce the amount of refractory POC that reaches the seafloor as food for benthic organisms. Therefore, if high remineralization rates occurred at the sites during the PETM (Figure 4.2), it would have reduced the benthic foraminiferal populations while increasing the oligotrophic taxa that tolerate low nutrients levels, especially in the still oxygenated Pacific. The combination of low POC flux from high remineralization and low bottom water oxygenation at the seafloor could have resulted in the global benthic foraminiferal extinctions (e.g., Thomas, 2007).

During ETM2 and ETM3, benthic foraminiferal data for study sites with age models were used to calculate benthic foraminiferal accumulation rates or BFAR (Figure 4.7). Site 401 does not currently have a reliable age model but the benthic foraminiferal counts per gram during ETM2 follow similar general patterns to the other study sites. BFAR was lowest during the CIE minimum after the onset of ETM2 at all the study sites (Figure 4.7). Diagenetic alteration could have affected the BFAR as well as the BAR recorded at Site 1215 during ETM2 and ETM3, but the same overall trend of low BFAR during the CIE minimum was observed. Populations of non-oligotrophic benthic foraminifera require a combination of adequate oxygenation of the deep ocean bottom water and nutrients, and therefore, low BFAR indicate harsh conditions at the seafloor during ETM2 and ETM3, but not as severe as during the PETM.

Global temperature increases of +3°C during ETM2 and +2°C ETM3 (Stap et al., 2010) were not as high as the PETM (Dunkley-Jones et al., 2013; Sluijs and Dickens, 2012) but the temperature increases would be large enough to reduced deep ocean circulation (Zhang et al., 1999) and reduce oxygen solubility (Weiss, 1970). Grain size analysis evidence indicates reduced deep

water circulation near Site 401 and low benthic foraminiferal counts per gram of sediment could be due to local seasonality changes (D'haenens et al., 2012).

Benthic foraminiferal $\delta^{18}O$ values from the Southeastern Atlantic (Site 1263) and Southern Ocean (Site 690) indicate at least +3°C warming in the deep ocean during ETM2 and +2°C during ETM3 (Stap et al., 2010), which results in reduced deep ocean circulation according to early Eocene global climate models (Jennions et al., 2015; Lunt et al., 2010). Increased deep ocean temperatures reduce DO levels but not to the same extent as during the PETM, due to the smaller temperature increases during ETM2 and ETM3. Small changes in DO concentration occurred in the deep ocean during ETM2 and ETM3.

Low quantities of oligotrophic benthic taxa at Site 401 (D'haenens et al., 2012) and deep ocean deoxygenation levels that were not as strong as the PETM suggests that low DO alone are probably not sufficient to completely account for the low BFAR during the smaller scale hyperthermal events. Instead, I suggest that high remineralization rates during ETM2 and ETM3 reduced the amount of POC transported to the seafloor and therefore lowered BFAR.

Microbially mediated remineralization during hyperthermal events would be impacted by the globally increased SSTs and dissolution of $CaCO_3$ ballasting materials. Global modeling simulations of the PETM intermediate seawater depth (~2000 m) temperatures during the PETM indicate a temperatures increase of ~2°C to 2.5°C in the Pacific and 2.5°C to almost 3°C in the Atlantic (Figure 4.8; Winguth et al., 2010). Remineralization occurs in the thermocline at intermediate depths, so warm seawater at intermediate depths during the PETM would enhance microbial metabolisms and result in high remineralization during the PETM, reducing nutrient transport to the seafloor. Atlantic intermediate depth temperatures in the southern hemisphere (Sites 1263 and 690) increased more than in the Pacific (Winguth et al., 2010), which would reduce oxygen solubility (Weiss, 1970) and increase microbial metabolisms although there is no evidence for higher remineralization rates in the Atlantic compared to the Pacific during the PETM.

Remineralization is increased when less ballasting material is available for organic aggregation, so detrital organic matter does not sink as readily. Smaller aggregates of POC have longer residence times in the thermocline, resulting in more time for microbial remineralization of the material. As previously discussed, since the primary ballasting material in the modern deep ocean is $CaCO_3$ (Klass and Archer, 2002), the extensive dissolution of $CaCO_3$ during the PETM would greatly reduce overall ballasting of material. Less ballasting of organic material and longer residence times in the thermocline would therefore increase remineralization as hypothesized by Ma et al. (2014). High rates of remineralization would reduce nutrient transport to benthic foraminiferal populations, and therefore result in low benthic foraminiferal populations.

Warming of SSTs and dissolution of $CaCO_3$ ballasting materials could have both increased microbial remineralization during ETM2 and ETM3. Global modeling simulations of ETM2 intermediate seawater depth temperatures at approximately 2000 m (Figure 4.9) indicate temperatures rises of +0.2 to +0.6°C in the Pacific (Sites 1209 and 1215, respectively) and +1°C in the Atlantic (Sites 401 and 1263; Jennions et al., 2015), approximately 1/3 to 1/4 as much as the PETM (Figure 4.8). Temperature elevations in the intermediate depths during ETM2 (and presumably ETM3) would therefore increase microbial metabolisms, and add to an increase in remineralization rates which reduce POC quantities in the deep ocean and decrease BFAR.

Dissolution of calcareous ballasting material is also thought to have occurred during ETM2 and ETM3, although $\delta^{13}C$ values of ETM2 and ETM3 (-1.4‰ and -0.8‰, respectively; Stap et al., 2010) were less than the PETM (-2.5 to -5‰; Dunkley-Jones et al., 2013; Sluijs & Dickens, 2012) suggesting that ocean acidification would have been less intense than the PETM (Stap et al., 2009). Dissolution of $CaCO_3$ occurred during ETM2 (Figure 4.7A, C and Figure 4.1I) and ETM3 (Figure 4.7E) during the CIE minimums, though not as severely as the PETM at most of the sites except for ETM3 at Site 1215 in the Equatorial Pacific. Decreased availability of calcareous ballasting material in the thermocline increases remineralization rates through longer exposure time of organic material

to microbial mineralization. High remineralization in the thermocline reduces the amount of POC that reaches the seafloor as food for benthic populations, decreasing BFAR.

Potential evidence for high levels of remineralization is the depletion of DO at intermediate seawater depths indicating high oxygen utilization rates (OUR) from microbial respiration. Ocean stratification during the PETM would also have reduced the transport of DO between ocean layers reducing the capacity of the water column to replenish the DO consumed by the remineralization. Low oxygen conditions during the PETM at intermediate seawater depths (1350 to 3300 m) in the Northern Atlantic (Site 401), Southeastern Atlantic (Site 1263) and Southern Ocean (Site 690) were determined through the presence of reduced Mn and U species in the sediment which contrasted to the higher levels of oxygenated species in sediment from deeper sites in the Atlantic (Pälike et al. 2014). Low oxygenation at intermediate ocean depths during the PETM has also been verified through coupled atmospheric-ocean models (Zhou et al., 2016) and the presence of taxa that tolerate low oxygen environments (e.g., Pardo et al., 1997; Yamaguchi and Norris, 2012). Lower oxygen depletion at intermediate depths in comparison to the ocean floor could be due to a combination of low oxygen solubility of warm waters (Weiss, 1970) and enhanced OUR from high remineralization rates.

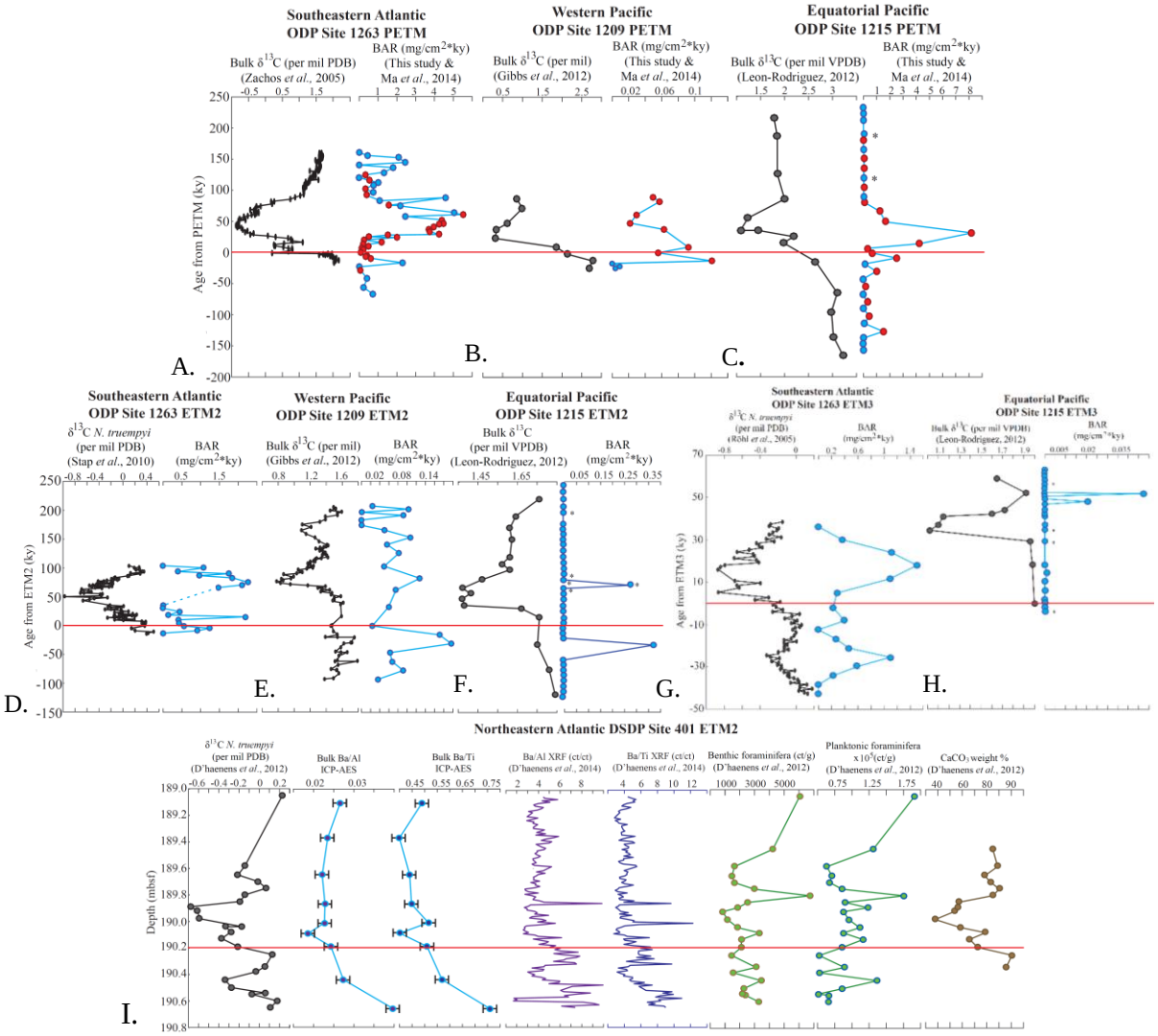

Figure 4.1: Barite accumulation rates (BAR) or Ba/Al and Ba/Ti elemental ratios at the study sites. A – C. PETM (red dots Ma et al. (2014); blue this study), D – F and I. ETM2 and G – H. ETM3. Dashed blue line indicates a sample gap and red line indicates the onset of the hyperthermal events per A and G. Röhl et al. (2007), B. Penman et al. (2014), C. Leon-Rodriguez and Dickens (2010), D. Jennions et al. (2015), E. Gibbs et al. (2012) and F. and H. E.Thomas (personal communication). I. Export production (blue lines) represented as elemental ratios of Ba/Al and Ba/Ti from bulk sediment samples and relative onset of ETM2 (red line) from D'haenens et al. (2014)

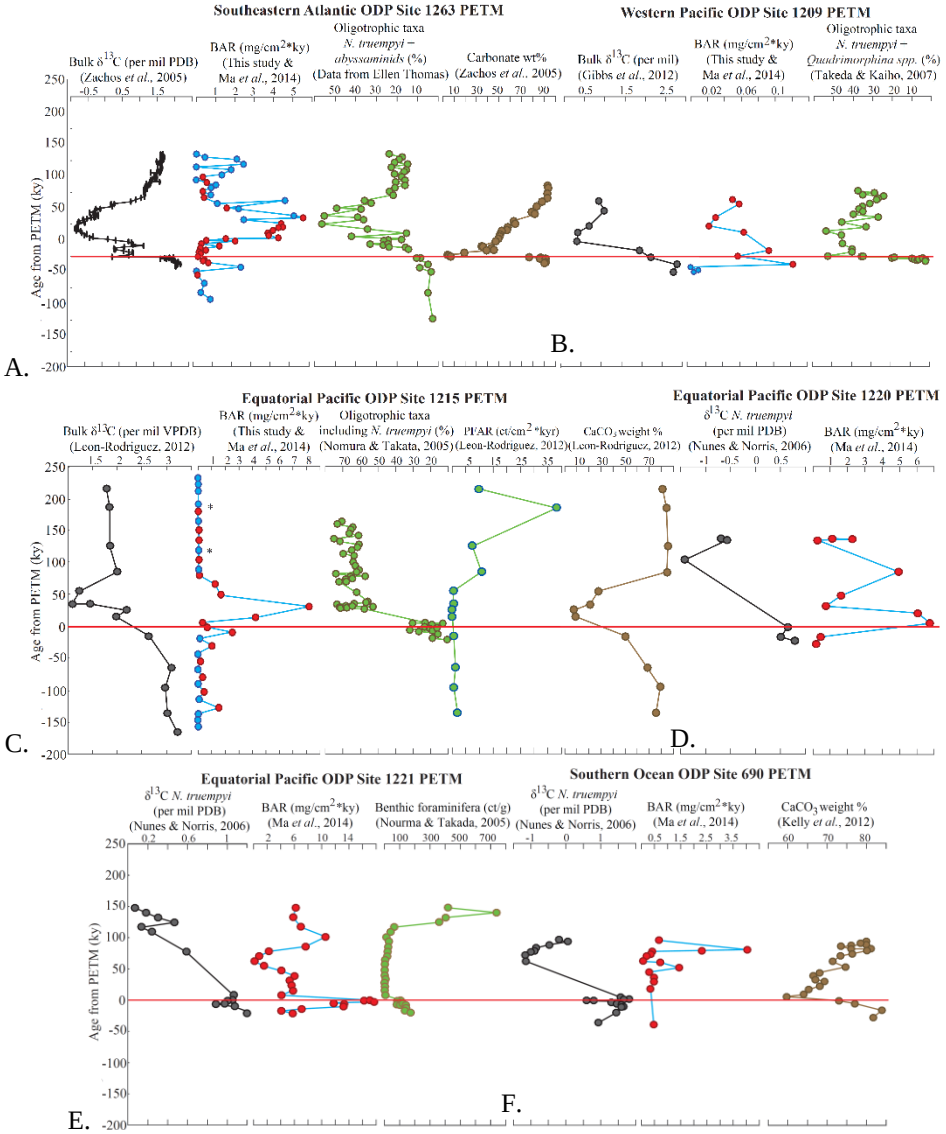

Figure 4.2: Study sites and comparison figures BAR during the PETM. Export production (blue line, red circles Ma et al. (2014) and blue circles this study, dashed blue line sample gap), productivity and calcium carbonate during the PETM (onset red line) at A. Southeastern Atlantic ODP Site 1263, B. Western Pacific Ocean ODP Site 1209, Equatorial Pacific C. ODP Site 1215, D. ODP Site 1220, E. ODP Site 1221 and Southern Ocean F. ODP Site 690. Age models used for A. Röhl et al. (2007), B. Penman et al. (2014), C. Leon-Rodriguez and Dickens (2010) D – F. Ma et al. (2014).

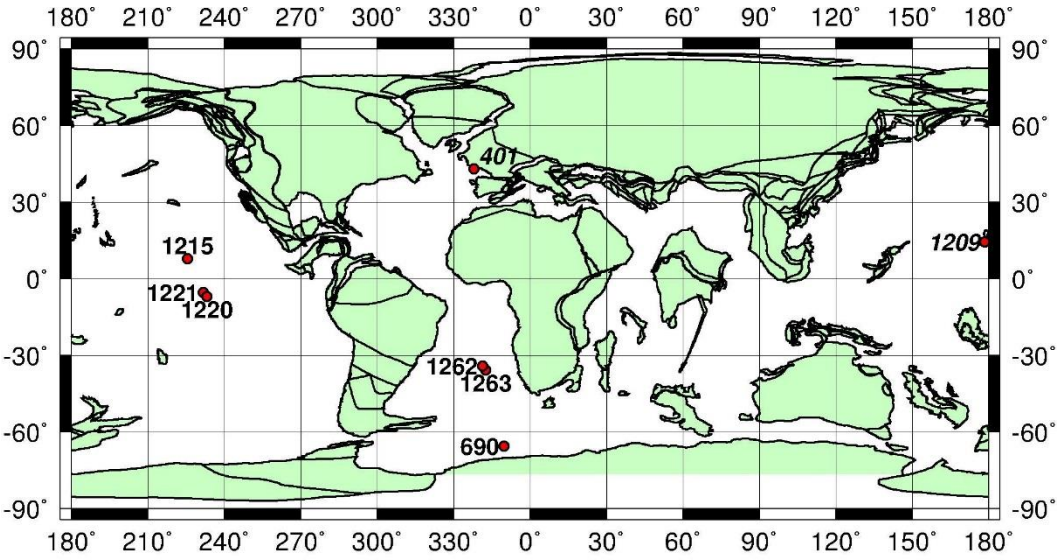

Figure 4.3: Study and comparison sites. Paleoreconstruction of 53 million years ago (Ma) with the study ODP Sites 1209, 1215, 1263 and DSDP 401 along with comparative International Ocean Drilling Program (IODP) Site U1337 and ODP Sites 690, 1220, 1221 and 1262. The modern locations for the sites are as follows: ODP Site 1209 is in the western Pacific Ocean southeast of Japan, ODP Sites 1215, 1220 and 1221 are in the equatorial Pacific Ocean near Honolulu, ODP Sites 1262 and 1263 are in the southeast Atlantic Ocean along Walvis Ridge, ODP Site 690 is on Maud Rise in the Southern Ocean and DSDP Site 401 is off the west coast of France on the North Biscay Margin. Plate reconstructions adapted from Ocean Drilling Stratigraphic Network (ODSN) Paleomap project (http://www.odsn.de/odsn/services/paleomap/paleomap.html).

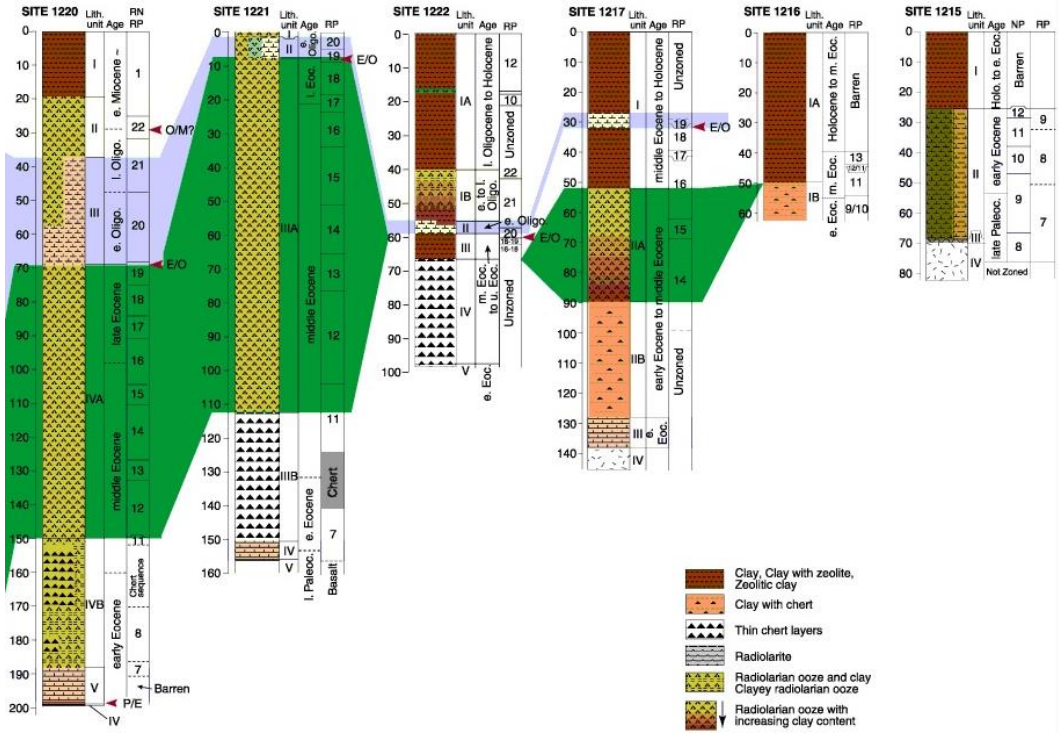

Figure 4.4: Lithologic and nannofossil comparison of Equatorial ODP Leg 199 sites. Sites presented from left to right by increasing latitude. Sample Site 1215 was obtained from the northernmost location of Leg 199 (Shipboard Scientific Party, 2002b).

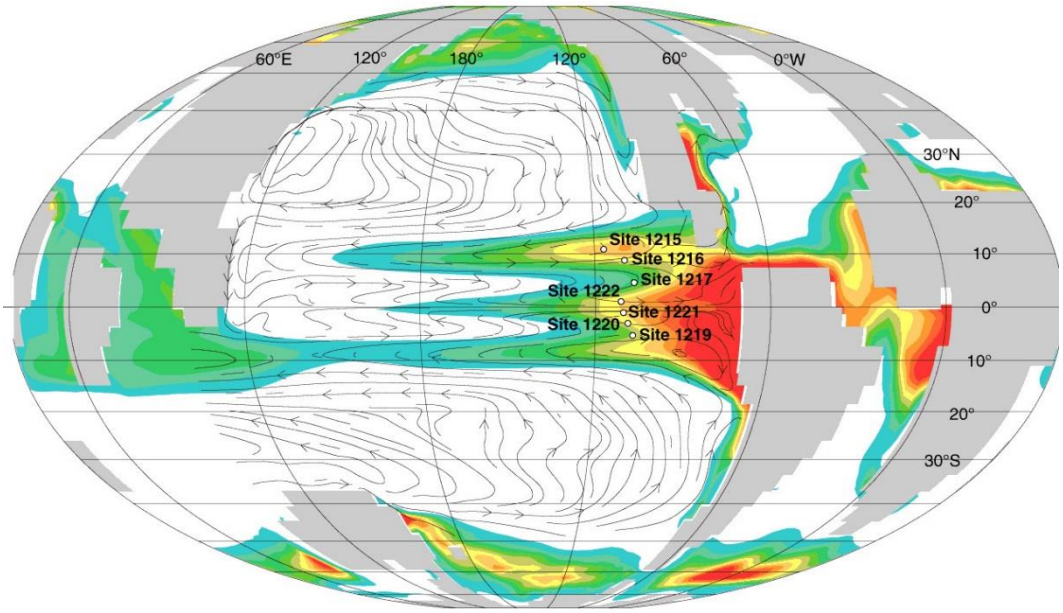

Figure 4.5: Equatorial upwelling model reconstruction for 56 Ma. Gobal land-sea distribution and annual average upwelling into the thermocline model from Huber (2002). Depicted in the model were regions of upwelling with intensities ranging from weak (blue) to strong (red), downwelling (white), and current streamlines (arrows) from approximately 100 m depth (Shipboard Scientific Party, 2002b).

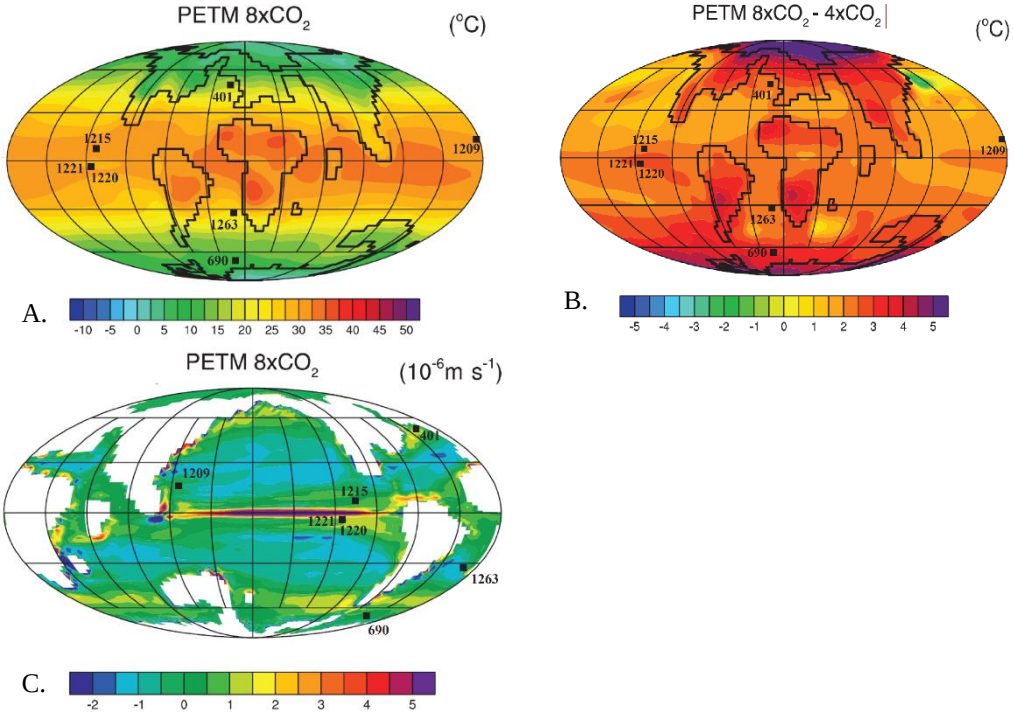

Figure 4.6: Modeled PETM global surface air temperature and upwelling regions. Surface air temperature for A. 8xCO_2 scenario 50 year mean surface air temperature (°C) and B. difference of 8xCO2 - 4xCO_2 to demonstrate regional temperature variation with increased CO_2. C. vertical velocity resulting in upwelling of nutrient rich deep ocean water represented in warmer colors (Winguth et al., 2010). Figure modified from Winguth et al. (2010).

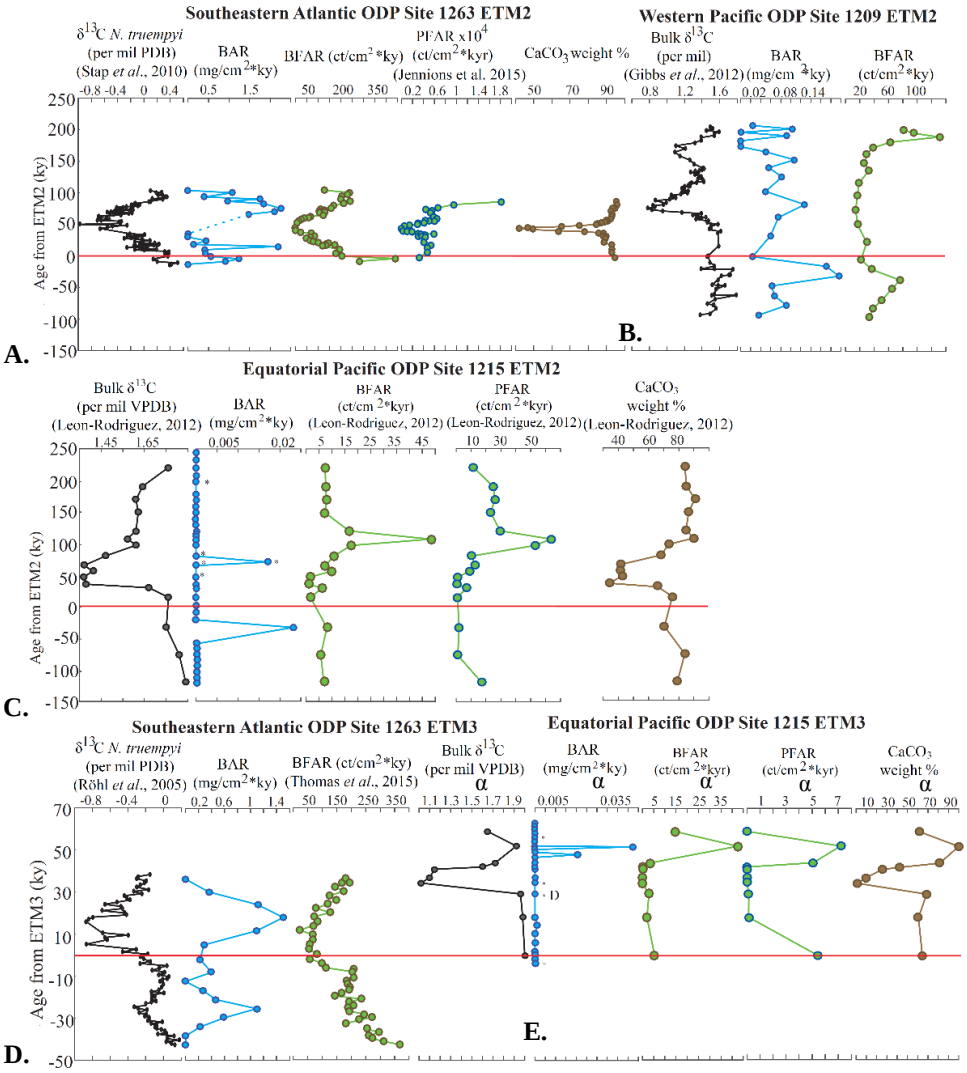

Figure 4.7: Comparison of export production, productivity and calcium during ETM2. Export production (blue lines, dashed blue line indicates sample gap) and productivity A. ODP Site 1263, B. ODP Site 1209 and C. ODP Site 1215, and ETM3 at D. ODP Site 1263, E. Site 1215. Red line indicates the onset of the hyperthermal events per A Jennions et al. (205), B and G. Röhl et al. (2007), B. Penman et al. (2014), C, E and I. Leon-Rodriguez and Dickens (2010), D. Jennions et al. (2015), and E. Gibbs et al. (2012). Additional labels include chert (*) and potential Discoaster coccolithophores (D) in residues after barite separation and α represents Leon-Rodriguez (2012).

A.

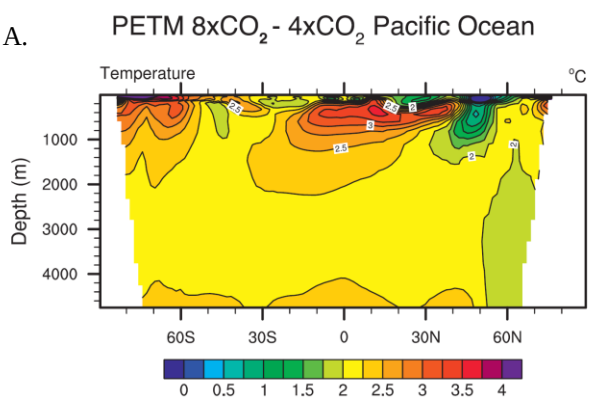

B.

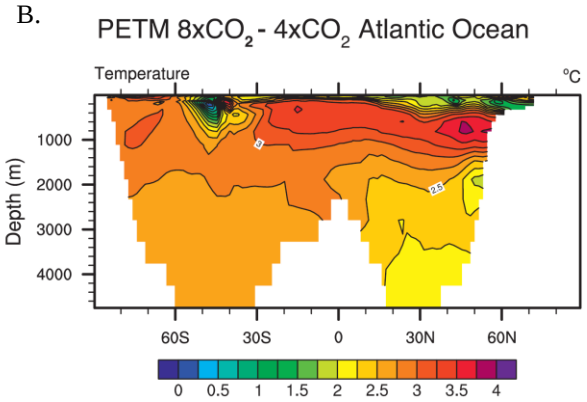

Figure 4.8: Simulated PETM potential temperatures with depth in the ocean. 50 year mean vertical temperature differences from $8xCO_2$ to $4xCO_2$ in the A. Pacific Ocean and B. Atlantic Ocean (Winguth et al., 2010).

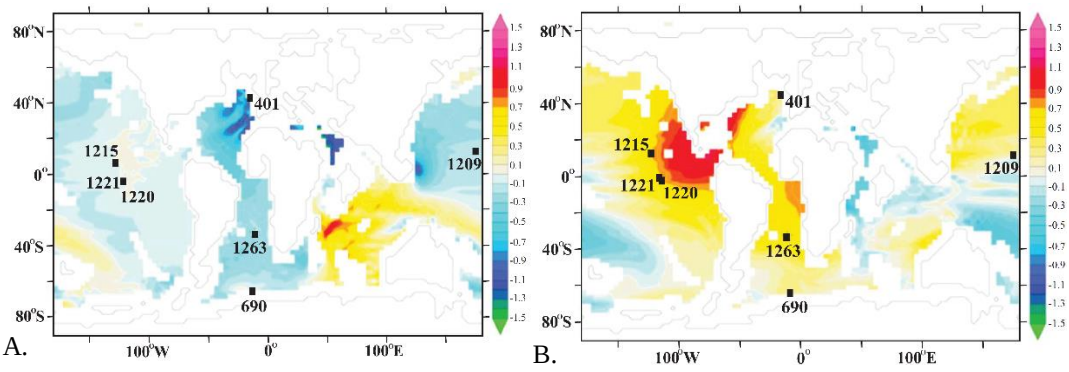

Figure 4.9: Global model of ocean temperature and circulation changes in ETM2. Global model projection of the temperature difference between the deep (~3500 m) and intermediate (~1500 m) ocean depths for A. early ETM2 (0 to 45 kyr after onset) and late ETM2 (85 to 130 kyr after onset) conditions with increased temperature difference from 1x to 2x preindustrial atmospheric CO_2 and B. mid-ETM2 (45 to 85 kyr after the onset) with 1x to 6x preindustrial atmospheric CO_2, and ocean circulation change. Modified from Jennions et al. (2015). Warm intermediate depths during ETM2 could potentially enhanced microbial metabolisms, promoting remineralization of exported organic matter (Jennions et al., 2015: Ma et al., 2014).

Table 4.1: Comparison of CIE magnitude and peak barite accumulation rate (BAR)

Event	Age [Ma]	Peak BAR [mg/cm^2*kyr]	CIE $\Delta\delta^{13}C$
ETM3*	~52.4	~1	-0.8‰
ETM2**	~53.7	~2	-1.0‰
PETM***	~55.5	~8	-3.0‰

*Site 1263, *N. truempyi* $\delta^{13}C$ (Röhl, et al., 2005); **Site 1263, *N. truempyi* $\delta^{13}C$ (Stap et al., 2010); ***Site 1215, bulk $\delta^{13}C$ (Leon-Rodriguez, 2012)

Chapter 5

Conclusions

Despite reduced or unchanged surface productivity, BAR and therefore export production, was increased at the study sites during the PETM, ETM2 and ETM3. Generally, maximum export production occurred during the hyperthermal CIE minimums for most of the sites from increased POC export efficiency out of the euphotic zone due to increased SSTs and/or increased residence time in the water column due to $CaCO_3$ dissolution of primary ballasting material. Export production was proportional to the CIE magnitude at the sites, with highest export production after the onset of the PETM and the smallest after the onset of ETM3.

After the onset of the PETM, export production was highest in the Equatorial Pacific (Sites 1215, 1220 and 1221) and the Southeastern Atlantic (Site 1263). The Southeastern Atlantic (Site 1263) had the highest export production after the onset of ETM2 and ETM3, however currently there is not a reliable record of BAR or export production from the Equatorial Pacific during these two events. Poor barite recovery from Site 1215 in the Equatorial Pacific during ETM2 and ETM3 may be the result of diagenetic alteration in the sediment due to the presence of other diagenetic byproducts such as numerous chert fragments and calcareous coccolithophores in the barite residue with potential silica replacement.

Reconstruction of remineralization rates during the early Eocene is important to explain a potential cause of the benthic foraminiferal extinctions during the PETM and low BFAR during ETM2 and ETM3, despite evidence for high export of POC during those hyperthermal events. Remineralization removes POC from the thermocline, reducing the amount of detrital organic matter that reaches the benthic foraminifera at the seafloor. Oligotrophic benthic foraminiferal taxa and low BFAR were likely the result of low DO and/or nutrients in the deep ocean. Results from this study suggest that low nutrients were due to high microbial remineralization rates from high

intermediate depth temperatures and dissolution of $CaCO_3$ ballasting material. Potential evidence of high remineralization is lower DO at intermediate ocean depths compared to the deep ocean, possibly indicating high OUR.

Future development of bulk sediment digestion Ba analysis with calibrated XRF scans that are comparable with BAR have the potential for reliable high resolution export production analysis along continental margins and regions with low barite accumulation. Future improvements of this method would involve bulk digestion of samples from existing barite records such as Sites 1220, 1221 and 690, along with XRF scans of Site 1221 and others. Direct comparison of Ba/Al and Ba/Ti elemental ratios to BAR from these sites would clarify which element ratios were more closely related to marine pelagic barite expanding on previous work by others. Disconnect between pelagic productivity and benthic foraminiferal populations during the PETM demonstrates the necessity of creating more global export production records that should include sites from continental margins for incorporation in global climate and circulation models.

Abundant peer reviewed articles currently exist on the PETM, but many sites could benefit from an extension of the analyzed core depth and age ranges before and after the PETM. The maximum BAR peak for some of the sites were prior to the onset of the hyperthermal event, such as the PETM at Site 1209 which occurred before the Ma et al. (2014) sample range. The smaller Eocene hyperthermals (ETM2 and ETM3) have only been investigated at a few sites and further research into different aspects of these hyperthermals, along with developing BAR records at a multitude of other locations, especially the Equatorial Pacific, will be required for a better and more complete comparison with the PETM. Earth system model simulations of DO concentration changes in the thermocline during the hyperthermal events could verify potential changes in respiration rates.

Appendix A

Barite data tables for Sites 1263, 1209 and 1215

Table A.1: Site 1263 ETM3 data

Exp/ Leg	Site	Hole	Core	Sect	Half	Top (cm)	Bottom (cm)	Depth (mbsf)	Depth (mcd)	Dry wt (g)	Barite (mg)	Barite (mg/g)	Age* (ky from ETM3)	LSR (cm/kyr)	DBD** (g/cm^3)	MAR (g/cm^2*kyrr)	BAR (mg/cm^2*kyrr)
208	1263	A	27H	2	A	124	125.5	234.84	274.87	22.8813	0	0.00	36.34109		1.488		0
208	1263	A	27H	2	A	130	131.5	234.90	274.93	29.7416	7.30	0.25	30.24806	0.984733	1.488	1.465282	0.359477
208	1263	A	27H	2	A	136	137.5	234.96	274.99	26.2781	19.99	0.76	24.15504	0.984733	1.488	1.465282	1.114667
208	1263	A	27H	2	A	142	143.5	235.02	275.05	28.7946	29.55	1.03	18.06202	0.984733	1.488	1.465282	1.503551
208	1263	A	27H	2	A	148	149.5	235.08	275.11	35.8277	28.79	0.80	11.73333	0.914029	1.488	1.360076	1.092988
208	1263	A	27H	3	A	4	5.5	235.14	275.17	38.0175	8.09	0.21	5.00000	0.891089	1.488	1.325941	0.282206
208	1263	A	27H	3	A	10	11.5	235.20	275.23	28.9661	4.99	0.17	-1.86667	0.877193	1.488	1.305263	0.225041
208	1263	A	27H	3	A	16	17.5	235.26	275.29	33.5936	7.47	0.22	-8.06061	1.20438	1.488	1.792117	0.398299
208	1263	A	27H	3	A	22	23.5	235.32	275.35	20.6177	0.00	0.00	-12.38788	1.386555	1.488	2.063193	0
208	1263	A	27H	3	A	28	29.5	235.38	275.41	34.4054	4.48	0.13	-16.71515	1.386555	1.488	2.063193	0.2686
208	1263	A	27H	3	A	34	35.5	235.44	275.47	34.5685	7.79	0.23	-21.04242	1.386555	1.488	2.063193	0.464764
208	1263	A	27H	3	A	40	41.5	235.50	275.53	33.0076	17.53	0.53	-25.36970	1.386555	1.488	2.063193	1.095998
208	1263	A	27H	3	A	46	48	235.56	275.59	23.075	6.68	0.29	-29.69697	1.386555	1.488	2.063193	0.597217
208	1263	A	27H	3	A	52	54	235.62	275.65	27.0822	3.00	0.11	-34.02424	1.386555	1.488	2.063193	0.228278
208	1263	A	27H	3	A	58	60	235.68	275.71	23.0552	0.00	0.00	-38.35152	1.386555	1.488	2.063193	0
208	1263	A	27H	3	A	64	66	235.74	275.77	30.8069	0.00	0.00	-42.67879	1.386555	1.488	2.063193	0

*Age model from Röhl et al. (2007), **Dry bulk density (DBD) from the IODP Initial Reports (Zachos et al. (2004)

Table A.2: Site 1263 ETM2 data

Exp/ Leg	Site	Hole	Core	Sect	Half	Top (cm)	Bottom (cm)	Depth (mbsf)	Depth (mcd)	Dry wt (g)	Barite (mg)	Barite (mg/g)	Age* (kyr from ETM2)	LSR (cm/kyr)	DBD** (g/cm^3)	MAR (g/cm^2*kyrr)	BAR (mg/cm^2*kyrr)
208	1263	C	10H	6	A	0	2	251.90	293.78	23.2955	0.00	0.00	104.21195	2.616	1.48	3.87183	0
208	1263	C	10H	6	A	10	12	252.00	293.88	40.9955	11.46	0.28	100.38947	2.616	1.48	3.87183	1.082434
208	1263	C	10H	6	A	28	30	252.18	294.06	31.6843	3.02	0.10	93.90992	2.787	1.48	4.12427	0.39324
208	1263	C	10H	6	A	38	40	252.28	294.16	31.0694	13.22	0.43	90.30273	2.772	1.48	4.10292	1.745687
208	1263	C	10H	6	A	47	49	252.37	294.25	38.8487	9.22	0.24	87.02941	2.750	1.48	4.06926	0.966022
208	1263	C	10H	6	A	58	60	252.48	294.36	30.5772	13.53	0.44	83.13034	2.829	1.48	4.18626	1.852865
208	1263	C	10H	6	A	77	79	252.67	294.55	40.1396	26.32	0.66	75.63942	2.328	1.48	3.44573	2.259473
208	1263	C	10H	6	A	86	88	252.76	294.64	32.3248	26.26	0.81	70.72204	1.743	1.48	2.57955	2.095403
208	1263	C	10H	6	A	94	96	252.84	294.72	41.9494	24.18	0.58	66.34132	1.730	1.48	2.55975	1.475759
208	1263	C	10H	7	W	13	15	253.03	294.91	26.4270	0.00	0.00	35.49972	0.858	1.48	1.27052	0
208	1263	C	10H	7	W	19	21	253.09	294.97	22.0692	0.00	0.00	30.31615	1.249	1.48	1.84894	0
208	1263	C	10H	7	A	25	27	253.15	295.03	28.0080	9.52	0.34	24.58293	0.884	1.48	1.30851	0.444538
208	1263	C	10H	7	A	31	33	253.21	295.09	26.8560	1.66	0.06	18.56505	1.544	1.48	2.28466	0.141144
208	1263	C	10H	7	A	39	41	253.29	295.17	39.4741	29.83	0.76	15.51056	1.969	1.48	2.91350	2.201321
208	1263	C	10H	7	A	49	51	253.39	295.27	28.7357	4.29	0.15	10.27050	1.908	1.48	2.82439	0.421244
208	1263	C	10H	7	A	59	61	253.49	295.37	28.8919	4.61	0.16	4.84670	1.844	1.48	2.72871	0.435723
208	1263	C	10H	7	A	70	72	253.60	295.48	30.8794	5.57	0.18	-0.42142	2.088	1.48	3.09028	0.557866
208	1263	C	10H	7	A	79	81	253.69	295.57	37.7065	13.52	0.36	-4.24675	2.353	1.48	3.48206	1.248868
208	1263	C	10H	7	A	89	91	253.79	295.67	34.8687	9.28	0.27	-8.51595	2.342	1.48	3.46669	0.922981
208	1263	C	10H	7	A	99	101	253.89	295.77	29.0460	0.00	0.00	-12.78515	2.342	1.48	3.46669	0

*Age model from Jennions et al (2015), **Dry bulk density (DBD) from the IODP Initial Reports (Zachos et al. (2004)

Table A.3: Site 1263 PETM data

Site	Hole	Core	Sect	Half	Top (cm)	Bottom (cm)	Depth (mbsf)	Depth (mcd)	Depth (rmcd)	Dry wt (g)	Barite (mg)	Barite (mg/g)	Barite Ma *et al*. (2014) (mg/g)	Age* (ky from PETM)	LSR (cm/kyr)	DBD** (g/cm^3)	MAR (g/cm^2*kyrr)	BAR (mg/cm^2*kyrr)
1263	C	14H	1	A	13	15	282.53	332.84	332.46	15.7354	0.00	0.00		160.186567		1.403		0.000
1263	C	14H	1	A	28	30	282.68	332.99	332.61	25.5234	2.69	0.11		155.485075	3.190	1.403	4.476	0.472
1263	C	14H	1	A	40	42	282.80	333.11	332.73	35.6200	17.10	0.48		151.723881	3.190	1.403	4.476	2.149
1263	C	14H	1	A	64	67	283.04	333.35	332.95	47.3136	28.76	0.61		144.272727	2.881	1.403	4.041	2.457
1263	C	14H	1	A	76	78	283.16	333.47	333.07	35.7480	0.09	0.00		140.107438	2.881	1.403	4.041	0.011
1263	C	14H	1	A	88	90	283.28	333.59	333.19	34.0753	15.88	0.47		135.942149	2.881	1.403	4.041	1.883
1263	C	14H	1	A	109	111	283.49	333.80	333.40	35.2633	11.58	0.33		128.571429	2.826	1.403	3.964	1.302
1263	C	14H	1		118	120	283.58	333.89	333.49				0.107	124.714286	2.333	1.403	3.273	0.351
1263	C	14H	1	A	130	132	283.70	334.01	333.61	34.5561	0.00	0.00		119.571429	2.333	1.403	3.273	0.000
1263	C	14	1		140	142	283.80	334.11	333.71				0.172	115.285714	2.333	1.389	3.240	0.559
1263	C	14H	1	A	148	150	283.88	334.19	333.79	27.1761	8.55	0.31		111.857143	2.333	1.389	3.240	1.019
1263	C	14H	2	A	8	10	283.98	334.29	333.89	18.1600	3.98	0.22		107.490506	2.290	1.389	3.180	0.697
1263	C	14	2		20	22	284.10	334.41	334.01				0.121	101.376582	1.799	1.522	2.739	0.331
1263	C	14H	2	A	30	32	284.20	334.51	334.11	26.8975	7.08	0.26		96.281645	1.963	1.522	2.988	0.786
1263	C	14	2		38	40	284.28	334.59	334.19				0.125	92.205696	1.963	1.578	3.096	0.386
1263	A	33H	2	W	108	111	283.68	334.68	334.28	38.9748	61.10	1.57		87.620253	1.963	1.578	3.096	4.854
1263	D	3H	CC	W	0	2	284.01	334.62	334.35	30.0411	19.56	0.65		82.566667	1.385	1.578	2.185	1.423
1263	C	14	2		62	64	284.52	334.83	334.43				0.737	76.433335	1.304	1.652	2.154	1.587
1263	B	28X	CC	W	0	2	283.88	334.71	334.46	23.6605	28.46	1.20		74.133335	1.304	1.718	2.240	2.695
1263	A	33H	CC	W	9	10.5	283.99	334.99	334.59	33.3497	93.08	2.79		64.000003	1.274	1.718	2.188	6.106
1263	C	14	2		82	84	284.72	335.03	334.63				2.695	60.654548	1.196	1.718	2.054	5.536
1263	C	14H	2	A	85	87	284.75	335.06	334.67	31.2902	35.48	1.13		57.309093	1.196	1.784	2.133	2.418
1263	D	4	1		15	17	284.45	335.08	334.75				2.053	50.618182	1.196	1.784	2.133	4.379

Table A.3-*Continued*

1263	D	4	1		20	22	284.50	335.13	334.80				2.140	46.436363	1.196	1.746	2.088	4.467
1263	D	4	1		21	23	284.51	335.14	334.81				1.997	45.599999	1.196	1.779	2.127	4.249
1263	D	4	1		27	29	284.57	335.20	334.87				2.154	39.974927	1.051	1.749	1.839	3.960
1263	D	4	1		30.5	32.5	284.61	335.23	334.91				2.076	36.169935	1.051	1.696	1.783	3.701
1263	D	4	1		34	36	284.64	335.27	334.94				2.132	33.316191	1.051	1.669	1.754	3.740
1263	D	4	1		39	41	284.69	335.32	334.99				2.407	28.559950	1.051	1.670	1.756	4.227
1263	D	4	1		40	42	284.70	335.33	335.00				0.876	27.608702	1.051	1.639	1.723	1.509
1263	C	14	2		122	124	285.12	335.43	335.03				0.287	24.754958	1.051	1.741	1.831	0.525
1263	D	4	1		44	46	284.74	335.37	335.04				1.221	23.758874	1.004	1.631	1.637	1.999
1263	D	4	1		48	50	284.78	335.41	335.08				0.158	19.686046	0.975	1.618	1.578	0.249
1263	D	4	1		52	54	284.82	335.45	335.12				0.767	15.583720	0.975	1.579	1.540	1.181
1263	D	4	1		56	58	284.86	335.49	335.16				0.117	11.481394	0.975	1.634	1.593	0.186
1263	C	14	2		137	139	285.27	335.58	335.18				0.283	9.430231	0.975	1.707	1.664	0.470
1263	D	4	1		60	62	284.90	335.53	335.20				0.086	7.379069	0.975	1.568	1.529	0.131
1263	C	14	2		142	144	285.32	335.63	335.23				0.141	4.302324	0.975	1.589	1.549	0.218
1263	C	14	2		147	149	285.37	335.68	335.28				0.045	-0.486486	1.118	1.570	1.754	0.079
1263	C	14	CC		8	10	285.48	335.79	335.39				0.269	-5.837838	2.056	0.742	1.525	0.410
1263	D	4	1		80	82	285.10	335.73	335.40				0.143	-6.324324	2.056	1.206	2.479	0.354
1263	C	14	CC		16	18	285.56	335.87	335.47				0.202	-9.729730	2.056	1.463	3.007	0.608
1263	C	15H	CC	A	11	13	285.71	336.02	335.62	22.1484	23.17	1.05		-17.027027	2.056	1.463	3.007	3.145
1263	A	34X	1	W	76	78	284.86	336.10	335.72	27.4024	0.00	0.00		-23.508197	1.452	0.304	0.442	0.000
1263	D	4	2		20	22	285.50	336.13	335.80				0.115	-29.016393	1.452	0.304	0.442	0.051
1263	A	34X	1	W	104	106	285.14	336.38	336.00	24.4888	4.93	0.20		-42.786885	1.452	0.304	0.442	0.089
1263	A	34X	1	W	124	126	285.34	336.58	336.20	16.6086	1.90	0.11		-56.557377	1.452	0.304	0.442	0.050
1263	A	34X	1	W	140	142	285.50	336.74	336.36	27.5424	9.83	0.36		-67.573770	1.452	0.304	0.442	0.158

*Age model from Röhl et al. (2007), **Dry bulk density (DBD) calculated from calibration of gamma ray density and dry density from discrete (Moisture And Density or MAD) samples measured on the JOIDES Resolution and both are archived on the IODP Janus database

Table A.4: Site 1209 Post-ETM2 data

Exp/ Leg	Site	Hole	Core	Sect	Half	Top (cm)	Bottom (cm)	Depth (mbsf)	Depth (mcd)	Depth* (rmcd)	Dry wt (g)	Barite (mg)	Barite (mg/g)	Age** (kyr from ETM2)	LSR (cm/kyr)	DBD*** (g/cm^3)	MAR (g/cm^2*kyrr)	BAR (mg/cm^2*kyrr)
198	1209	C	10H	4	W	115	117	189.15	204.44	209.16	20.7726	8.50	0.41	678.00	1.894	0.98	1.86	0.76
198	1209	C	10H	4	W	125	127	189.25	204.54	209.26	22.5050	6.54	0.29	663.00	0.667	0.98	0.66	0.19
198	1209	C	10H	4	W	135	137	189.35	204.64	209.36	19.1593	0	0.00	648.00	0.667	0.99	0.66	0.00
198	1209	C	10H	4	W	145	147	189.45	204.74	209.46	22.1564	3.69	0.17	633.00	0.667	0.99	0.66	0.11
198	1209	C	10H	5	W	5	7	189.55	204.84	209.56	17.7923	0	0.00	618.00	0.667	0.99	0.66	0.00
198	1209	C	10H	5	W	16	18	189.66	204.95	209.67	21.3408	1.74	0.08	601.00	0.647	0.99	0.64	0.05
198	1209	C	10H	5	W	26	28	189.76	205.05	209.77	19.0655	0.0	0.00	586.00	0.667	0.99	0.66	0.00
198	1209	C	10H	5	W	38	40	189.88	205.17	209.89	24.6893	2.79	0.11	568.00	0.667	0.99	0.66	0.07
198	1209	C	10H	5	W	46	48	189.96	205.25	209.97	19.2973	0	0.00	556.00	0.667	0.99	0.66	0.00
198	1209	C	10H	5	W	57	59	190.07	205.36	210.08	21.5335	0.64	0.03	539.00	0.647	0.97	0.63	0.02
198	1209	C	10H	5	W	67	69	190.17	205.46	210.18	21.3177	0	0.00	522.00	0.588	0.94	0.55	0.00
198	1209	C	10H	5	W	75	77	190.25	205.54	210.26	16.5146	0	0.00	506.00	0.500	0.91	0.46	0.00
198	1209	C	10H	5	W	86	88	190.36	205.65	210.37	19.4534	0	0.00	490.00	0.688	0.88	0.60	0.00
198	1209	C	10H	5	W	96	98	190.46	205.75	210.47	19.5807	0	0.00	464.00	0.385	0.86	0.33	0.00
198	1209	C	10H	5	W	106	108	190.56	205.85	210.57	23.1606	0	0.00	444.00	0.500	0.82	0.41	0.00
198	1209	C	10H	5	W	116	118	190.66	205.95	210.67	17.2904	0	0.00	424.00	0.500	0.78	0.39	0.00
198	1209	C	10H	5	W	126	128	190.76	206.05	210.77	20.5313	0	0.00	404.00	0.500	0.78	0.39	0.00
198	1209	C	10H	5	W	135	137	190.85	206.14	210.86	20.8816	3.27	0.16	371.00	0.273	0.79	0.21	0.03
198	1209	C	10H	5	W	145	147	190.95	206.24	210.96	21.4329	0	0.00	330.00	0.244	0.79	0.19	0.00
198	1209	C	10H	6	W	5	7	191.05	206.34	211.06	24.7809	6.09	0.25	289.00	0.244	0.18	0.04	0.01
198	1209	C	10H	6	W	15	17	191.15	206.44	211.16	23.3590	5.10	0.22	248.00	0.244	1.25	0.30	0.07

*Revised meters composite depth (rmcd) offset from Westerhold and Röhl (2006) **Age model from Gibbs et al. (2012), ***Dry bulk density (DBD) calculated from calcium carbonate weight percent (Hancock et al., 2005) calibrated with the high biogenic carbonate weight percent equation from Snoeckx and Rea (1994).

Table A.5 Site 1209 ETM2 data

Exp / Leg	Site	Hole	Core		Half	Top (cm)	Bottom (cm)	Depth (mbsf)	Depth (mcd)	Depth* (rmcd)	Dry wt (g)	Barite (mg)	Barite (mg/g)	Age** (kyr from ETM2)	LSR (cm/kyr)	DBD*** (g/cm^3)	MAR (g/cm^2*kyrr)	BAR (mg/cm^2*kyrr)
198	1209	C	10H	6	W	25	27	191.25	206.54	211.26	21.3282	2.69	0.13	207.05	1.894	0.81	1.54	0.19
198	1209	C	10H	6	W	35	37	191.35	206.64	211.36	22.5662	1.50	0.07	201.77	1.894	0.82	1.55	0.10
198	1209	C	10H	6	W	45	47	191.45	206.74	211.46	18.0823	0	0.00	196.41	1.865	0.82	1.54	0.00
198	1209	C	10H	6	W	55	57	191.55	206.84	211.56	20.3763	1.21	0.06	191.00	1.848	0.83	1.53	0.09
198	1209	C	10H	6	W	65	67	191.65	206.94	211.66	15.4692	0	0.00	182.98	1.247	0.84	1.04	0.00
198	1209	C	10H	6	W	75	77	191.75	207.04	211.76	18.8638	0	0.00	173.75	1.084	0.84	0.91	0.00
198	1209	C	10H	6	W	85	87	191.85	207.14	211.86	17.8632	0	0.00	164.53				
198	1209	C	10H	6	W	95	97	191.95	207.24	211.96	16.0248	0	0.00	152.95				
198	1209	A	21H	3	W	5	7	191.75	204.96	211.85	23.4502	1.59	0.07	165.45	0.880	0.85	0.75	0.05
198	1209	A	21H	3	W	15	17	191.85	205.06	211.95	17.4198	2.74	0.16	152.95	0.800	0.85	0.68	0.11
198	1209	A	21H	3	W	25	27	191.95	205.16	212.05	18.9671	1.49	0.08	140.49	0.803	0.89	0.71	0.06
198	1209	A	21H	3	W	35	37	192.05	205.26	212.15	19.8687	2.59	0.13	125.95	0.688	0.92	0.63	0.08
198	1209	A	21H	3	W	45	47	192.15	205.36	212.25	21.2052	2.54	0.12	102.99	0.435	0.95	0.42	0.05
198	1209	A	21H	3	W	55	57	192.25	205.46	212.35	20.1645	5.46	0.27	82.11	0.479	0.99	0.47	0.13
198	1209	A	21H	3	W	65	67	192.35	205.56	212.45	18.3160	2.81	0.15	61.68	0.490	1.00	0.49	0.08
198	1209	A	21H	3	W	75	77	192.45	205.66	212.55	20.3201	5.05	0.25	32.49	1.00	0.24	0.06	1.00
198	1209	A	21H	3	W	85	87	192.55	205.76	212.65	17.6101	1.39	0.08	-0.30	0.99	0.30	0.02	0.99
198	1209	A	21H	3	W	95	97	192.65	205.86	212.75	17.7267	4.74	0.27	-15.71	0.98	0.64	0.17	0.98
198	1209	A	21H	3	W	105	107	192.75	205.96	212.85	18.8799	5.86	0.31	-31.13	0.98	0.63	0.20	0.98
198	1209	A	21H	3	W	115	117	192.85	206.06	212.95	17.5474	1.74	0.10	-46.54	0.97	0.63	0.06	0.97
198	1209	A	21H	3	W	125	127	192.95	206.16	213.05	15.2911	1.64	0.11	-61.95	0.96	0.62	0.07	0.96
198	1209	A	21H	3	W	135	137	193.05	206.26	213.15	21.1829	3.12	0.15	-77.37	0.96	0.62	0.09	0.96
198	1209	A	21H	3	W	145	147	193.15	206.36	213.25	16.1320	0.94	0.06	-92.78	0.95	0.62	0.04	0.95

*Revised meters composite depth (rmcd) offset from Westerhold and Röhl (2006) **Age model from Gibbs et al. (2012), ***Dry bulk density (DBD) calculated from calcium carbonate weight percent (Hancock et al., 2005) calibrated with the high biogenic carbonate weight percent equation from Snoeckx and Rea (1994).

Table A.6 Site 1209 PETM data

Exp/ Leg	Site	Hole	Core	Sect	Half	Top (cm)	Bottom (cm)	Depth (mbsf)	Depth (mcd)	Depth* (rmcd)	Dry wt (g)	Barite (mg)	Barite (mg/g)	Mat *et al*. (2012) (mg/g)	Age** (kyr from PETM)	LSR (cm/kyr)	DBD*** (g/cm^3)	MAR (g/cm^2*kyrr)	BAR (mg/cm^2*kyrr)
198	1209	A	21	7	10	12	197.80	197.80	211.01	217.81				0.163	89.00	0.354	0.85	0.30	0.05
198	1209	A	21	7	13	15	197.83	197.83	211.04	217.84				0.195	82.00	0.354	0.84	0.30	0.06
198	1209	A	21	7	19	21	197.89	197.89	211.10	217.88				0.158	61.00	0.236	0.80	0.19	0.03
198	1209	A	21	7	21	23	197.91	197.91	211.12	217.90				0.209	47.50	0.122	0.86	0.10	0.02
198	1209	A	21	7	23	25	197.93	197.93	211.14	217.92				0.421	37.33	0.162	0.92	0.15	0.06
198	1209	A	21	7	28	30	197.98	197.98	211.19	217.96				0.595	9.00	0.146	1.07	0.16	0.09
198	1209	A	21	7	30	32	198.00	198.00	211.21	217.98				0.277	0.00	0.175	1.09	0.20	0.06
198	1209	A	21	7	35	37	198.05	198.05	211.26	218.05				0.194	-13.00	1.328	1.09	0.62	0.12
198	1209	A	21 H	7	W	37	39	198.07		218.07	13.6085	0.00	0.00		-17.00	1.000	1.08	0.54	0.00
198	1209	A	21 H	7	W	39	41	198.09		218.09	17.0174	0.29	0.02		-21.00	0.750	1.08	0.54	0.01
198	1209	A	21 H	7	W	41	43	198.11		218.11	13.0968	0.09	0.01		-25.00	0.750	1.07	0.54	0.00

*Revised meters composite depth (rmcd) offset from Westerhold and Röhl (2006) **Age model from Penman et al. (2014), ***Dry bulk density (DBD) calculated from calcium carbonate weight percent (Hancock et al., 2005) calibrated with the high biogenic carbonate weight percent equation from Snoeckx and Rea (1994).

Table A.7 Site 1215 ETM3 data

Exp / Leg	Site	Hole	Core		Half	Top (cm)	Bottom (cm)	Depth (mbsf)	Dry wt (g)	Barite (mg)	Barite (mg/g)	Age** (kyr from ETM2)	LSR (cm/kyr)	DBD*** (g/cm^3)	MAR (g/cm^2*kyrr)	BAR (mg/cm^2*kyrr)
199	1215	A	4 H	5	W	145	147	27.65	8.6370	8.0923	0.000	62.7	3.83	0.429	1.64	0.000
199	1215	A	4 H	5	W	148	150	27.68	9.3701	7.8649	0.000	61.9	3.83	0.418	1.60	0.000
199	1215	A	4 H	6	W	4	6	27.74	4.5863	8.0414	0.000	60.3	3.83	0.397	1.52	0.000
199	1215	A	4 H	6	W	9	11	27.79	5.7853	8.1214	0.000	59.0	3.83	0.392	1.50	0.000
199	1215	A	4 H	6	W	15.5	17.5	27.86	7.3876	7.8976	0.000	57.3	3.79	0.498	1.88	0.000
199	1215	A	4 H	6	W	20.5	22.5	27.91	4.7834*	8.1037	0.000	56.0	3.79	0.419	1.58	0.000
199	1215	A	4 H	6	W	25.5	27.5	27.96	8.7676	8.0078	0.000	54.6	3.79	0.513	1.94	0.000
199	1215	A	4 H	6	W	30.5	32.5	28.01	9.7143	7.9271	0.000	53.3	3.79	0.562	2.13	0.000
199	1215	A	4 H	6	W	35.5	37.5	28.06	8.2238	7.8364	0.000	52.0	3.79	0.595	2.25	0.000
199	1215	A	4 H	6	W	37.5	39.5	28.08	9.3116	7.8334	0.0233	51.5	4.00	0.510	2.04	0.047
199	1215	A	4 H	6	W	42.5	44.5	28.13	6.7229	7.9044	0.000	50.3	4.00	0.432	1.73	0.000
199	1215	A	4 H	6	W	47.5	49.5	28.18	6.0251	8.1192	0.000	49.0	4.00	0.484	1.93	0.000
199	1215	A	4 H	6	W	52.5	54.5	28.23	7.4719	8.0123	0.010	47.8	4.00	0.500	2.00	0.021
199	1215	A	4 H	6	W	57.5	59.5	28.28	7.8175	8.0963	0.000	46.5	4.00	0.527	2.11	0.000
199	1215	A	4 H	6	W	62.5	64.5	28.33	8.8402	8.1194	0.000	45.3	4.00	0.552	2.21	0.000
199	1215	A	4 H	6	W	67.5	69.5	28.38	7.1028	8.0310	0.000	44.0	4.00	0.563	2.25	0.000
199	1215	A	4 H	6	W	72	74	28.42	3.8626	7.8509	0.000	42.0	2.25	0.436	0.98	0.000
199	1215	A	4 H	6	W	77.5	79.5	28.48	7.0573	7.9034	0.000	41.0	5.50	0.406	2.23	0.000
199	1215	A	4 H	6	W	85.5	87.5	28.56	3.5371	7.9200	0.000	37.0	2.00	0.383	0.77	0.000
199	1215	A	4 H	6	W	90.5	92.5	28.61	3.820*	0.000	0.000	34.4	0.80	0.360	0.29	0.000
199	1215	A	4 H	6	W	94.5	96.5	28.65	10.252*	0.00	0.00	29.2	0.62	0.546	0.34	0.000
199	1215	A	4 H	6	W	101.5	103.5	28.72	7.471	0.000	0.000	18.0	0.62	0.634	0.40	0.000
199	1215	A	4 H	6	W	106.5	108.5	28.77	9.770	0.013	0.0013	14.0	1.25	0.635	0.79	0.001
199	1215	A	4 H	6	W	111.5	113.5	28.82	10.820	0.000	0.000	10.0	1.25	0.580	0.72	0.000

Table A.7-*Continued*

199	1215	A	4 H	6	W	116.5	118.5	28.87	11.354	0.000	0.000	6.0	1.25	0.579	0.72	0.000
199	1215	A	4 H	6	W	121.5	123.5	28.92	9.824	0.000	0.000	2.0	1.25	0.539	0.67	0.000
199	1215	A	4 H	6	W	124.5	126.5	28.95	8.166	0.000	0.000	-0.2	2.50	0.522	1.31	0.000
199	1215	A	4 H	6	W	129.5	131.5	29.00	8.304	0.000	0.000	-2.2	2.50	0.516	1.29	0.000
199	1215	A	4 H	6	W	134.5	136.5	29.05	17.279*	0.000	0.000	-4.2	2.50	1.079	2.70	0.000

*Significant amount of chert in bulk sample, **Age model from E.Thomas (this study) through CIE correlation of Leon-Rodriguez and Dickens (2010) $\delta^{13}C$ and Lauretano et al. (2015), ***Dry bulk density (DBD) calculated from calcium carbonate weight percent (Hancock et al., 2005) calibrated with the high biogenic carbonate weight percent equation from Snoeckx and Rea (1994).

Table A.8 Site 1215 ETM2 data

Exp / Leg	Site	Hole	Core		Half	Top (cm)	Bottom (cm)	Depth (mbsf)	Dry wt (g)	Barite (mg)	Barite (mg/g)	Age** (kyr from ETM2)	LSR (cm/kyr)	DBD*** (g/cm^3)	MAR (g/cm^2*kyrr)	BAR (mg/cm^2*kyrr)
199	1215	A	5 H	2	W	83	85	32.03	10.398	0.000	0.000	244.0	0.88	0.561	0.49	0.000
199	1215	A	5 H	2	W	93	95	32.13	9.981	0.000	0.000	233.0	0.91	0.564	0.51	0.000
199	1215	A	5 H	2	W	103.5	105.5	32.24	9.855	0.000	0.000	220.0	0.81	0.628	0.51	0.000
199	1215	A	5 H	2	W	119	121	32.39	9.666	0.000	0.000	207.0	1.19	0.570	0.68	0.000
199	1215	A	5 H	2	W	129	131	32.49	12.351*	0.000	0.000	199.0	1.25	0.564	0.71	0.000
199	1215	A	5 H	3	W	2	4	32.72	11.244	0.000	0.000	244.0	0.88	0.561	0.49	0.000
199	1215	A	5 H	3	W	10.5	12.5	32.81	8.388	0.000	0.000	169.0	0.50	0.588	0.29	0.000
199	1215	A	5 H	3	W	26	28	32.96	11.432	0.000	0.000	158.0	1.41	0.722	1.02	0.000
199	1215	A	5 H	3	W	36.5	38.5	33.07	8.905	0.000	0.000	149.0	0.50	0.703	0.35	0.000
199	1215	A	5 H	3	W	47	49	33.17	8.110	0.000	0.000	140.0	1.17	0.687	0.80	0.000
199	1215	A	5 H	3	W	57	59	33.27	10.075	0.000	0.000	130.0	1.00	0.682	0.68	0.000
199	1215	A	5 H	3	W	67.5	69.5	33.38	9.444	0.000	0.000	120.0	1.05	0.653	0.69	0.000
199	1215	A	5 H	3	W	76	78	33.46	8.554	0.000	0.000	117.1	2.96	0.689	2.04	0.000
199	1215	A	5 H	3	W	86	88	33.56	8.542	0.000	0.000	113.8	2.96	0.680	2.01	0.000
199	1215	A	5 H	3	W	96	98	33.66	10.722	0.000	0.000	110.4	2.96	0.684	2.03	0.000
199	1215	A	5 H	3	W	106	108	33.76	8.859	0.000	0.000	107.0	2.96	0.674	2.00	0.000
199	1215	A	5 H	3	W	120	122	33.90	9.748*	0.000	0.000	97.0	1.40	0.731	1.02	0.000
199	1215	A	5 H	3	W	130.5	132.5	34.01	8.509*	0.000	0.000	80.1	1.10	0.612	0.67	0.000
199	1215	A	5 H	3	W	141	143	34.11	7.557*	0.253	0.033	70.6	1.10	0.466	0.51	0.017
199	1215	A	5 H	4	W	2	4	34.22	7.095*	0.000	0.000	65.0	1.96	0.404	0.79	0.000
199	1215	A	5 H	4	W	11.5	13.5	34.32	5.481	0.000	0.000	47.0	0.53	0.484	0.26	0.000
199	1215	A	5 H	4	W	17.5	19.5	34.38	5.567	0.000	0.000	35.4	0.52	0.455	0.24	0.000
199	1215	A	5 H	4	W	28	30	34.48	6.390	0.000	0.000	29.8	1.87	0.595	1.12	0.000

Table A.8-*Continued*

199	1215	A	5 H	4	W	40.5	42.5	34.61	7.694	0.000	0.000	14.4	0.86	0.598	0.52	0.000
199	1215	A	5 H	4	W	51	53	34.71	7.880	0.000	0.000	2.3	0.86	0.600	0.52	0.000
199	1215	A	5 H	4	W	61	63	34.81	9.920	0.000	0.000	-9.3	0.86	0.645	0.56	0.000
199	1215	A	5 H	4	W	71	73	34.91	7.982	0.000	0.000	-20.9	0.86	0.551	0.48	0.000
199	1215	A	5 H	4	W	81.5	83.5	35.02	6.566	0.368	0.056	-33.0	0.86	0.478	0.41	0.023
199	1215	A	5 H	4	W	91	93	35.11	8.804	0.000	0.000	-59.0	0.37	0.524	0.19	0.000
199	1215	A	5 H	4	W	101	103	35.21	9.838	0.000	0.000	-67.6	1.16	0.616	0.72	0.000
199	1215	A	5 H	4	W	111	113	35.31	8.139	0.000	0.000	-76.7	1.11	0.617	0.68	0.000
199	1215	A	5 H	4	W	121	123	35.41	10.564	0.000	0.000	-87.4	0.93	0.986	0.91	0.000
199	1215	A	5 H	4	W	131	133	35.51	10.512	0.000	0.000	-96.9	1.06	0.658	0.70	0.000
199	1215	A	5 H	4	W	141	143	35.61	6.133	0.000	0.000	-103.0	1.62	0.441	0.71	0.000
199	1215	A	5 H	4	W	148	150	35.68	9.475	0.000	0.000	-107.4	1.62	0.699	1.13	0.000
199	1215	A	5 H	5	W	8	10	35.78	9.763	0.000	0.000	-113.6	1.62	0.611	0.99	0.000

*Significant amount of chert in bulk sample, **Age model from E.Thomas (this study) through CIE correlation of Leon-Rodriguez and Dickens (2010) $\delta^{13}C$ and Lauretano et al. (2015), ***Dry bulk density (DBD) calculated from calcium carbonate weight percent (Hancock et al., 2005) calibrated with the high biogenic carbonate weight percent equation from Snoeckx and Rea (1994).

Table A.9 Site 1215 PETM data

Exp/ Leg	Site	Hole	Core	Sect	Half	Top (cm)	Bottom (cm)	Depth (mbsf)	Dry wt (g)	Barite (mg)	Barite (mg/g)	Mat *et al.* (2012) (mg/g)	Age* (kyr from PETM)	LSR (cm/kyr)	DBD** (g/cm^3)	MAR (g/cm^2*kyrr)	BAR (mg/cm^2*kyrr)
199	1215	A	8 H	2	W	100	102	52.70	12.287	0.000	0.000		222.0	-4.92	0.829	-4.08	0.000
199	1215	A	8 H	2	W	110	112	52.80	11.021	0.000	0.000		211.0	1.00	0.734	0.73	0.000
199	1215	A	8 H	2	W	120	122	52.90	11.577	0.000	0.000		231.0	-0.50	0.756	-0.38	0.000
199	1215	A	8 H	2	W	130	132	53.00	14.258*	0.203	0.014		191.0	0.25	1.007	0.25	0.004
199	1215	A	8	2		140	142	53.10				0.096	179.0	0.67	0.737	0.49	0.047
199	1215	A	8 H	3	W	0	2	53.20	12.991	0.000	0.000		164.0	0.67	0.724	0.48	0.000
199	1215	A	8	3		10	12	53.30				0.083	149.0	0.67	0.779	0.52	0.043
199	1215	A	8	3		20	22	53.40				0.096	134.0	0.67	0.697	0.46	0.045
199	1215	A	8 H	3	W	30	32	53.50	13.503*	0.000	0.000		118.8	0.64	0.768	0.49	0.000
199	1215	A	8	3		40	42	53.60				0.071	103.5	0.66	0.876	0.57	0.041
199	1215	A	8 H	3	W	50	52	53.70	10.438	0.000	0.000		88.1	0.65	0.675	0.44	0.000
199	1215	A	8	3		60	62	53.80				0.126	79.3	1.40	0.550	0.77	0.098
199	1215	A	8	3		80	82	54.00				3.057	65.0	1.43	0.288	0.41	1.259
199	1215	A	8	3		100	102	54.20				4.433	48.3	0.89	0.417	0.37	1.652
199	1215	A	8	3		120	122	54.40				8.186	30.8	1.90	0.527	1.00	8.222
199	1215	A	8	3		140	142	54.60				12.454	13.5	1.33	0.257	0.34	4.266
199	1215	A	8	4		0	2	54.70				0.951	6.0	1.33	0.253	0.34	0.321
199	1215	A	8	4		10	12	54.80				0.880	-1.6	1.32	0.597	0.79	0.691
199	1215	A	8	4		20	22	54.90				5.222	-9.5	1.27	0.383	0.48	2.529
199	1215	A	8 H	4	W	30	32	55.00	8.645	2.599	0.301		-18.7	0.81	0.367	0.30	0.089
199	1215	A	8	4		40	42	55.10				1.996	-30.9	0.82	0.606	0.50	0.991
199	1215	A	8 H	4	W	50	52	55.20	12.780	0.000	0.000		-43.0	0.83	0.577	0.48	0.000
199	1215	A	8	4		60	62	55.30				0.245	-55.2	0.82	0.669	0.55	0.134

Table A.8-*Continued*

199	1215	A	8 H	4	W	70	72	55.40	11.931	0.000	0.000		-67.3	0.87	0.600	0.52	0.000
199	1215	A	8	4		80	82	55.50				0.598	-78.8	0.87	0.625	0.54	0.325
199	1215	A	8 H	4	W	90	92	55.60	10.625	0.000	0.000		-90.4	0.86	0.685	0.59	0.000
199	1215	A	8	4		100	102	55.70				0.783	-102.3	0.82	0.613	0.50	0.394
199	1215	A	8 H	4	W	110	112	55.80	8.298	0.000	0.000		-114.4	0.83	0.550	0.45	0.000
199	1215	A	8	4		120	122	55.90				2.836	-126.5	0.83	0.651	0.54	1.526
199	1215	A	8 H	4	W	130	132	56.00	8.439	0.000	0.000		-137.7	1.11	0.492	0.55	0.000
199	1215	A	8 H	4	W	140	142	56.10	8.739	0.000	0.000		-146.8	1.10	0.372	0.41	0.000
199	1215	A	8 H	4	W	148	150	56.18	11.015	0.000	0.000		-154.1	1.10	0.602	0.66	0.000

*Significant amount of chert in bulk sample, **Age model from Leon-Rodriguez and Dickens (2010), ***Dry bulk density (DBD) calculated from calcium carbonate weight percent (Hancock et al., 2005) calibrated with the high biogenic carbonate weight percent equation from Snoeckx and Rea (1994).

Appendix B

Site 401 digestion and ICP data tables

Table B.1 Site 401 ETM2 bulk sediment sample digestion data

Exp/ Leg	Site	Core	Sect	Half	Top (cm)	Bottom (cm)	Depth (mbsf)	Total digest (mg/L)	Al* 394.401 Avg (mg/L)	Al *** normalized (mg Al / mg sample)	Ba* 230.424 Avg (mg/L)	Ba *** normalized (µg Ba / mg sample)	Ca** 616.217 Avg (mg/L)	Ca *** normalized (mg Ca / mg sample)	Ti* 368.519 Avg (mg/L)	Ti *** normalized (µg Ti / mg sample)	Ba / Al	Ba / Ti
48	401	13R	1	W	11	13	189.11	331.97	6.138	0.018	0.163	0.491	94.9	0.286	0.334	1.006	0.027	0.488
48	401	13R	1	W	37	39	189.37	331.27	7.614	0.023	0.179	0.540	92	0.278	0.448	1.352	0.024	0.400
48	401	13R	1	W	65	67	189.65	330.65	9.701	0.029	0.215	0.650	83.6	0.253	0.488	1.476	0.022	0.441
48	401	13R	1	W	87	89	189.87	332.81	11.21	0.034	0.256	0.769	71.6	0.215	0.572	1.719	0.023	0.448
48	401	13R	1	W	101	103	190.01	336.57	13.2	0.039	0.3	0.891	64.2	0.191	0.583	1.732	0.023	0.515
48	401	13R	1	W	109	111	190.09	328.86	8.773	0.027	0.165	0.502	81.5	0.248	0.411	1.250	0.019	0.401
48	401	13R	1	W	119	121	190.19	329.35	10.2	0.031	0.247	0.750	78.7	0.239	0.485	1.473	0.024	0.509
48	401	13R	1	W	144	146	190.44	331.31	10.74	0.032	0.294	0.887	73.8	0.223	0.517	1.560	0.027	0.569
48	401	13R	1	W	16	18	190.66	334.72	4.678	0.014	0.186	0.556	91.3	0.273	0.245	0.732	0.040	0.759

*OSU PerkinElmer ICP-AES average wavelength with lowest percent error relative to quality control standard **UTA Shimadzu ICP-AES average wavelength with lowest percent error relative to quality control standard. ***Elements normalized to ICP-AES concentration over total digest sample weight

Table B.2 Site 401 ETM2 and raw XRF scan data for calibration D'haenens et al. (2014),

Site	Core	Sect	Top (cm)	Bottom (cm)	Depth (mbsf)	Total digest mg/L	Al_2O_3 weight %*	Al* raw counts	Al¿ CLR	$BaSO_4$ weight %*	Ba* raw count	Ba¿ CLR	$CaCO_3$ weight %**	Ca* raw count	Ca¿ CLR	TiO_2 weight %*	Ti* raw count	Ti¿ CLR
401	13R	1	11	13	189.11	331.97	4.56	646	-0.757	0.039	2304	-0.205	2304	212471	1.760	0.21	587	-0.799
401	13R	1	37	39	189.37	331.27	5.42	654	-0.797	0.045	3062	-0.127	3062	173328	1.626	0.28	813	-0.703
401	13R	1	65	67	189.65	330.65	6.55	707	-0.752	0.052	2687	-0.173	2687	204879	1.710	0.31	656	-0.785
401	13R	1	87	89	189.87	332.81	6.90	1136	-0.605	0.060	3720	-0.090	3720	95838	1.321	0.36	1085	-0.625
401	13R	1	101	103	190.01	336.57	7.70	722	-0.683	0.067	4010	0.062	4010	155232	1.650	0.36	326	-1.028
401	13R	1	109	111	190.09	328.86	5.86	1267	-0.635	0.040	3305	-0.218	3305	176392	1.509	0.26	1205	-0.656
401	13R	1	119	121	190.19	329.35	6.41	620	-0.779	0.057	3153	-0.073	3153	225070	1.781	0.31	440	-0.928
401	13R	1	144	146	190.44	331.31	6.65	809	-0.733	0.066	3523	-0.094	3523	169958	1.589	0.33	759	-0.761
401	13R	1	16	18	190.66	334.72	3.76	332	-0.928	0.044	2750	-0.010	2750	161573	1.759	0.15	426	-0.820

*Raw XRF counts from D'haenens et al. (2014), ¿ Centered log ratio (CLR) following Aitchison (1986).

Table B.3 Site 401 ETM2 digested residues from barite separation data

Exp/ Leg	Site	Core	Sect	Half	Top (cm)	Bottom (cm)	Depth (mbsf)	Initial bulk dry wt (mg)	Barite residue digested (mg)	Total residue digested mg/L	Al* 394.401 Avg (mg/L)	Al ** normalized (mg Al / mg residue)	Ba* 455.403 Avg (mg/L)	Ba ** normalized (mg Ba / mg residue)	Ba/Al
48	401	13R	1	W	11	13	189.11	16075.6							
48	401	13R	1	W	13	15	189.13	14908.4							
48	401	13R	1	W	15	17	189.15	30521.8	20.2	336.62	9.04	0.027	0.049	0.146	0.005
48	401	13R	1	W	24	26	189.24	22526.3	19.9	330.25	10.19	0.031	0.049	0.148	0.005
48	401	13R	1	W	37	39	189.37!	21719.5	20.1	334.67	11.77	0.035	0.048	0.143	0.004
48	401	13R	1	W	45	47	189.45!	20356.5	13.9	231.41	8.12	0.035	0.049	0.212	0.006
48	401	13R	1	W	59	61	189.59!	34306	20.0	333.01	12.23	0.037	0.117	0.351	0.010
48	401	13R	1	W	65	67	189.65!	23905.1	20.0	332.41	10.03	0.030	0.066	0.199	0.007
48	401	13R	1	W	77	79	189.77!	34173.7	19.9	331.22	11.33	0.034	0.062	0.187	0.005
48	401	13R	1	W	80	82	189.80	22973.6	19.8	329.07	13.19	0.040	0.045	0.137	0.003
48	401	13R	1	W	87	89	189.87!	23436.8	19.9	331.25	9.34	0.028	0.046	0.139	0.005
48	401	13R	1	W	92	93.5	189.92!	28526.7	20.0	330.71	9.63	0.029	0.072	0.218	0.007
48	401	13R	1	W	101	103	190.01!	38010.5	19.8	328.53	8.34	0.025	0.070	0.213	0.008
48	401	13R	1	W	104	106	190.04!	22721.1	20.1	335.13	10.34	0.031	0.054	0.161	0.005
48	401	13R	1	W	109	111	190.09!	28351.5	20.1	334.67	10.78	0.032	0.063	0.188	0.006
48	401	13R	1	W	114	116	190.14	31342.4	20.0	333.05	8.58	0.026	5.305	15.929	0.618
48	401	13R	1	W	119	121	190.19!	29701.3	20.2	336.26	10.71	0.032	0.121	0.360	0.011
48	401	13R	1	W	125	127	190.25!	35465.5	20.2	336.64	11.21	0.033	0.084	0.250	0.007
48	401	13R	1	W	133	135	190.33	37556.1	19.8	325.65	12.40	0.038	0.081	0.249	0.007
48	401	13R	1	W	138	140	190.38!	26867.9	19.9	324.63	11.01	0.034	0.057	0.176	0.005
48	401	13R	1	W	144	146	190.44!	27653.2	20.0	333.28	12.88	0.039	0.142	0.426	0.011

Table B.3-*Continued*

48	401	13R	1	W	7	9	190.57!	35320	20.0	332.16	10.73	0.032	0.041	0.123	0.004
48	401	13R	1	W	10	12	190.60	19823.4	12.6	208.99	6.51	0.031	0.027	0.129	0.004
48	401	13R	1	W	16	18	190.66	24041.1	15.0	249.59	9.69	0.039	0.044	0.176	0.005

*OSU PerkinElmer ICP-AES average wavelength with lowest percent error relative to quality control standard, !Sample corrected for drift.
**Elements normalized to ICP-AES concentration over total digest sample weight

Table B.3 Site 401 PETM barite residue digestion data

Exp/ Leg	Site	Core	Sect	Half	Top (cm)	Bottom (cm)	Depth (mbsf)	Initial bulk dry wt (mg)	Barite residue digested (mg)	Total residue digested mg/L	Al* 394.401 Avg (mg/L)	Al *** normalized (mg Al / mg residue)	Ba* 455.403 Avg (mg/L)	Ba *** normalized (mg Ba / mg residue	Ba/Al
48	401	14R	1	W	60	62	199.10	20789	20.2	335.28	7.19	0.021	0.892	2.661	0.124
48	401	14R	1	W	68	70	199.18	23473.8	19.9	331.63	5.96	0.018	2.157	6.504	0.362
48	401	14R	1	W	78	80	199.28	23025.7	19.9	331.17	2.55	0.008	0.415	1.253	0.163
48	401	14R	1	W	88	90	199.38	24097.7	20	333.18	5.52	0.017	2.690	8.074	0.488
48	401	14R	1	W	110	112	199.60	30455.2	19.8	328.48	4.43	0.013	5.452	16.598	1.232
48	401	14R	1	W	115	117	199.65	22202.1	20.2	336.02	8.13	0.024	1.501	4.467	0.185
48	401	14R	1	W	129	131	199.79	24675.8	19.8	328.68	5.72	0.017	0.163	0.496	0.029
48	401	14R	1	W	141	143	199.91	22181.6	19.8	329.01	5.13	0.016	0.775	2.356	0.151
48	401	14R	2	W	13	15	200.13	27334.3	20.2	334.44	3.24	0.010	0.978	2.924	0.302
48	401	14R	2	W	25	27	200.25	15588.7	19.9	330.41	10.11	0.031	3.291	9.960	0.326
48	401	14R	2	W	35	37	200.35	23096.7	20	332.92	5.19	0.016	0.456	1.370	0.088
48	401	14R	2	W	43	45	200.43	15196.4	20.2	335.04	7.38	0.022	0.064	0.191	0.009
48	401	14R	2	W	53	55	200.53	35832.1	20	333.01	5.84	0.018	3.028	9.093	0.518
48	401	14R	2	W	60	62	200.60	27106.1							
48	401	14R	2	W	78	80	200.78	29410.2	20.2	336.36	5.15	0.015	1.351	4.016	0.262
48	401	14R	2	W	80	82	200.80	19751.4	20.2	334.80	7.53	0.023	0.121	0.361	0.016
48	401	14R	2	W	91	93	200.91	17884.7	20	333.05	9.79	0.029	0.675	2.027	0.069
48	401	14R	4	W	11	14	203.11	15989.6	20.1	332.42	9.21	0.028	0.689	2.073	0.075
48	401	14R	4	W	14	17	203.14	26158.7	20.1	333.09	9.15	0.027	0.093	0.279	0.010

*OSU PerkinElmer ICP-AES average wavelength with lowest percent error relative to quality control standard, ***Elements normalized to ICP-AES concentration over total digest sample weight

Appendix C

MATLAB codes for barite separation purity

C.1: test_red_fill_script2.m (slightly modified from original script by T.J. Fincannon, personal communication)

```
filename= 'E:\ .jpg'
x = imread(filename)

test=x
red = x(:,:,1); % Red channel
green = x(:,:,1); % Green channel
blue = x(:,:,1); % Blue channel
%matlab formula to compute grey scale
grey_x= 0.2989*red + 0.5870*green + 0.1140*blue

%index cells values between range ex: 36- 142
Impur = (grey_x >= 35 & grey_x <= 142);
Impur_mat = +Impur
%create 10by10 filter mask
Filt= ones(10)

%average cells by 10x10 square with all boundry cells=1
Impur_avg = (conv2(Impur_mat,Filt,'same')/100)
%Compute all impurites with values larger than .5
Impurities = (Impur_avg >= .9)

%Turn impurities color red
red(Impurities)=200
green(Impurities)=0
blue(Impurities)=0

%output to test matrix
test(:,:,1)=red; test(:,:,2)=green; test(:,:,3)=blue;

%view and compare originl and test
figure, imshow(x)
figure, imshow(test)
```

C.2: SEMImageAnalysis.m (script by S.C. Carter, personal communication)

```
%change the part in '' to your file path
%keep the *.bmp at the end
%Or whatever file type you have...
srcFiles = dir('E:\ *.jpg');

%%Creates cell that data will be added to
i=1;
j=1;
C = cell(i,j);
%%Reads in images from the folder
for i = 1 : length(srcFiles)
   %change the part in '' to what you have above,
   %but with no *.bmp at the end
   filename = strcat('E:\', srcFiles(i).name);       %%Reads in image from folder
   I = imread(filename);
   x = percentBaSO4new(I);          %%Calculates percentage of white grains (BaSO4)

   C{i,j} = srcFiles(i).name;      %%Appends file name and percentage to cell array
   j = j+1;
   C{i,j} = x;
   j = 1; i = i+1;
end

%When you run the .m file, the percentages and picture name will be
%saved into the "C" array, which I just copy into excel
```

C.3: PercentBaSO4new.m (script by S.C. Carter)

```
function y = percentBaSO4new(x)
%PERCENTBaSO4 returns the percentage of white grains in an image relative
%to the number of red grains (amount of BaSO4 relative to impurities)
%%Counts the number of redish pixels, which represents the impurities
%%colored red in Adobe

Impurities = (x(:,:,1)>200 & x(:,:,2)<40 & x(:,:,3)<40);
area_Impurities = sum(Impurities(:));

%%If image is RGB, converts to grayscale
[m,n,j] = size(x);
if j>1
   x = rgb2gray(x);
end

%%Makes image binary with only BaSO4 grains white, then counts number of
%%white pixels and outputs percent relative to red pixels
BaSO4 = x > 91;
area_BaSO4 = sum(sum(BaSO4));
Total = area_BaSO4 + area_Impurities;
y = 100.0 * area_BaSO4 / Total;
```

References

Agnini, C., Fornaciari, E., Rio, D., Tateo, F., Backman, J., & Giusberti, L. (2007). Responses of calcareous nannofossil assemblages, mineralogy and geochemistry to the environmental perturbations across the Paleocene/Eocene boundary in the Venetian Pre-Alps. Marine Micropaleontology, 63(1), 19–38.

Aitchison, J. (1986). The statistical analysis of compositional data. London: Chapman and Hall.

Alldredge, A. L., Passow, U., & Logan, B. E. (1993). The abundance and significance of a class of large, transparent organic particles in the ocean. Deep Sea Research Part I: Oceanographic Research Papers, 40(6), 1131–1140.

Armstrong, R. A., Lee, C., Hedges, J. I., Honjo, S., & Wakeham, S. G. (2002). A new, mechanistic model for organic carbon fluxes in the ocean based on the quantitative association of POC with ballast minerals. Deep Sea Research Part II: Topical Studies in Oceanography, 49(1), 219–236.

Berger, W. H., Smetacek, V. S., & Wefer, G. (1989). Ocean productivity and paleoproductivity—an overview. Productivity of the Ocean: Present and Past, (44), 1–34.

Berner, R. A. (2003). The long-term carbon cycle, fossil fuels and atmospheric composition. Nature, 426(6964), 323–326.

Bernstein, R. E., Byrne, R. H., Betzer, P. R., & Greco, A. M. (1992). Morphologies and transformations of celestite in seawater: The role of acantharians in strontium and barium geochemistry. Geochimica et Cosmochimica Acta, 56(8), 3273-3279.

Bertram, M. A., & Cowen, J. P. (1997). Morphological and compositional evidence for biotic precipitation of marine barite. Journal of Marine Research, 55(3), 577–593.

Bice, K. L., Barron, E. J., & Peterson, W. H. (1997). Continental runoff and early Cenozoic bottom-water sources. Geology, 25(10), 951–954.

Bigeleisen, J. (1965). Chemistry of isotopes. Science, 147(3657), 463–471.

Bishop, J. K. (1988). The barite-opal-organic carbon association in oceanic particulate matter. Nature, 332(6162), 341–343.

Bornemann, A., Norris, R. D., Lyman, J. A., D'haenens, S., Groeneveld, J., Röhl, U., Farley, K. A., & Speijer, R. P. (2014). Persistent environmental change after the Paleocene–Eocene Thermal Maximum in the eastern North Atlantic. Earth and Planetary Science Letters, 394, 70–81.

Bowen, G. J., & Zachos, J. C. (2010). Rapid carbon sequestration at the termination of the Palaeocene-Eocene Thermal Maximum. Nature Geoscience, 3(12), 866–869.

Bralower, T. J. (2002). Evidence of surface water oligotrophy during the Paleocene- Eocene thermal maximum: Nannofossil assemblage data from Ocean Drilling Program Site 690, Maud Rise, Weddell Sea. Paleoceanography, 17(2).

Bralower, T. J., Premoli Silva, I., Malone, M., and the Scientific Participants of Leg 198 (2002). Proceedings of the Ocean Drilling Program, Initial Report, V. 198, available at: http://www-odp.tamu. edu/publications/198 IR/198ir.htm, 2002a.

Brinkhuis, H., Schouten, S., Collinson, M. E., Sluijs, A., Damsté, J. S. S., Dickens, G. R., Huber, M., Cronin, T. M., Onodera, J., & Takahashi, K. (2006). Episodic fresh surface waters in the Eocene Arctic Ocean. Nature, 441(7093), 606–609.

Broecker, W. S., & Peng, T. H. (1982). Tracers in the Sea, 690 pp. Lamont-Doherty Geological Observatory, Palisades, NY.

Bryan, K., & Cox, M. D. (1967). A numerical investigation of the oceanic general circulation. Tellus, 19(1), 54–80.

Buesseler, K. O. (1991). Do upper-ocean sediment traps provide an accurate record of particle flux? Nature, 353(6343), 420–423.

Chun, C. O., Delaney, M. L., & Zachos, J. C. (2010). Paleoredox changes across the Paleocene-Eocene thermal maximum, Walvis Ridge (ODP Sites 1262, 1263, and 1266): Evidence from Mn and U enrichment factors. Paleoceanography, 25(4).

Cloern, J. E. (1987). Turbidity as a control on phytoplankton biomass and productivity in estuaries. Continental Shelf Research, 7(11–12), 1367–1381.

Daneri, G., Dellarossa, V., Quiñones, R., Jacob, B., Montero, P., & Ulloa, O. (2000). Primary production and community respiration in the Humboldt Current System off Chile and associated oceanic areas. Marine Ecology Progress Series, 197, 41–49.

DeConto R., Galeotti S., Pagani M., Tracy D. M., Pollard D., & Beerling D. J. (2010). Hyperthermals and orbitally paced permafrost soil organic carbon dynamics. Presented at AGU Fall Meeting, Dec. 13–17, San Francisco (Abstr.PP21E-08).

DeConto, R. M., Galeotti, S., Pagani, M., Tracy, D., Schaefer, K., Zhang, T., Pollard, D., & Beerling, D. J. (2012). Past extreme warming events linked to massive carbon release from thawing permafrost. Nature, 484(7392), 87–91.

Dedert, M., Stoll, H. M., Kroon, D., Shimizu, N., Kanamaru, K., & Ziveri, P. (2012). Productivity response of calcareous nannoplankton to Eocene Thermal Maximum 2 (ETM2). Climate of the Past, 8, 977–993.

Defant, A. (1961). Physical Oceanography Vol. 1, New York and London, Pergamon Press, 729.

Dehairs, F., Chesselet, R., & Jedwab, J. (1980). Discrete suspended particles of barite and the barium cycle in the open ocean. Earth and Planetary Science Letters, 49(2), 528–550.

Dehairs, F., Stroobants, N., & Goeyens, L. (1991). Suspended barite as a tracer of biological activity in the Southern Ocean. Marine Chemistry, 35(1–4), 399–410.

Dehairs, F., Baeyens, W., & Goeyens, L. (1992). Accumulation of suspended barite at mesopelagic depths and export production in the Southern Ocean. Science, 258(5086), 1332–1336.

de Jesus Mendes, P. A., & Thomsen, L. (2012). Effects of ocean acidification on the ballast of surface aggregates sinking through the twilight zone. PloS One, 7(12), e50865.

D'haenens, S., Bornemann, A., Stassen, P., & Speijer, R. P. (2012). Multiple early Eocene benthic foraminiferal assemblage and δ 13 C fluctuations at DSDP Site 401 (Bay of Biscay—NE Atlantic). Marine Micropaleontology, 88, 15–35.

D'haenens, S., Bornemann, A., Claeys, P., Röhl, U., Steurbaut, E., & Speijer, R. P. (2014). A transient deep- sea circulation switch during Eocene Thermal Maximum 2. Paleoceanography, 29(5), 370–388.

Dickens, G. R. (2011). Down the rabbit hole: Toward appropriate discussion of methane release from gas hydrate systems during the Paleocene-Eocene thermal maximum and other past hyperthermal events. Climate of the Past, 7(3), 831–846.

Dickens, G. R., O'Neil, J. R., Rea, D. K., & Owen, R. M. (1995). Dissociation of oceanic methane hydrate as a cause of the carbon isotope excursion at the end of the Paleocene. Paleoceanography, 10(6), 965–971.

Dickens G. R., Castillo M. M., & Walker J. C. G. (1997). A blast of gas in the latest Paleocene: simulating first-order effects of massive dissociation of oceanic methane hydrate. Geology, 25, 259–262.Doney, S. C., & Schimel, D. S. (2007). Carbon and climate system coupling on timescales from the Precambrian to the Anthropocene. Annu. Rev. Environ. Resour., 32, 31–66.

Doney, S. C., Fabry, V. J., Feely, R. A., & Kleypas, J. A. (2009). Ocean acidification: the other CO2 problem. Marine Science, 1.

Dunkley-Jones, T., Lunt, D. J., Schmidt, D. N., Ridgwell, A., Sluijs, A., Valdes, P. J., & Maslin, M. (2013). Climate model and proxy data constraints on ocean warming across the Paleocene–Eocene Thermal Maximum. Earth-Science Reviews, 125, 123–145.

Dymond, J., Suess, E., & Lyle, M. (1992). Barium in deep-sea sediment: A geochemical proxy for paleoproductivity. Paleoceanography, 7(2), 163–181.

Eagle, M., Paytan, A., Arrigo, K. R., van Dijken, G., & Murray, R. W. (2003). A comparison between excess barium and barite as indicators of carbon export. Paleoceanography, 18(1).

Ekman, V. W. (1905). On the influence of the earth\'s rotation on ocean currents. Ark. Mat. Astron. Fys., 2, 1–53.

Eldholm, O., & Thomas, E. (1993). Environmental impact of volcanic margin formation. Earth and Planetary Science Letters, 117(3), 319–329.

Engel, A. (2000). The role of transparent exopolymer particles (TEP) in the increase in apparent particle stickiness (α) during the decline of a diatom bloom. Journal of Plankton Research, 22(3), 485-497.

Engel, A., Delille, B., Jacquet, S., Riebesell, U., Rochelle-Newall, E., Terbrüggen, A., & Zondervan, I. (2004). TEP and DOC production by Emiliania huxleyi exposed to different CO2 concentrations: A mesocosm experiment. Aquat. Microb. Ecol, 34, 93–104.

Eppley, R. W. (1972). Temperature and phytoplankton growth in the sea. Fish. Bull, 70(4), 1063–1085.

Falkowski, P. G., Barber, R. T., & Smetacek, V. (1998). Biogeochemical controls and feedbacks on ocean primary production. Science, 281(5374), 200–206.

Farley, K. A., & Eltgroth, S. F. (2003). An alternative age model for the Paleocene–Eocene thermal maximum using extraterrestrial 3 He. Earth and Planetary Science Letters, 208(3), 135–148.

Foster, L. C., Schmidt, D. N., Thomas, E., Arndt, S., & Ridgwell, A. (2013). Surviving rapid climate change in the deep sea during the Paleogene hyperthermals. Proceedings of the National Academy of Sciences, 110(23), 9273–9276.

Fu, F.-X., Warner, M. E., Zhang, Y., Feng, Y., & Hutchins, D. A. (2007). Effects of increased temperature and CO2 on photosynthesis, growth, and elemental ratios in marine Synechococcus and Prochlorococcus (Cyanobacteria). Journal of Phycology, 43(3), 485–496.

Ganachaud, A., & Wunsch, C. (2000). Improved estimates of global ocean circulation, heat transport and mixing from hydrographic data. Nature, 408(6811), 453–457.

Gavrilov Y.O., Shcherbinina E. A., & Oberhänsli H. (2003). Paleocene-Eocene boundary events in the northeastern Peri-Tethys. Geological Society of America Special Papers, 369, 147-168.

Gat, J. R. (1996). Oxygen and hydrogen isotopes in the hydrologic cycle. Annual Review of Earth and Planetary Sciences, 24(1), 225–262.

Gibbs, S. J., Stoll, H. M., Bown, P. R., & Bralower, T. J. (2010). Ocean acidification and surface water carbonate production across the Paleocene–Eocene thermal maximum. Earth and Planetary Science Letters, 295(3), 583–592.

Gibbs, S. J., Bown, P. R., Murphy, B. H., Sluijs, A., Edgar, K. M., Pälike, H., Bolton, C.T. & Zachos, J. C. (2012). Scaled biotic disruption during early Eocene global warming events. Biogeosciences, 9(11), 4679–4688.

Goldberg, E. D., & Arrhenius, G. O. S. (1958). Chemistry of Pacific pelagic sediments. Geochimica et Cosmochimica Acta, 13(2), 153-212.

Gutjahr, M., Ridgwell, A., Sexton, P. F., Anagnostou, E., Pearson, P. N., Pälike, H., Norris, R. D., Thomas, E., & Foster, G. L. (2017). Very large release of mostly volcanic carbon during the Palaeocene-Eocene Thermal Maximum. Nature, 548, 573–577.

Hancock, H. J. L. & Dickens, G. R. 2005: Carbonate Dissolution Episodes in Paleocene and Eocene sediment, Shatsky Rise, West-Central Pacific, in: Proceedings of the Ocean Drilling Program, Scientific Results, 198.

Heinze, C., Maier- Reimer, E., & Winn, K. (1991). Glacial pCO2 reduction by the world ocean: Experiments with the Hamburg carbon cycle model. Paleoceanography, 6(4), 395–430.

Hendriks, I. E., Duarte, C. M., & Álvarez, M. (2010). Vulnerability of marine biodiversity to ocean acidification: a meta-analysis. Estuarine, Coastal and Shelf Science, 86(2), 157–164.

Higgins J. A., Schrag D. P. (2006). Beyond methane: towards a theory for the Paleocene-Eocene Thermal Maximum. Earth and Planetary Science Letters, 245, 523–537.

Hoegh-Guldberg, O., Mumby, P. J., Hooten, A. J., Steneck, R. S., Greenfield, P., Gomez, E., Harvel, C. D., Sale, P.F., Edwards, A. J., & Caldeira, K. (2007). Coral reefs under rapid climate change and ocean acidification. Science, 318(5857), 1737–1742.

Holcomb, M., Venn, A. A., Tambutte, E., Tambutte, S., Allemand, D., Trotter, J., & McCulloch, M. (2014). Coral calcifying fluid pH dictates response to ocean acidification. Scientific Reports, 4, 5207.

Iglesias-Rodriguez, M. D., Halloran, P. R., Rickaby, R. E., Hall, I. R., Colmenero-Hidalgo, E., Gittins, J. R., … von Dassow, P. (2008). Phytoplankton calcification in a high-CO2 world. Science, 320(5874), 336–340.

IPCC, Field, C. B., Barros, V. R., Mastrandrea, M. D., Mach, K. J., Abdrabo, M.-K., … Barnett, J. (2014). Summary for policymakers. Climate Change 2014: Impacts, Adaptation, and Vulnerability. Part A: Global and Sectoral Aspects. Contribution of Working Group II to the Fifth Assessment Report of the Intergovernmental Panel on Climate Change, 1–32.

Jennions, S. M., Thomas, E., Schmidt, D. N., Lunt, D., & Ridgwell, A. (2015). Changes in benthic ecosystems and ocean circulation in the Southeast Atlantic across Eocene Thermal Maximum 2. Paleoceanography, 30(8), 1059–1077.

Jin, X., Zhang, X., & Zhou, T. (1999). Fundamental framework and experiments of the third generation of IAP/LASG world ocean general circulation model. Advances in Atmospheric Sciences, 16(2), 197–215.

Kaiho, K., Takeda, K., Petrizzo, M. R., & Zachos, J. C. (2006). Anomalous shifts in tropical Pacific planktonic and benthic foraminiferal test size during the Paleocene–Eocene thermal maximum. Palaeogeography, Palaeoclimatology, Palaeoecology, 237(2), 456–464.

Katz M. E., Pak D. K., Dickens G. R,. & Miller K. G. (1999). The source and fate of massive carbon input during the Latest Paleocene Thermal Maximum. Science, 286, 1531–1533.

Keeling, C. D., Piper, S. C., Bollenbacher, A. F., & Walker, S. J. (2005). Monthly atmospheric 13C/12C isotopic ratios for 10 SIO stations. Trends: A Compendium of Data on Global Change.

Keeling, C. D., Piper, S. C., Bollenbacher, A. F., & Walker, S. J. (2010). Monthly atmospheric 13C/12C isotopic ratios for 10 SIO stations. Trends: A Compendium of Data on Global Change.

Kelly, D. C., Nielsen, T. M., McCarren, H. K., Zachos, J. C., & Röhl, U. (2010). Spatiotemporal patterns of carbonate sedimentation in the South Atlantic: Implications for carbon cycling during the Paleocene–Eocene thermal maximum. Palaeogeography, Palaeoclimatology, Palaeoecology, 293(1), 30–40.

Klaas, C., & Archer, D. E. (2002). Association of sinking organic matter with various types of mineral ballast in the deep sea: Implications for the rain ratio. Global Biogeochemical Cycles, 16(4).

Kvenvolden K.A. (1993). Gas hydrates—geological perspective and global change. Review of Geophysics, 31, 173–187.

Lauretano, V., Littler, K., Polling, M., Zachos, J. C., & Lourens, L. J. (2015). Frequency, magnitude and character of hyperthermal events at the onset of the Early Eocene Climatic Optimum. Climate of the Past, 11(10).

Leon-Rodriguez, L. (2012). Constraints on Ocean Acidification Associated with Rapid and Massive Carbon Injections of the Early Paleogene: The Geological Record at Ocean Drilling Program Site 1215, Equatorial Pacific Ocean. Rice University.

Leon-Rodriguez, L., & Dickens, G. R. (2010). Constraints on ocean acidification associated with rapid and massive carbon injections: The early Paleogene record at ocean drilling program site 1215, equatorial Pacific Ocean. Palaeogeography, Palaeoclimatology, Palaeoecology, 298(3), 409–420.

Littler, K., Röhl, U., Westerhold, T., & Zachos, J. C. (2014). A high-resolution benthic stable-isotope record for the South Atlantic: Implications for orbital-scale changes in Late Paleocene–Early Eocene climate and carbon cycling. Earth and Planetary Science Letters, 401, 18–30.

López-Urrutia, Á., San Martin, E., Harris, R. P., & Irigoien, X. (2006). Scaling the metabolic balance of the oceans. Proceedings of the National Academy of Sciences, 103(23), 8739–8744.

Lourens, L. J., Sluijs, A., Kroon, D., Zachos, J. C., Thomas, E., Röhl, U., Bowles, J., & Raffi, I. (2005). Astronomical pacing of late Palaeocene to early Eocene global warming events. Nature, 435(7045), 1083–1087.

Lunt, D. J., Valdes, P. J., Jones, T. D., Ridgwell, A., Haywood, A. M., Schmidt, D. N., Marsh, R., & Maslin, M. (2010). CO2-driven ocean circulation changes as an amplifier of Paleocene-Eocene thermal maximum hydrate destabilization. Geology, 38(10), 875–878.

Ma, Z., Gray, E., Thomas, E., Murphy, B., Zachos, J., & Paytan, A. (2014). Carbon sequestration during the Palaeocene-Eocene Thermal Maximum by an efficient biological pump. Nature Geoscience, 7(5), 382–388.

Maier-Reimer, E., Mikolajewicz, U., & Hasselmann, K. (1993). Mean circulation of the Hamburg LSG OGCM and its sensitivity to the thermohaline surface forcing. Journal of Physical Oceanography, 23(4), 731-757.

Matsumoto, K. (2007). Biology- mediated temperature control on atmospheric pCO2 and ocean biogeochemistry. Geophysical Research Letters, 34(20).

McCrea, J. M. (1950). On the isotopic chemistry of carbonates and a paleotemperature scale. The Journal of Chemical Physics, 18(6), 849-857.

McInerney, F. A., & Wing, S. L. (2011). The Paleocene-Eocene Thermal Maximum: a perturbation of carbon cycle, climate, and biosphere with implications for the future. Annual Review of Earth and Planetary Sciences, 39, 489–516.

McKinney, C. R., McCrea, J. M., Epstein, S., Allen, H. A., & Urey, H. C. (1950). Improvements in mass spectrometers for the measurement of small differences in isotope abundance ratios. Review of Scientific Instruments, 21(8), 724–730.

Monnin, C., & Cividini, D. (2006). The saturation state of the world's ocean with respect to (Ba, Sr) SO 4 solid solutions. Geochimica et Cosmochimica Acta, 70(13), 3290–3298.

Montadert, L., Roberts, D.G., Auffret, G.A., Bock, W.D., Dupeuble, P.A., Hailwood, E.A., Harrison, W.E., Kagami, H., Lumsden, D.N., Müller, C.M., Schnitker, D., Thompson, R.W., Thompson, T.L., Timofeev, P.P., Bourbon, M., & Mann, D. (1979). In: Montadert, L., Roberts, D.G. (Eds.), Site 401. Initial Reports of the Deep Sea Drilling Program, 48 (4). U.S. Government Printing Office, Washington, pp. 71–123. Government Printing Office, Washington, pp. 1025–1060.

Murray, R. W., & Leinen, M. (1996). Scavenged excess aluminum and its relationship to bulk titanium in biogenic sediment from the central equatorial Pacific Ocean. Geochimica et Cosmochimica Acta, 60(20), 3869–3878.

Nicolo, M. J., Dickens, G. R., Hollis, C. J., & Zachos, J. C. (2007). Multiple early Eocene hyperthermals: Their sedimentary expression on the New Zealand continental margin and in the deep sea. Geology, 35(8), 699–702.

NOAA. (2016). Recent monthly mean CO2 at Mauna Loa. Retrieved November 8, 2016, from http://www.esrl.noaa.gov/gmd/ccgg/trends/

Nomura, R., & Takata, H. (2005). Data report: Paleocene/Eocene benthic foraminifers, ODP Leg 199 Sites 1215, 1220, and 1221, equatorial central Pacific Ocean. In Proceeding of Ocean Drilling Program, Scientific Results 199, 1-34.

Nomura, R., Takata, H., Wilson, P. A., Lyle, M., & Firth, J. V. (2005). Data report: Paleocene/Eocene benthic foraminifers, ODP Leg 199 Sites 1215, 1220, and 1221, equatorial central Pacific Ocean. In Proceeding of Ocean Drilling Program, Scientific Results (Vol. 199, pp. 1–34).

Orr, J. C., Fabry, V. J., Aumont, O., Bopp, L., Doney, S. C., Feely, R. A., Gnanadesikan, A., Gruber, N., Ishida, A., Joos, F., & Key, R. M. (2005). Anthropogenic ocean acidification over the twenty-first century and its impact on calcifying organisms. Nature, 437(7059), 681–686.

Pagani, M., Pedentchouk, N., Huber, M., Sluijs, A., Schouten, S., Brinkhuis, H., Damsté, J.S.S., Dickens, G.R., Backman, J., Clemens, S., & Cronin, T. (2006). Arctic hydrology during global warming at the Palaeocene/Eocene thermal maximum. Nature, 442(7103), 671–675.

Pälike, C., Delaney, M. L., & Zachos, J. C. (2014). Deep- sea redox across the Paleocene- Eocene thermal maximum. Geochemistry, Geophysics, Geosystems, 15(4), 1038-1053.

Panchuk, K., Ridgwell, A., & Kump, L. R. (2008). Sedimentary response to Paleocene-Eocene Thermal Maximum carbon release: A model-data comparison. Geology, 36(4), 315–318.

Pardo, A., Keller, G., Molina, E., & Canudo, J. (1997). Planktic foraminiferal turnover across the Paleocene-Eocene transition at DSDP Site 401, Bay of Biscay, North Atlantic. Marine Micropaleontology, 29(2), 129–158.

Passow, U. (2002a). Production of transparent exopolymer particles (TEP) by phyto-and bacterioplankton. Marine Ecology Progress Series, 236, 1–12.

Passow, U. (2002b). Transparent exopolymer particles (TEP) in aquatic environments. Progress in Oceanography, 55(3), 287–333.

Paytan, A., Kastner, M., & Chavez, F. P. (1996). Glacial to interglacial fluctuations in productivity in the equatorial Pacific as indicated by marine barite. Science, 274(5291).

Paytan, A., & Griffith, E. M. (2007). Marine barite: Recorder of variations in ocean export productivity. Deep Sea Research Part II: Topical Studies in Oceanography, 54(5), 687–705.

Paytan, A., Averyt, K., Faul, K., Gray, E., & Thomas, E. (2007). Barite accumulation, ocean productivity, and Sr/Ba in barite across the Paleocene–Eocene Thermal Maximum. Geology, 35(12), 1139–1142.

Penman, D. E., Hönisch, B., Zeebe, R. E., Thomas, E., & Zachos, J. C. (2014). Rapid and sustained surface ocean acidification during the Paleocene- Eocene Thermal Maximum. Paleoceanography, 29(5), 357–369.

Petrizzo, M. R. (2007). The onset of the Paleocene–Eocene Thermal Maximum (PETM) at Sites 1209 and 1210 (Shatsky Rise, Pacific Ocean) as recorded by planktonic foraminifera. Marine Micropaleontology, 63(3), 187–200.

Pytkowicz, R. M. (1975). Activity coefficients of bicarbonates and carbonates in seawater. Limnology and Oceanography, 20(6), 971–975.

Raffi, I., & De Bernardi, B. (2008). Response of calcareous nannofossils to the Paleocene–Eocene Thermal Maximum: Observations on composition, preservation and calcification in sediments from ODP Site 1263 (Walvis Ridge—SW Atlantic). Marine Micropaleontology, 69(2), 119-138.

Reid, R. O. (1948). The equatorial currents of the eastern Pacific as maintained by the stress of the wind. Journal of Marine Research, 7(2), 74–99.

Reitz, A., Pfeifer, K., De Lange, G. J., & Klump, J. (2004). Biogenic barium and the detrital Ba/Al ratio: a comparison of their direct and indirect determination. Marine Geology, 204(3), 289–300.

Ridgwell, A., & Zeebe, R. E. (2005). The role of the global carbonate cycle in the regulation and evolution of the Earth system. Earth and Planetary Science Letters, 234(3), 299–315.

Riebeek, H. (2011). The Carbon Cycle: Feature Articles [Text.Article]. Retrieved November 10, 2016, from http://earthobservatory.nasa.gov/Features/CarbonCycle/

Riebesell, U., Schulz, K. G., Bellerby, R. G. J., Botros, M., Fritsche, P., Meyerhöfer, M., Neill, C., Nondal, G., Oschlies, A., Wohlers, J., & Zöllner, E. (2007). Enhanced biological carbon consumption in a high CO2 ocean. Nature, 450(7169), 545–548.

Rivkin, R. B., & Legendre, L. (2001). Biogenic carbon cycling in the upper ocean: effects of microbial respiration. Science, 291(5512), 2398–2400.

Röhl, U., Westerhold, T., Monechi, S., Thomas, E., Zachos, J. C., & Donner, B. (2005). The third and final early Eocene thermal maximum: characteristics, timing, and mechanisms of the "X" event. GSA Annual Meeting, Abstracts, 37 (7), p. 264.

Röhl, U., Westerhold, T., Bralower, T. J., & Zachos, J. C. (2007). On the duration of the Paleocene-Eocene thermal maximum (PETM). Geochemistry, Geophysics, Geosystems, 8(12).

Rosenthal, Y., Boyle, E. A., & Slowey, N. (1997). Temperature control on the incorporation of magnesium, strontium, fluorine, and cadmium into benthic foraminiferal shells from Little Bahama Bank: Prospects for thermocline paleoceanography. Geochimica et Cosmochimica Acta, 61(17), 3633–3643.

Sarmiento, J., & Gruber, N. (2006). Ocean Biogeochemical Dynamics. New Jersey: Princeton University Press. Retrieved from http://press.princeton.edu/titles/8223.html

Sarmiento, J. L., Thiele, G., Key, R. M., & Moore, W. S. (1990). Oxygen and nitrate new production and remineralization in the North Atlantic subtropical gyre. Journal of Geophysical Research: Oceans, 95(C10), 18303–18315.

Scudder, R. P., Murray, R. W., Schindlbeck, J. C., Kutterolf, S., Hauff, F., & McKinley, C. C. (2014). Regional- scale input of dispersed and discrete volcanic ash to the Izu- Bonin and Mariana subduction zones. Geochemistry, Geophysics, Geosystems, 15(11), 4369–4379.

Sexton, P. F., Norris, R. D., Wilson, P. A., Pälike, H., Westerhold, T., Röhl, U., Bolton, C.T., & Gibbs, S. (2011). Eocene global warming events driven by ventilation of oceanic dissolved organic carbon. Nature, 471(7338), 349–352.

Shipboard Scientific Party, 2002a. Proceedings of the Ocean Drilling Program, Initial Reports, 1999, in: Lyle, M., Wilson, P.A., Janecek, T.R., et al. (Ed.), Proceedings of the Ocean Drilling Program, 199 Initial Reports. Ocean Drilling Program, College Station, TX (Ocean Drilling Program), pp. 1–87.

Shipboard Scientific Party, 2002b. Leg 199 Preliminary Report. ODP Prelim. Rpt., 99 [Online]. Available from World Wide Web: <http://www.odp.tamu.edu/publications/prelim/199_prel/199PREL.PDF>. [Cited 2017-05-24]

Sluijs, A., & Dickens, G. R. (2012). Assessing offsets between the δ13C of sedimentary components and the global exogenic carbon pool across early Paleogene carbon cycle perturbations. Global Biogeochemical Cycles, 26(4).

Snoeckx, H., & Rea, D. K. (1994). Dry bulk density and CaCO3 relationships in upper Quaternary sediments of the eastern equatorial Pacific. Marine Geology, 120(3–4), 327–333.

Stap, L., Sluijs, A., Thomas, E., & Lourens, L. (2009). Patterns and magnitude of deep sea carbonate dissolution during Eocene Thermal Maximum 2 and H2, Walvis Ridge, southeastern Atlantic Ocean. Paleoceanography, 24(1).

Stap, L., Lourens, L. J., Thomas, E., Sluijs, A., Bohaty, S., & Zachos, J. C. (2010). High-resolution deep-sea carbon and oxygen isotope records of Eocene Thermal Maximum 2 and H2. Geology, 38(7), 607–610.

Stoll, H. M., Shimizu, N., Archer, D., & Ziveri, P. (2007). Coccolithophore productivity response to greenhouse event of the Paleocene–Eocene Thermal Maximum. Earth and Planetary Science Letters, 258(1), 192–206.

Stommel, H. (1948). The westward intensification of wind- driven ocean currents. Eos, Transactions American Geophysical Union, 29(2), 202–206.

Stommel, H. (1979). Determination of water mass properties of water pumped down from the Ekman layer to the geostrophic flow below. Proceedings of the National Academy of Sciences, 76(7), 3051–3055.

Svensen, H., Planke, S., Malthe-Sørenssen, A., Jamtveit, B., Myklebust, R., Eidem, T. R., & Rey, S. S. (2004). Release of methane from a volcanic basin as a mechanism for initial Eocene global warming. Nature, 429(6991), 542–545.

Svensen H., Planke S., & Corfu F. (2010). Zircon dating ties NE Atlantic sill emplacement to initial Eocene global warming. Journal of the Geological. Society, 167, 433–436.

Takeda, K., & Kaiho, K. (2007). Faunal turnovers in central Pacific benthic foraminifera during the Paleocene–Eocene thermal maximum. Palaeogeography, Palaeoclimatology, Palaeoecology, 251(2), 175–197.

Thomas, E. (2007). Cenozoic mass extinctions in the deep sea: What perturbs the largest habitat on Earth? Geological Society of America Special Papers, 424, 1–23.

Thomas, E., Zachos, J. C., & Bralower, T. J. (2000). Deep-sea environments on a warm earth: latest Paleocene-early Eocene. In Huber, B.T, MacLeod, K.G., and Wing, S.L. (Eds.), Warm climates in earth history (pp. 132–160). Cambridge, UK: Cambridge University Press.

Thomas, E., Balestra, B., Monechi, S., & Röhl, U. (2015). The biotic Response to Early Eocene Thermal Maximum 3 at Walvis Ridge, SE Atlantic Ocean. GSA Annual meeting, 47(7), 631.

Urey, H. C. (1947). The thermodynamic properties of isotopic substances. Journal of the Chemical Society, London, 561–581.

Urey, H. C. (1948). Oxygen isotopes in nature and in the laboratory. Science 108(2810), 489–496.

Urey, H. C., Lowenstam, H. A., Epstein, S. & McKinney, C. R. (1951). Measurement of paleotemperatures and temperatures of the Upper Cretaceous of England, Denmark, and the southeastern United States. Geological Society of America Bulletin, 62(4), 399-416.

Van Beek, P., Reyss, J.-L., Bonte, P., & Schmidt, S. (2003). Sr/Ba in barite: a proxy of barite preservation in marine sediments? Marine Geology, 199(3), 205–220.

Vermeer, M., & Rahmstorf, S. (2009). Global sea level linked to global temperature. Proceedings of the National Academy of Sciences, 106(51), 21527–21532.

Volk, T., & Hoffert, M. I. (1985). Ocean carbon pumps: Analysis of relative strengths and efficiencies in ocean- driven atmospheric CO2 changes. The Carbon Cycle and Atmospheric CO: Natural Variations Archean to Present, 99–110.

Weiss, R. F. (1970). The solubility of nitrogen, oxygen and argon in water and seawater. In Deep Sea Research and Oceanographic Abstracts. Elsevier, 17, 721–735.

Westerhold, T., Röhl, U., Laskar, J., Raffi, I., Bowles, J., Lourens, L. J., & Zachos, J. C. (2007). On the duration of magnetochrons C24r and C25n and the timing of early Eocene global warming events: Implications from the Ocean Drilling Program Leg 208 Walvis Ridge depth transect. Paleoceanography, 22(2).

Westerhold, T., Röhl, U., Raffi, I., Fornaciari, E., Monechi, S., Reale, V., Bowles, J., & Evans, H. F. (2008). Astronomical calibration of the Paleocene time. Palaeogeography, Palaeoclimatology, Palaeoecology, 257(4), 377–403.

Westerhold, T., Rohl, U., McCarren, H. K., & Zachos, J. C. (2009). Latest on the absolute age of the Paleocene-Eocene Thermal Maximum (PETM): new insights from exact stratigraphic position of key ash layers +19 and −17. Earth and Planetary Science Letters, 287, 412–419.

Westerhold, T., Röhl, U., Donner, B., McCarren, H. K., & Zachos, J. C. (2011). A complete high-resolution Paleocene benthic stable isotope record for the central Pacific (ODP Site 1209). Paleoceanography, 26(2).

Westerhold, T., Röhl, U., & Laskar, J. (2012). Time scale controversy: Accurate orbital calibration of the early Paleogene. Geochemistry, Geophysics, Geosystems, 13(6).

Winguth, A., Shellito, C., Shields, C., & Winguth, C. (2010). Climate response at the Paleocene–Eocene thermal maximum to greenhouse gas forcing—a model study with CCSM3. Journal of Climate, 23(10), 2562-2584.

Winguth, A. M., Thomas, E., & Winguth, C. (2012). Global decline in ocean ventilation, oxygenation, and productivity during the Paleocene-Eocene Thermal Maximum: Implications for the benthic extinction. Geology, 40(3), 263–266.

Wolf-Gladrow, D. A., Riebesell, U. L. F., Burkhardt, S., & Buma, J. (1999). Direct effects of CO2 concentration on growth and isotopic composition of marine plankton. Tellus B: Chemical and Physical Meteorology, 51(2), 461-476.

Yamaguchi, T., & Norris, R. D. (2012). Deep-sea ostracode turnovers through the Paleocene–Eocene thermal maximum in DSDP Site 401, Bay of Biscay, North Atlantic. Marine Micropaleontology, 86, 32–44.

Zachos, J., Pagani, M., Sloan, L., Thomas, E. & Billups, K. (2001). Trends, rhythms, and aberrations in global climate 65 Ma to present. Science, 292(5517), 686–693.

Zachos, J. C., Kroon, D., Blum, P., & others, A. 24. (2004). Proceedings of the Ocean Drilling Program, Vol. 208. Initial Reports. Early Cenozoic extreme climates: The Walvis Ridge transect. Ocean Drilling Program.

Zachos, J. C., Röhl, U., Schellenberg, S. A., Sluijs, A., Hodell, D. A., Kelly, D. C., Thomas, E., Nicolo, M., Raffi, I., & Lourens, L. J. (2005). Rapid acidification of the ocean during the Pale ocene-Eocene thermal maximum. Science, 308(5728), 1611–1615.

Zachos, J. C., Dickens, G. R., & Zeebe, R. E. (2008). An early Cenozoic perspective on greenhouse warming and carbon-cycle dynamics. Nature, 451(7176), 279–283.

Zachos, J. C., McCarren, H., Murphy, B., Röhl, U., & Westerhold, T. (2010). Tempo and scale of late Paleocene and early Eocene carbon isotope cycles: Implications for the origin of hyperthermals. Earth and Planetary Science Letters, 299(1), 242–249.

Zeebe, R. E., Zachos, J. C., & Dickens, G. R. (2009). Carbon dioxide forcing alone insufficient to explain Palaeocene–Eocene Thermal Maximum warming. Nature Geoscience, 2(8), 576–580.

Zhang, J.-H., Chung, T. D., & Oldenburg, K. R. (1999). A simple statistical parameter for use in evaluation and validation of high throughput screening assays. Journal of Biomolecular Screening, 4(2), 67–73.

Zhou, X., Thomas, E., Winguth, A. M. E., Ridgwell, A., Scher, H., Hoogakker, B. A. A., Rickaby, R.E.M., & Lu, Z. (2016). Expanded oxygen minimum zones during the late Paleocene-early Eocene: Hints from multiproxy comparison and ocean modeling. Paleoceanography, 31(12), 1532–1546.

Ziegler, C. L., & Murray, R. W. (2007). Geochemical evolution of the central Pacific Ocean over the past 56 Myr. Paleoceanography, 22(2).

Biographical Information

Angela Lewis graduated from Cypress-Creek High School in Houston, Texas in June 2002 and was awarded a Bachelor of Science in Biology with a focus in Environmental Science from UT Arlington, Texas in May 2007. A second Bachelor of Science degree was awarded in May 2015 in Earth and Environmental Science at UT Arlington, Texas. Completion of her Master's Thesis was in December 2017, she was awarded an Earth and Environmental Science Master's Degree in December 2017 from UT Arlington, Texas.

Angela was a volunteer Lab Assistant in the summer of 2014 assisting Samantha Carter on her Masters of Science thesis project "Equatorial Pacific Export Production and carbonate accumulation over the Middle Miocene Climate Transition". Later, as an Undergraduate Research Assistant, Angela work on the project "Carbonate accumulation in the Equatorial Pacific during the middle Miocene" and presented her findings at the UT Arlington Annual Celebration of Excellence by Students (ACES) in spring 2015. She submitted a grant proposal to the Evolving Earth Foundation "The global effects of two Eocene hyperthermal events on marine export production" in May 2016 and she presented her thesis at the American Geophysical Union (AGU) Fall Meeting in New Orleans, Louisiana in December 2017.

Her research interests are in marine biogeochemistry which include marine productivity dynamics and nutrient distributions, as well ecology and paleontology. Future plans include pursuing a Doctor of Philosophy degree, postdoctoral research position. Potential career directions include Lab Technician, research assistant, or teaching position in high education.